OpenFOAM Simulations of Wave Forces on Coastal Structures induced by Tsunami and Gravity Current

Peiwei Xie

Doctor of Philosophy

Department of Civil Engineering and Applied Mechanics

McGill University

Montreal, Quebec

2020-04-24

A thesis submitted to McGill University in partial fulfilment of the requirements for the degree of Doctor of Philosophy

DEDICATION

This thesis is dedicated to my dear parents, Shaoyuan Xie and Lizhi She, my beloved sister and brother-in-law, Weishan Xie and Shijie Shu, and my newly-born nephew, Ruoxuan Shu.

ACKNOWLEDGEMENTS

Foremost I would like to express my sincere gratitude to my supervisor, Prof. Vincent H. Chu. All the knowledge, perspectives and research skills I learned from him are invaluable and appreciated. His inspiration, encouragement, and continuous help made this work possible.

The care and encouragement by Prof. Van-Thanh-Van Nguyen and Prof. Sofia Babarutsi are most appreciated. I would also like to thank Mr. Jorge Sayat and Mr. John Bartczak for the technical support in these serval years.

I would like to give my special thanks to Tengkun Li, a friend of many years, for all the encouragement and inspiration. I hope his Journey toward the doctoral degree shares the luckiness that I have. Thanks to all my old friends in China and friends here in Canada. I have been living more or less in isolation over the past several years, it was these friends that helped me stay sane and keep positive. Finally, my deepest gratiude goes to my parents, Shaoyuan Xie and Liyin She, and my sister, Weishan Xie, for their unfailing love and steadfast faith in me.

ABSTRACT

Global warming and sea-level rise have increased the exposure of coastal communities in low-lying area to extreme inundation. Coastal structures need to be designed and redesigned for stability to withstand the wave impact by tsunami. The American Society of Civil Engineers and the Federal Emergency Management Administration (ASCE/SEI 7-16; FEMA-P646) have begun developing guidelines for adaptation to climate changes. Most current research effort has devoted to the development of the inundation maps for the low-lying area of the coast. The goal of the present investigation, however, is focusing on the computation of wave forces and overturning stability of the coastal structures. We used the commercial software ANSYS-Fluent in our initial investigation. However, the open-source solvers, and the pre- and post-processing utilities, managed by the OpenFOAM Foundation were found far more transparent, efficient and adaptable.

This thesis evaluated the performance of two well-used solvers, interFoam and twoLiquidMixingFoam, for their adaptability to calculate wave forces on coastal structures. The interFoam solver is a two-phase incompressible flow solver with the volume-of-fluid interface capturing technique. We modified the interFoam solver to study the tsunami wave force on a vertical seawall, on structures of finite-width and on elevated coastal structures. The solver was calibrated by comparing the simulation results with analytical solution, solution of shallow-water hydraulics, and available experimental data. The mesh refinement study further ensures the accuracy of the numerical solution. The simulation results identified the dependence of wave force on the Froude number and structure characteristics, and also provided the generalized force coefficients for design purpose. The other solver – twoLiquidMixingFoam –

simulates the mixing between two miscible fluids. We used this solver to investigate the earthquake-induced gravity current impacted on sub-sea structures. The simulations by the twoLiquidMixngFoam solver perfectly reproduced the laboratory obseravations. With mesh refinement, the simulations were further extended to find the impact forces at a Reynolds number significantly higher than any previous study.

These simulations by the interFoam and twoLiquidMixingFoam solvers for the wave forces on coastal structures have shown the dependence of wave forces on the Froude number, and provided the formulas for the design of coastal structures. Through the mesh refinement studies and the calibrations, we demonstrate the accuracy and adaptability of these solvers for a broad range of applications in scientific research and engineering.

ABRÉGÉ

Le réchauffement climatique et l'élévation du niveau de la mer ont accru l'exposition des communautés côtières des zones basses aux inondations extrêmes. Les structures côtières doivent être conçues et repensées pour assurer la stabilité afin de résister à l'impact des vagues par le tsunami. L'American Society of Civil Engineers et la Federal Emergency Management Administration (ASCE / SEI 7-16; FEMA-P646) ont commencé à élaborer des directives pour l'adaptation aux changements climatiques. La plupart des efforts de recherche actuels ont été consacrés à l'élaboration des cartes des inondations pour les zones basses de la côte. Cependant, le but de la présente enquête se concentre sur le calcul des forces des vagues et le stabilité contre le renversement des structures côtières. Nous avons utilisé le logiciel commercial ANSYS-Fluent dans notre enquête initiale. Cependant, les solveurs open source et les utilitaires de pré et post-traitement, gérés par la Fondation OpenFOAM, se sont révélés beaucoup plus transparents, efficaces et adaptables.

Cette thèse a évalué les performances de deux solveurs populaires, interFoam et twoLiquidMixingFoam, pour leur capacité de calculer les forces des vagues sur les structures côtières. L'interFoam est un solveur d'écoulements incompressibles à deux phases avec la technique de capture de l'interface de volume de fluide. Nous avons modifié le solveur interFoam pour étudier la force des vagues du tsunami sur une digue verticale, sur des structures de largeur finie et sur des hautes structures côtières. Le solveur a été calibré en comparant les résultats de la simulation avec une solution analytique, une solution hydraulique en eau peu profonde et les données expérimentales disponibles. Une étude de raffinement du maillage assure la précision de la solution numérique. Les résultats de la simulation ont identifié la dépendance de la force des vagues

sur le nombre de Froude et sur les caractéristiques de la structure, et ont également fourni les coefficients de force généralisés qui sont utilisés pour la conception. L'autre solveur - twoLiquidMixingFoam - simule le mélange entre deux fluides incompressibles. Nous avons utilisé ce solveur pour étudier le courant de généré par l'impact d'un tremblement de terre sur les structures sous-marines. Les simulations du solveur twoLiquidMixngFoam reproduisent parfaitement les observations de laboratoire. En utilisant le raffinement du maillage, les simulations ont été étendues pour trouver les forces d'impact à des nombres de Reynolds sensiblement plus élevé que les études précédentes.

Ces simulations par les solveurs interFoam et twoLiquidMixingFoam pour trouver les forces des vagues sur les structures côtières ont montré la dépendance des forces des vagues sur le nombre de Froude, et fourni les formules pour la conception des structures côtières. En calibrant ces solveurs en faisant des études de raffinement de maillage, nous démontrons la précision et l'adaptabilité de ces solveurs pour une large gamme d'applications en recherche scientifique et en ingénierie.

TABLE OF CONTENTS

LIST OF TABLES

LIST OF FIGURES

Chapter 1
INTRODUCTION

Global warming and sea-level rise have increased the exposure of coastal communities to extreme inundation (Parry et al. 2007; FitzGerald et al. 2008; Werner et al. 2009; Nicholls & Cazenava 2010). A moderate rise of sea level can significantly worsen the risk of tsunami hazards to low-lying coastal areas (Dall'Osso et al. 2014; Li et al. 2018). The rise of sea-level is real and is accelerating (Rignot et al. 2011; Nerem et al. 2018; VIMS 2019). Coastal structures in the low-lying areas need to be designed and redesigned for stability to withstand the anticipated greater impact by tsunami.

Coastal structures damaged by tsunami is well documented. Post-event field surveys have been carried out for the 2004 Indian Ocean Tsunami (Liu et al. 2005; Goff et al. 2006) and the 2011 Tōhoku Tsunami (Suppasri et al. 2012; Suppasri et al. 2013; Yeh et al. 2013; De Risi 2017). Structures previously understood to be invulnerable to tsunami were heavily damaged. Many buildings designated for vertical evacuation have failed to function (FEMA P-646). Further study of the wave impact on coastal structures is needed.

We used the open-source interFoam solver, managed by the OpenFOAM Fundation, to determine the tsunami wave force on a vertical seawall, on structures of finite-width and on elevated structures. The interFoam solver is a two-phase fluids solver with interface capture technique. The solver was calibrated with the laboratory work by Arnason et al. (2009) and Robertson et al. (2013). The simulations were then extended to a broader range of flow

conditions and structure characteristics to determine the dependence of wave-force coefficients on the wave Froude number, the width and the elevation of the structures. The simulations by the OpenFOAM solver were three-dimensional. The results were validated by analytical solution and by the two-dimensional simulations using the shallow-water hydraulics model.

OpenFOAM is an open-source C++ library of solvers and pre-/post-processing utilities for fluid dynamics simulation. The solvers and utilities are undergoing rapid development through contributions of a growing community of users. The goal of the thesis, besides the study of tsunami wave impact on coastal structures, is to evaluate the accuracy and adaptability of the OpenFOAM solvers to model wave-structure interaction. For this purpose, we evaluated the performance of another solver, twoLiquidMixingFoam, which is designed for studying the mixing of two miscible fluids. The earthquake-induced turbidity current on sub-sea structures is the problem selected for this evaluation. The sudden destabilization of submarine sediments during landslides caused by earthquakes can produce turbidity currents with great destructive forces. The dynamics of turbidity currents have been the subject of numerous studies. However, relatively little attention has been paid to the impact force of the current, despite the fact that the impact force is needed in the design of sub-sea structures. We conducted three-dimensional numerical simulations using the twoLiquidMixingFoam solver to determine the impact force of turbidity current on a sub-sea cylinder above seabed.

1.1 Literature Review

Most of the existing studies about tsunami focused on the analysis of inundation and flow velocity (Borrero et al. 2006; Matsutomi et al. 2006; Rossetto et al. 2007; Dias et al. 2009; Mori et al. 2011; Fritz et al. 2012;

Jaffe et al. 2012; Park et al. 2013; Park & Cox 2016). Less research attention has been paid on investigating the impact of tsunami on coastal structures, despite its significance in the design and maintenance of coastal structures.

The theoretical analysis of tsunami impact on a seawall R.H. Cross in 1967 started the very beginning of the research in this field. Kirkgöz(1995) conducted two-dimensional experiments to investigate the characteristics of wave breaking on a vertical seawall. The discussion for the effect of breaking wave condition on the tsunami force started by from work. Ramsden (1996) conducted another set of two-dimensional experiments to study the effect of wet-bed and dry-bed conditions on tsunami force on a vertical wall. The significant impulsive force by wet-bed bores was detected, compared to the milder force of a dry-bed surge. Cuomo et al. (2010) studied the breaking wave force and overturning moment on a seawall, and offered an empirical equation for force prediction. Linton et al. (2012) and Robertson et al. (2013) carried out large-scale experiments of tsunami wave force on a vertical wall with different initial inundation depth. In their results, the wave forces were correlated to the wave height and velocity, implying the possible dependence of the wave force on the Froude number.

Besides the vertical seawall, coastal structure of finite width is another significant consideration by researchers. Laboratory work by Asakura et al. (2003) and OCDAI (2009) of tsunami waves hitting a square block offered empirical formulas that correlated the wave force to the wave height. Experiments by Arnason et al. (2009) and Fujima et al. (2009) concluded that the wave force was a function of wave height and velocity, and it is proportional to the stagnation pressure. The usage of drag coefficient was introduced. Based on the previous work, FEMA P-646 suggested the use of drag coefficient $C_D = 2.0$ for predicting the tsunami impact force on a finite-width structure,

and a larger value of $C_D = 3.0$ for structural wall elements of significant width. However, as denoted by Yeh (2014), the value of drag coefficient should depend on the Froude number of the wave. Using the drag coefficient as a constant value may significantly underestimate the wave force. One of the research goals of this thesis is to investigate the dependence of the drag coefficient on the wave Froude number.

In the 2004 Indian Ocean Tsunami event and the 2011 Tohoku Tsunami event, buildings with open nature of the first floor or breakaway ground-level components (wall, windows, doors) were found with more sustainability than others (Dalrymple & Kriebel 2005; Yeh et al. 2013). Indeed, fields surveys also shown that structures with elevation above ground were much more invulnerable in coastal flooding event (Kennedy et al. 2011; Tomiczek et al. 2014). Elevated coastal structure could be an option of vertical evacuation. Thus far, only few research attention has been paid on the study tsunami wave hitting an elevated structure (Park et al. 2017; Park et al. 2019). Another goal of this thesis is to obtain a better comprehension of tsunami wave impact on a elevated structure.

In recent years, more and more advanced numerical models have been developed and applied to study the tsunami impact on coastal structures. St Germain et al. (2012, 2013) used a Smoothed Particle Hydrodynamics model to study the impact of tsunami on structures on both wet beds and dry land. Takagi and Bricker (2014) performed numerical simulations to study the effect of breakwaters during a tsunami event. By using the interFoam solver from OpenFOAM, Douglas and Nistor (2015) investigated the tsunami wave force on a circular cylinder; Higuera et al. (2014a, b) studied the interaction of waves and coastal breakwaters and dikes. Roeber and Bricker (2015) used a two-dimensional BOSZ model to simulate the real-scale impact of tsunami

waves, and have validated the results using the interFoam solver. Most of the numerical work offered decent comparisons with experimental data. Numerical simulation as a research tool has a growing credibility for its accuracy, efficiency and feasibility.

In the research of turbidity current, the generation, propagation and dynamics of the current have been the subject of numerous studies (Hacker et al. 1996; Hartel et al. 2000; Shin et al. 2004; Cantero et al. 2007; Ooi et al. 2007; Ooi et al. 2009; Longo et al. 2018). However, only a few research work has been done in laboratory to measure the impact force of turbidity current on sub-sea structure. Ermanyuk & Gavrilov (2005a, b) conducted the only set of laboratory experiments to investigate the drag and lift forces of turbidity current on a square cylinder and a circular cylinder. Their experiments served as a benchmark for the simulation in this thesis. Gonzalez-Juez et al. (2009) and Gonzalez-Juez et al. (2010) used their self-developed numerical model to study the turbidity current impact on a cylinder at laboratory-scale Reynolds number. The study of turbidity current impact on sub-sea structures with high Reynolds numbers is still missing and would be one of the research topics in this thesis. The adoption of the twoLiquidMixingFoam solver in research includes the work by Zhang et al (2016) for jet flow and by Krpan et al. (2018) for mixing of two horizontal flows. The application on modeling gravity current was not achieved yet and awaiting investigation.

1.2 Numerical Methods in OpenFOAM

The Open Source Field Operation and Manipulation C++ libraries, namely OpenFOAM, is a platform for developing executable applications for solving problems of fluid dynamics. The pre-built solvers provide the options for solving different classes of fluid dynamics issues, including single-phase flow,

multi-phase flow, combustion and heat transfer. The pre-processing and post-processing utilities allow the meshing, initial and boundary conditions setup, parallel running, data processing and graphing of the simulations. A combination of the solvers and utilities ensures consistent data handling across all environments. In particular, the open-source character offers the possibility of modifying and extending the collection of solvers, which provides much more flexibility and transparency than commercial software. The two solvers and the correlated numerical methods used in our studies are introduced in this section as follows.

1.2.1 InterFoam solver

The interFoam solver is a two-phase incompressible flow solver with the volume-of-fluid(VOF) interface capturing technique. The interaction of water and air, as well as the sharp interface between these two liquids, can be accurately simulated by using this solver. The solver employs finite volume discretization on collocated grids for the solution of two-phase equations of fluids. The cell-centered variables are and their face interpolated values are used in the solution procedure. The Reynolds-Averaged Navier-Stokes equations are solved in the InterFoam solver. The conservation equation of mass is given as:

$$\frac{\partial \rho \bar{u_i}}{\partial x_j} = 0 \tag{1.1}$$

and the momentum conservation equation is:

$$\frac{\partial(\rho \bar{u_i})}{\partial t} + \frac{\partial}{\partial x_j}(\rho \bar{u_i}\bar{u_j} + \rho \bar{u_i'u_j'}) = \frac{\partial \bar{p}}{\partial x_i} + \frac{\partial \bar{\tau}_{ij}}{\partial x_j} + \rho g_i + f_{\sigma i} \tag{1.2}$$

where ρ is the fluid density, $\bar{u}_{i,j}$ is the Reynolds-averaged velocity component, u_i' is the fluctuating velocity component, p is the fluid pressure, g_i is the gravitational acceleration, $f_{\sigma i}$ is the surface tension and τ_{ij} is the viscous stress

calculated as:

$$\bar{\tau}_{ij} = \mu(\frac{\partial \bar{u}_i}{\partial x_j} + \frac{\partial \bar{u}_j}{\partial x_i}) \tag{1.3}$$

The free surface is modeled by use of the VOF interface capturing method. A scalar function of volume fraction, $\alpha(x,t)$, whose value is unity at a cell fully occupied by water, and zero if the cell is in the air, is defined. An additional equation besides the mass and momentum conservation equations is implemented to calculate the volume fraction in each cell:

$$\frac{\partial \alpha}{\partial t} + \frac{\partial \alpha \bar{u}_j}{\partial x_j} = 0 \tag{1.4}$$

The cell with value of $\alpha(x,t)$ between one and zero denotes the location of a free surface. The term of surface tension in the momentum conservation equation is modeled as continuum surface force and calculated based on the volume fraction $\alpha(x,t)$(Brackbill et al. 1992).

In this study, the PIMPLE iterative algorithm, which is the combination of the pressure-implicit split operator (PISO) and the semi-implicit method for pressure-linked equations (SIMPLE) algorithms, is used for coupling equations of momentum and mass conservation. The number of corrector is chose as two as suggested in OpenFOAM (Greenfields & Christopher 2017). A classic implicit Euler method was used for time integration together with the dynamic adjustable time stepping technique to guarantee a local Courant number less than 0.8. The second-order linear-Upwind scheme is used for solving the continuity and momentum equations. The second-order VanLeer scheme is utilized for solving the volume fraction equation.The k-ϵ model is solved with MINMOD scheme.

1.2.2 twoLiquidMixingFoam solver

The twoLiquidMixingFoam solver determines the mixing process of two miscible incompressible fluids. The solver calculates the advection-diffusion equation (Krpan et al. 2018)

$$\frac{\partial \alpha}{\partial t} + \nabla \cdot (\mathbf{U}\alpha) = \nabla((D_{ab} + \frac{\nu_t}{S_C})\nabla\alpha) \tag{1.5}$$

for the volume fraction of one fluid α and the volume of the other fluid $1 - \alpha$. The density of the mixed fluid is $\rho = \alpha\rho_0 + (1 - \alpha)\rho_1$. Unlike the two-phase flow with a sharp interface, the mixture zone of the fluids with $0 < \alpha < 1$ may cover a wide range. The velocity vector $\mathbf{U}$ is determined by the continuity equation and the momentum equation (Gruber et al. 2011)

$$\frac{\partial \rho}{\partial t} + \nabla \cdot (\rho\mathbf{U}) = 0 \tag{1.6}$$

$$\frac{\partial \rho\mathbf{U}}{\partial t} + \nabla \cdot (\rho\mathbf{U}\mathbf{U}) = -\nabla p + \nabla \cdot (\mu(\mathbf{U} + \mathbf{U}^T)) + \rho\mathbf{g} \tag{1.7}$$

In the equations, D_{ab} is the molecular diffusivity. ν_t is the turbulent eddy viscosity. S_C is the turbulent Schmidt number calculated as $S_C = \nu/D\rho$. The viscosity μ is allowed to be a function of the fluid volume fraction.

In this study, the spatial discretizations are solved with linear-Upwind scheme except that the volume-fraction terms are solved with the VanLeer scheme. The PIMPLE iterative algorithm is used for coupling equations of momentum and mass conservation. The number of corrector is chose as two as suggested by OpenFOAM (2017). The implicit Euler method was used for time integration. The dynamic time-stepping technique ensures a local Courant number less than 0.8 and offers flexibility to the time integration.

1.2.3 Simulation of Turbulent Flow

Turbulent flow typically developed as an instability of laminar flows appearing at a certain critical Reynolds number, and is broadly observed in practice. Unlike the stable laminar flow, turbulent flows are chaotic, diffusive with rapid mixing, highly time-dependent, and involving three-dimensional vorticity fluctuations with a broad range of time and length scales (Tennekes & Lumley, 1972). The most well-known and accepted theory of turbulence is based on the energy cascade concept developed by Kolmogorov (1941). The turbulence is a composition of a large group of eddies of different sizes, with each eddy possessing a certain amount of energy depends on its dimension. The large eddies break up and transfer their energy to small eddies. The small eddies undergo similar break-up processes and transfer their energy to smaller eddies until the smallest possible eddy is reached. The smallest eddies are at the scale that the molecular viscosity is very effective in dissipating the kinetic energy into heat.

Based on the theory, direct numerical simulation (DNS) resolving the entire spectrum of temporal and spatial turbulent scales can be achieved, with the requirement of a very small time step and a refined mesh size to resolve the small scale motion where energy dissipation takes place. DNS is a highly computational-demanding approach. Its feasibility is limited to the conditions of low Reynolds number and simple geometry (Rodi et al. 2013). The less expensive approaches, i.e., large-eddy simulation (LES) and Reynolds-averaged simulation, are developed and widely adopted in research and industry.

Reynolds-averaged Navier-Stokes simulation

Thus far, the most popular approach for simulating turbulence in engineering issues is the Reynolds-averaged simulation by solving the Reynolds-averaged Navier-Stokes (RANS) equations. In this approach, each variable in

the Navier-Stokers equations is decomposed to a time-averaging component and a fluctuating one, e.g. for velocity:

$$\mathbf{u} = \overline{\mathbf{u}} + \mathbf{u}' \tag{1.8}$$

the continuity equation and momentum equations are obtained as:

$$\frac{\partial \rho}{\partial t} + \nabla \bullet (\rho \bar{\mathbf{u}}) = 0 \tag{1.9}$$

$$\frac{\partial}{\partial t}(\rho \bar{\mathbf{u}}) + \nabla \bullet (\rho \bar{\mathbf{u}} \bar{\mathbf{u}}) = -\nabla \bar{p} + \nabla \bullet \left(\overline{\tau} + \tau^R\right) + \rho \mathbf{g} \tag{1.10}$$

Using such an averaging technique would introduce six new unknowns, as know as Reynolds stress τ^R into the equations. The Reynolds stress tensor is given as:

$$\tau^R = -\rho \overline{\mathbf{u}' \mathbf{u}'} \tag{1.11}$$

As a consequence, the RANS equations are not a closed set. Additional equations are needed to solve for the unknown Reynolds stress. The process of calculating these Reynolds stresses is denoted in the literature by turbulence modeling. The direct modeling of the Reynolds stress is based on the Boussinesq hypothesis, in which the Reynolds stress is assumed to be a linear function of the mean velocity gradients such as (for incompressible flow):

$$\tau^R = -\rho \overline{\mathbf{u}' \mathbf{u}'} = \mu_t \{\nabla \bar{\mathbf{u}} + (\nabla \bar{\mathbf{u}})^T\} - \frac{2}{3} \rho k \mathbf{I} \tag{1.12}$$

where μ_t is the turbulent eddy viscosity and k is the turbulent kinetic energy defined as:

$$k = \frac{1}{2} \overline{\mathbf{u}' \mathbf{u}'} \tag{1.13}$$

For incompressible flows the term $-(2/3)\rho k \mathbf{I}$ in the Reynolds stress is usually combined with the pressure gradient term by defining a turbulent pressure p

as

$$p \leftarrow p + \frac{2}{3}\rho k \tag{1.14}$$

the unknowns are reduced to μ_t alone. The momentum conservation equations are then obtained as:

$$\frac{\partial}{\partial t}(\rho \mathbf{u}) + \nabla \bullet (\rho \mathbf{u}\mathbf{u}) = -\nabla p + \nabla \bullet ((\mu + \mu_t)\nabla \mathbf{u}) + \rho \mathbf{g} \tag{1.15}$$

note that the over bar is dropped from the time-averaged variables.

Turbulence Model

Several groups of turbulence models have been developed based on the Boussinesq hypothesis. The goal of using the turbulence model is to resolve the turbulent viscosity, μ_t. The turbulence models have four main categories: Zero-equation models, one-equation models, two equation models and second-order (six-equation) closure models. Among which the two-equation turbulence models are most popularly used, as it requires additional two equations for solving μ_t and delivers accurate-enough prediction. The zero-equation models use an algebraic equation to solve for μ_t without solving any differential equation. The one-equation models require solving one differential equation to find the turbulent viscosity. The second-order closure models solve the six unknown turbulent stress tensors ($-\rho\overline{\mathbf{u}'\mathbf{u}'}$) separately, which necessitates six equations and make it the most computational expensive one. To be note that, none of the developed models is universally applicable to all flow conditions.

The standard $k-\epsilon$ model by Jones and Launder (1972) is one of the most popular two-equation models. In the $k-\epsilon$ model, the turbulent viscosity is expressed as:

$$\mu_t = \rho C_\mu k^2/\epsilon \tag{1.16}$$

in which k is the turbulent kinetic energy, ϵ is the rate of dissipation of turbulence kinetic energy per unit mass, C_μ is a constant coefficient taken as 0.09.

Two transport equations are added on the Reynolds -averaged Navier-Stokes equations for the calculation of k and ϵ:

$$\frac{\partial}{\partial t}(\rho k) + \nabla \bullet (\rho \mathbf{u} k) = \nabla \bullet (\mu_k \nabla k) + P_k - \rho\epsilon \tag{1.17}$$

$$\frac{\partial}{\partial t}(\rho \epsilon) + \nabla \bullet (\rho \mathbf{u} \epsilon) = \nabla \bullet (\mu_\epsilon \nabla \epsilon) + C_{\epsilon 1}\frac{\epsilon}{k}P_k - C_{\epsilon 2}\rho\frac{\epsilon^2}{k} \tag{1.18}$$

where $\mu_k = \mu + \mu_t/\sigma_k$, $\mu_\epsilon = \mu + \mu_t/\sigma_\epsilon$. The values of the coefficients are assigned as $C_{\epsilon 1} = 1.44, C_{\epsilon 2} = 1.92, \sigma_k = 1.0$ and $\sigma_\epsilon = 1.3$.

The $k - \epsilon$ model is derived based on the assumption of fully turbulent flow and the effects of molecular viscosity is neglected. As a high Reynolds number model, it can not be integrated all the way to the wall, where the viscous sublayer takes place. To allow the integration to the wall region, there are variants of the $k - \epsilon$ model using damping functions, e.g. the well-known van Driest (1956) damping function, to damp the turbulent viscosity towards zero as the distance to the wall decreases. Variants of the model also includes the Re-normalized Group (RNG) $k - \epsilon$ model (Yakhot et al. 1992), which is adapted in our study. The renormalization group theory is applied to derive a turbulence model similar to the k_ϵ model. This model does not include any experimental adjustable parameter. The model produces converged results when $k \to 0$ and $\epsilon \to \infty$, which allows the calculation of flow motion near walls.

Large Eddy Simulation

The key concept of LES is to filter the eddies into large-scale eddies and small-scale eddies when solving the Navier-Stokes equations. The large-scale eddies with a high content of energy are then resolved directly by solving the Navier-Stokes equations, while the small-scale eddies are modeled using a sub-grid scale model. Modeling the small-scale turbulence is feasible as it can be considered as isotropic and independent of flow types and boundary

conditions. This approach avoids solving the small-scale dissipative motion, which reduces the mesh requirement and also allows the simulation of high Reynolds number and complex geometry.

The first step in LES is to split the local quantities f into resolved quantities $\bar{f}$ and fluctuations f', which is called filtering. The fluctuations are the fluid quantities that are smaller than the filter width. In general, the width of the filter is the same as the mesh size. Only motions with scales larger than the mesh size can be resolved. The governing equations of LES are similar to the RANS:

$$\frac{\partial \rho}{\partial t} + \nabla \bullet (\rho \bar{\mathbf{u}}) = 0 \tag{1.19}$$

$$\frac{\partial}{\partial t}(\rho \bar{\mathbf{u}}) + \nabla \bullet (\rho \bar{\mathbf{u}} \bar{\mathbf{u}}) = -\nabla \bar{p} + \nabla \bullet \left(\overline{\tau} + \tau^{SGS}\right) + \rho \mathbf{g} \tag{1.20}$$

Note that fluid properties with the over bar are no longer the time-averaged properties but the filtered properties to be resolved. The sub-grid scale stresses τ^{SGS} are expressed as:

$$\tau^{SGS} = \overline{\mathbf{u}\mathbf{u}} - \bar{\mathbf{u}}\bar{\mathbf{u}} \tag{1.21}$$

In the sub-grid scale turbulence model, the sub-grid scale stresses are calculated as:

$$\tau^{SGS} = -2\mu_t \bar{S_{ij}} \tag{1.22}$$

in which $\bar{S_{ij}}$ is the resolved rate of strain defined as:

$$\bar{S_{ij}} = \frac{1}{2}\{\frac{\partial \bar{u}_i}{\partial x_j} + \frac{\partial \bar{u}_j}{\partial x_i}\} \tag{1.23}$$

The major task of using SGS models is to obtain the turbulent viscosity μ_t. Details about the different SGS models could be found in the book of *Large-Eddy Simulation in Hydraulics* by Rodi (2013)

1.2.4 Wall Boundary Condition in OpenFOAM

When solving a turbulent flow problem, modifications to the conservation equations are made at the first interior point C in the control volume next to the wall. The value of d^+ at that location, denoted by d_C^+, is first calculated to infer whether the point lies in the viscous or inertial sublayer. d^+ is defined as:

$$d^+ = \frac{du_\tau}{\nu} = y^+ \tag{1.24}$$

where d is the normal distance to the wall, ν is the kinematic viscosity, u_τ is the friction velocity expressed as:

$$u_\tau = \sqrt{\frac{|\tau_w|}{\rho}} \tag{1.25}$$

where $|\tau_w|$ is the magnitude of the wall shear stress. The transition from the viscous to the inertial layer is assumed to occur at a limiting value of d^+, denoted by d_{lim}^+. d_{lim}^+ is a flow-dependent value while all the reported values are within 11 and 12. A value of 11.06 is adopted in OpenFOAM.

If $d_C^+ < d_{lim}^+$ then the first grid point lies in the viscous sublayer, the viscosity on the wall is set equal to the laminar viscosity and the shear stress is computed as for laminar flows. The turbulent kinetic energy on the first grid is set to be zero. The shear stress is assumed constant over the control volume with its value calculated as:

$$\tau_w \frac{\partial \mathbf{u}_C}{\partial d} = \mu \frac{\mathbf{u}_C^2}{d_C^2} \tag{1.26}$$

If $d_C^+ > d_{lim}^+$ then the first grid point lies in the inertial sublayer. The logarithmic wall functions are applied at the first interior point C. The shear stress is calculated using the logarithmic wall function as:

$$|\tau_w| = \rho u_\tau^2 = -\frac{\rho u_\tau \mathbf{u}_C}{\frac{1}{Ka} Ln d_C^+ + B} \tag{1.27}$$

where Ka is the von Karmon constant assigned as 0.41, B is set as 5.25.

1.2.5 Pressure-velocity Coupling Algorithms

On solving the non-linear Navier-Stokes equation, the primary issue that can not be addressed directly with the equations is the missing of an explicit equation for computing the pressure fields in the momentum equation. A solution for it is the reformulation of the Navier-Stokes equations in terms of a momentum equation and a pressure correction equation, which are discretized and solved sequentially. The solution algorithms for solving the momentum and pressure correction equations and coupling the pressure-velocity information are one of the standard prepossessing methods in computational fluid dynamics. The three algorithms correlated to this study are introduced below in brief.

The SIMPLE (Semi Implicit Method for Pressure Linked Equations) algorithm was first developed by Patankar & Spalding (1972). The algorithm starts with a guessed pressure and velocity fields and solves the momentum and pressure equations implicitly. This SIMPLE iteration is repeated until the solution is converged. The PISO (Pressure-Implicit with Splitting of Operators) pressure-velocity coupling scheme adds an outer corrector after the implicit SIMPLE iteration, in which the momentum equation is solved explicitly. The iteration of solving the SIMPLE iteration plus the outer corrector would be repeated until the solution is converged. The outer corrector helps improve the rate of convergence of the solution, and also enhances the efficiency of the calculation. The PIMPLE Algorithm in OpenFOAM is a combination of the SIMPLE and PISO algorithms. Additional iterations are added to the outer corrector to ensure all the explicit components of the equations are converged. The recommended number of correctors of 2 allows a number of iterations between 50 to 1000, depends on at which iteration the solution converges. Better

stability is obtained from the PIMPLE over the PISO algorithm, especially when dealing with large time steps or when the nature of the solution is inherently unstable.

1.3 Organization of the Thesis

The following remarks serve as a guide in reading this manuscript-based thesis. The introduction chapter provides the motivations and objective of the study. This chapter also provides a overview of the numerical methods and a literature review for the relevant research topics. Chapters 2 to 5 are drawn based on the following journal papers and conferences papers:

- Peiwei Xie and Vincent H Chu. The forces of tsunami waves on a vertical wall and on a structure of finite width. *Coastal Engineering* (2019) 149: 65-80.

- Peiwei Xie and Vincent H. Chu. Tsunami Wave Force on Elevated Coastal Structures. *Coastal Engineering* (2020) draft for submission.

- Peiwei Xie and Vincent H. Chu. Impact Forces by a Gravity Current on a Circular Cylinder above the Seabed. *Coastal Engineering* (2020) under review.

- Peiwei Xie and Vincent H. Chu. OpenFOAM Simulation of Bores and Surges on Coastal Structures. E-proceedings of the 38th IAHR World Congress. September 1-6, 2019, Panama City, Panama. doi: 10.3850/38WC09-2019-0664.

- Peiwei Xie and Vincent H. Chu. OpenFOAM Simulation of Gravity-Current Head Impact on a structure on the Sea Floor. *E-proceedings of the 38th IAHR World Congress.* September 1-6, 2019, Panama City, Panama. doi: 10.3850/38WC092019-0187.

• Peiwei Xie and Vincent H. Chu. Storm Surge and Tsunami Impact Forces on Coastal Structures. *The Fourth International Conference on Computational Science and Engineering*. July 25-27, 2019, Ho Chi Minh City, Vietnam.

Chapter 2 presents the study of the wave forces by earthquake-induced tsunami on a vertical seawall and a structure of finite-width. The interFoam solver was validated by comparisons with experimental work, with analytical solution and with shallow-water hydraulics simulations. The dependences of the wave force on the wave Froude number and size of the structure were investigated. The differences of impact between a wet-bed bore and a dry-bed surge are discussed.

In chapter 3, we extended the application of the interFoam solver to study the tsunami wave impact on an elevated coastal structure. The mesh refinement study ensured the solution accuracy. We examined the effect of the elevation, as the most significant parameter for an elevated structure, and validated the dependence of wave force on the wave Froude number and the structure size.

The performance of another two-phase fluid solver for wave-structure interaction, the twoLiquidMixingFoam solver, was evaluated in Chapter 4. The earthquake-induced turbidity current on a sub-sea circular cylinder is the problem selected for this evaluation. The study started with a validation with laboratory work and a selection of turbulence model. The simulations were extended to a high Reynold number that is beyond the range of any previous study. The drag, lift and total forces on the cylinder were analyzed for their dependence of elevation, and compared with the forces of a cylinder in steady flow of uniform density.

The last chapter, Chapter 5, offers the conclusions and the contributions of the thesis.

1.4 Contribution of Authors

The research work and the writing of this thesis and publications were carried out by the candidate. Prof. Vincent H. Chu provides the supervision to all the work and edit of the manuscripts. The shallow-water hydraulics model was developed based on the work by Dr. Lai Wai Tan and Dr. Shooka Karimpour.

Chapter 2
The Forces of Tsunami Waves on a Vertical Wall and on a Structure of Finite Width

Peiwei Xie and Vincent H. Chu. The forces of tsunami waves on a vertical wall and on a structure of finite width. *Coastal Engineering* 149 (2019): 65-80.

Preface

The hydrodynamic forces on coastal structures impacted by tsunami depend on the wave Froude number, the sizes and shapes of the structures and also on whether the structures stand in water or on dry land at the time of the impact. We conducted simulations using shallow-water hydraulic equations and then simulations using full Navier-Stokes equations to determine the wave impact on a vertical wall – i.e., a structure of infinite width – and a structure of finite width. In the case of steep waves on a wet bed, the wave-drag coefficient rose to a peak on impact and then settled to a wave-structure interaction equilibrium. In the case of smooth waves on dry land, the approach to the equilibrium was gradual. The numerical simulations determined the dependence of the wave-drag coefficients on the Froude number and the width-to-depth ratio for waves on wet beds and, separately, for waves on dry land. The simulations also reproduced the wave forces for the range of conditions observed in the laboratory.

LIST OF SYMBOLS

A_w	frontal projection area
c	celerity of an incoming wet-bed bore
c_r	reflected wave celerity
C_D	wave-drag coefficient
$\tilde{C}_D$	wave-drag coefficient at wave-structure equilibrium
$\hat{C}_D$	peak wave-drag coefficient
$\hat{C}_{DF}$	peak wave-drag coefficient on the front face
F	wave-drag force
$\tilde{F}$	wave-drag force at wave-structure equilibrium
$\hat{F}$	peak wave-drag force
g	gravity acceleration
h	depth of water
H	initial still-water depth
H_j	wave height $= H_w - H$
H_r	reflected wave height by SWH-WALL solution
H_w	inflow depth
L	distance from the inlet to the structure
p	bottom pressure
R	run-up height on the front face
$R_{\max}$	maximum run-up height
t	time
$\hat{t}$	time when peak force occurs
t^*	dimensionless time $= (t - \hat{t})U_w/W$ defined by W
t_g^*	dimensionless time $= t\sqrt{g/H_w}$ defined by g
$\tilde{T}$	duration of exceedance in terms of structure width

$\hat{T}_g$	duration of exceedance in terms of gravity
U_w	inflow velocity
W	width of structure
x_F	bore front position
Δx	mesh size in x-direction
Δy	mesh size in y-direction
ρ	density of water

DEFINITION OF TERMS

wall	a structure of infinite width
bore	a wave with a steep front on a wet bed
surge	a wave with a smooth front on dry land
SWH	Shallow Water Hydraulics

2.1 Introduction

"Tsunami" are the waves produced in oceans by the displacement of large volumes of water due to earthquakes, volcanic activities, and landslides. Unlike ocean waves generated by wind, a tsunami is characterized by its long wavelength and its wave period of minutes to tens of minutes (Camfield 1980, FEMA 2012). The advance of these long waves onto coastal waters is often described in the framework of shallow-water hydraulics, as the depth of the coastal waters is small compared with the wavelength.

The devastating effects of tsunami on coastal structures are well documented (Liu et al. 2005; Ghobara et al. 2006; Nistor et al. 2010; Mori et al. 2011; Yeh et al. 2013; De Risi et al. 2017). Post-event field surveys for the 2011 Tohoku Earthquake, carried out by Japan's Ministry of Land, Infrastructure and Transportation, reported that as much as 70% of the 200,000 buildings along the Miyagi coastline suffered damage classified as: Major (19.9%); Complete (2.8%); Collapsed (17.3%); and Washed Away (30.3%). This damage to buildings highlighted the need for a better understanding of wave-structure interaction in the design of coastal structures. Some structures previously understood to be invulnerable to tsunamis were heavily damaged or even destroyed in 2011 (Reese et al. 2011; Suppaasri et al. 2013; Charvet et al. 2014; Yeh et al. 2014).

In the laboratory, solitary waves have been the models for tsunami. The shoaling of the solitary wave onto shallow waters produced bores with steep fronts on wet beds or surges on dry land. Sudden removal of a gate (dam-break) and vertical release of a volume of water were other methods used to produce the bores or the surges in the laboratory. We follow the convention to use the word "bore" for a wave with a steep front on a wet bed, and "surge" for the less steep wave on dry land (Ramsden and Riachlen 1990, Ramsden 1996

and Wüthrich et al. 2018). In the study of tsunami wave force on coastal structures, Ramsden (1996), Linton et al. (2012) and Robertson et al. (2013) studied the impact of waves on a wall in the laboratory. (Please note that the word "wall" is used throughout this paper to describe the large structure of infinite width.) Asakura et al. (2003), Arnason et al. (2009), Japan's Overseas Coastal Area Development Institute (OCADI 2009) and Fujima et al. (2009) studied wave impact on coastal structures of finite width, where the impact is affected by the scattering of the waves laterally around the structure. The impact of the waves on a wall produced the reflected waves traveling only in the upstream direction.

Table 2–1: Wave-force formulas derived from laboratory investigations: H_w = depth; H = initial depth; $H_j = H_w - H$; U_w = velocity; $c = U_w H_w / H_j$ = celerity; W = width of block; L = distance to structures; F = wave-drag force; $C_D = F/(\frac{1}{2}\rho U_w^2 H_w W)$ = wave-drag coefficient.

Authors	Structure	Waves	Wave-force Formulae
Ramsden	wall	dam-break	$F = \frac{1}{2}\rho g(2H_w - H)^2\{1.325 + 0.347(H_w/H - 1) + (H_w/H - 1)^2/58.5 + (H_w/H - 1)^3/7160\}$
Asakura et al.	block	dam-break	$F = 4.5\rho g H_w^2$
Arnason et al.	block	dam-break	$F = C_D(\frac{1}{2}\rho U_w^2)H_w W,\ C_D \simeq 2.0$
OCADI	block	dam-break	$F = 3.3\rho g(H_w - H)^2 + 2.2\rho g(H_w - H)H$
Fujima et al.	block	solitary	$F = 1.5(\frac{1}{2}\rho U_w^2)WH_w\ (H_w/L < 0.05)$ $F = 3.6(\frac{1}{2}\rho U_w^2)WH_w\ (H_w/L > 0.05)$
Robertson et al.	wall	solitary	$F = \frac{1}{2}\rho g H_w^2 + \rho H_j^2 + \rho g^{1/3}(H_j c)^{4/3}$
Linton et al.	wall	solitary	$F = \frac{1}{2}\rho g W H_w^2 + \rho W H_w c^2$

In these laboratory investigations, the measured wave force F on the structure was correlated with the wave height H_w, the wave velocity U_w, the gravity g, and the width of the building W. Table 2.1 summarizes the correlation formulas derived from the laboratory investigations. Due to the differences in channel set-up, wave formation and the buildings' characteristics and scales, the wave parameters do not always have the same definitions. Although each formula may work well with its specific laboratory condition

regarding the structure's type and scale, its range of applicability needs to be defined. Arnason et al. (2009) and Yeh et al. (2014) have suggested the use of a wave-drag coefficient and its possible dependence on the Froude number. Besides the Froude number, the value of the wave-drag coefficient is expected to depend on the size and shape of the structure. The distinction between the advance of bores on a wet bed and surges on dry land is another significant factor that has been examined by Ramsden (1996), Chanson et al. (2003) and Wüthrich et al. (2018) but needs further investigation.

Besides the laboratory work, numerical simulations have been carried out to study the tsunami impact on coastal structures. St Germain et al. (2012, 2015) used an Smoothed Particle Hydrodynamics model to study the impact of tsunami on structures on both wet beds and dry land. Douglas and Nistor (2015) considered the same problem using OpenFOAM simulation. Roeber and Bricker (2015) used a two-dimensional BOSZ model to simulate the real-scale impact of tsunami waves, and have validated the results using OpenFOAM simulation. Takagi and Bricker (2014) performed numerical simulations to study the effect of breakwaters during a tsunami event. The accuracy and efficiency of these numerical simulations are well documented, clearly indicating the potential of numerical simulation in the study of tsunami impact.

In the present investigation, the wave impact on a wall and a square structure were determined by numerical simulations using shallow-water-hydraulics (SWH) equations, and then by simulations using full Navier-Stokes equations conducted by open-source codes under the Open source Field Operation And

Manipulation (OpenFOAM®) platform (Weller et al. 1998). The wave impact on a wall was considered first, to provide the relation between the wave-drag coefficient[1] C_D and the wave Froude number Fr_w. The simulations of wave impact on a square structure–a structure of finite width–would provide the additional dependence of the wave-drag coefficient C_D on the width-to-depth ratio W/H_w of the structure.

This paper has seven sections, including this Introduction. Section 2 presents an analytical solution for the impact of wet-bed bores on a vertical wall. The numerical methods are described in Section 3. The numerical simulations were conducted first for the impact of the bores on structures standing in water, and then for the impact of surges on dry land. Section 4 and Section 5 present the simulation results for the impacts of the wet-bed bore on a wall and on a structure of finite width, respectively. The impact of dry-land surges on a wall and a structure of finite width is considered in Section 6. Finally, summary and conclusion are provided Section 7.

2.2 Analytical Solution for Impact of Bore on a Vertical Wall

We begin with an analytical solution for the impact of a bore on a vertical wall standing in water of depth H. The bore advanced toward the wall with a depth H_w, a velocity U_w and a celerity c as shown in Figure 2–1(a). The reflection by the wall produced an upstream propagating bore of depth H_r and celerity c_r as shown in Figure 2–1(b). The analytical solution was obtained

[1] The wave force obtained from our numerical simulation is the total force including both drag and inertia force. The "drag coefficient" nevertheless is used in other studies of the tsunami (FEMA P646 2012; Yeh et al. 2014). We have decided to follow the convention to use the wave-drag coefficient as the dimensionless coefficient for the wave force.

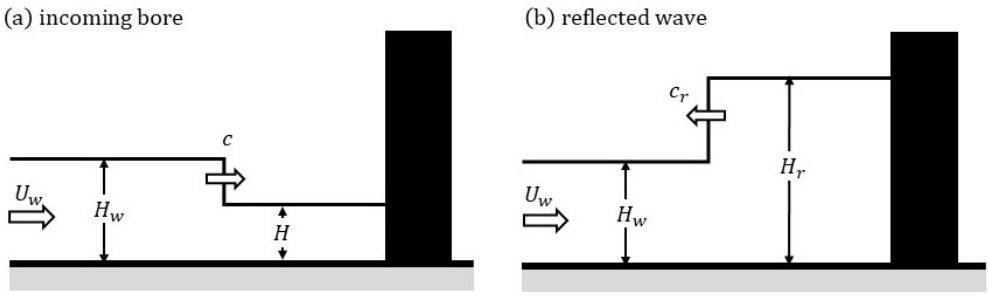

Figure 2–1: (a) The advancement of the bore toward a vertical wall. (b) The reflected wave after the bore impacts on the wall. The bore was produced by an inflow of depth H_w and velocity U_w on an initial still-water depth H.

using the shallow-water-hydraulics (SWH) method as described in the books by Chow (1959) and Henderson (1966). In using this method, the variation of the pressure over the depth of the shallow waters is assumed to be hydrostatic.

2.2.1 Compatibility Condition

For the bore to advance on still water that remains at a constant depth, the inflow depth H_w and the velocity U_w must satisfy a condition compatible to the still-water depth H. Equating the flow force (momentum flux plus hydrostatic pressure force) across the front in a reference frame moving with the celerity c of the bore gives the momentum equation

$$\frac{c^2H^2}{gH_w} + \frac{1}{2}H_w^2 = \frac{c^2H^2}{gH} + \frac{1}{2}H^2 \tag{2.1}$$

The continuity equation is

$$U_wH_w = (H_w - H)c \tag{2.2}$$

Eliminating c from the momentum and continuity equations gives a relation between the depth ratio H_w/H and the wave Froude number Fr_w as follows:

$$\mathrm{Fr}_w^2 = \frac{U_w^2}{gH_w} = \frac{1}{2}(\frac{H_w}{H} + 1)(\frac{H_w}{H} - 1)^2(\frac{H_w}{H})^{-2} \tag{2.3}$$

The line in Figure 2–2(a) is this relation between the depth ratio H_w/H of the bore and its wave Froude number Fr_w. In the numerical simulations, the depth ratio H_w/H was specified. Once this ratio was specified, the wave Froude number Fr_w, and therefore the velocity at the inlet $U_w = \mathrm{Fr}_w\sqrt{gH_w}$, must be selected according to the "compatibility condition" defined by Equation 3.1. The bore advances relatively unchanged on a wet bed if the boundary and the initial conditions are specified according to the compatibility condition.

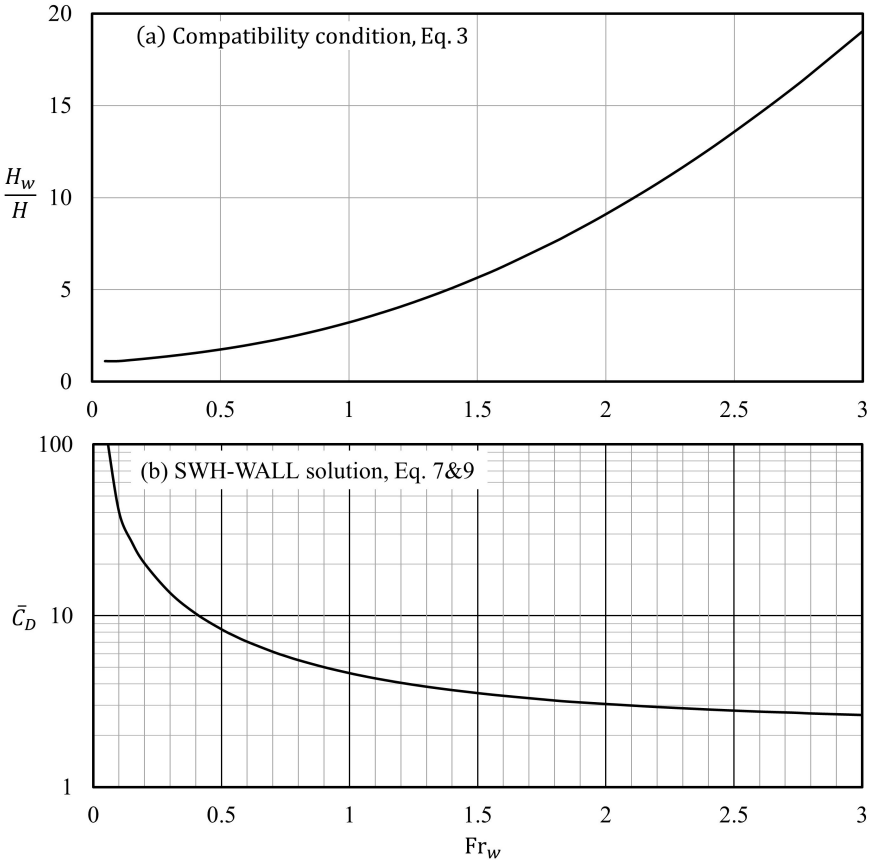

Figure 2–2: (a) The relation between the depth ratio H_w/H and the wave Froude number Fr_w that defines the compatibility condition, Equation 3.1. (b) The SWH-WALL solution for the wave-drag coefficient as a function of the wave Froude number defined by Equations 2.7 and 2.9.

2.2.2 Upstream Propagating Bore

The impact on the wall produced an upstream propagating bore as shown in Figure 2–1(b). The water in front of the wall rises to a depth of H_r as the bore advances with a celerity c_r in the upstream direction. Equating the flow force in a reference frame moving with celerity c_r gives the momentum equation

$$\frac{1}{2}H_w^2 + \frac{(c_r + U_w)^2 H_w^2}{gH_w} = \frac{1}{2}H_r^2 + \frac{c_r^2 H_r^2}{gH_r} \tag{2.4}$$

in which $U_w = q_w/H_w$. The continuity equation is

$$q_w = c_r(H_r - H_w) \tag{2.5}$$

Eliminating c_r from equations 2.4 and 2.5,

$$\frac{1}{2}H_w^2 + \frac{q_w^2 H_r^2}{gH_w(H_r - H_w)^2} = \frac{1}{2}H_r^2 + \frac{q_w^2 H_r^2}{gH_r(H_r - H_w)^2} \tag{2.6}$$

This leads to the following relation between the wave Froude number Fr_w and the reflected-to-incoming wave height ratio H_r/H_w:

$$\mathrm{Fr}_w^2 = \frac{q_w^2}{gH_w^3} = \frac{1}{2}(\frac{H_r}{H_w} + 1)(\frac{H_r}{H_w} - 1)^2(\frac{H_r}{H_w})^{-1} \tag{2.7}$$

2.2.3 Wave Drag Coefficient

If the pressure distribution on the front and back of the vertical wall were assumed to be hydrostatic, the impact force per unit width would be

$$F = \frac{1}{2}\rho g(H_r^2 - H^2). \tag{2.8}$$

The dimensionless variable for the force is the wave-drag coefficient

$$\overline{C}_D = \frac{F}{\frac{1}{2}\rho U_w^2 A_w} = \frac{1}{\mathrm{Fr}_w^2}\frac{H_r^2 - H^2}{H_w^2} \tag{2.9}$$

where A_w is the frontal projection area; $A_w = H_w$ per unit width of the flow. Equation 2.7 and Equation 2.9 define a SWH-WALL solution for the wave-drag

coefficient $\overline{C}_D$ as a function of the wave number Fr_w, shown as the line in Figure 2–2(b). According to this SWH-WALL solution, the wave-drag coefficient follows the asymptotic $\overline{C}_D \to 4/\mathrm{Fr}_w$ as the Froude number Fr_w approaches zero, and approaches a value of $\overline{C}_D \to 2$ as $\mathrm{Fr}_w \to \infty$.

2.3 SWH-MinMod and OpenFOAM Simulations

Two numerical methods, referred to as Shallow Water Hydraulic MinMod (SWH-MinMod) and Open source Field Operation And Manipulation (OpenFOAM), were employed to simulate the impact of the wet-bed bores and dry-land surges on the wall and on a structure of finite width. The SWH-MinMod simulation used the FORTRAN program developed by Karimpour and Chu (2014, 2015, 2016). The discontinuity in the depth and velocity across the wave front in the SWH-MinMod simulation were captured using the well-known MinMod flux-limiting scheme. The simulations for the non-hydrostatic effect using the full Navier-Stokes equations were conducted using open-source codes under the OpenFOAM platform. We chose InterFoam, an incompressible multiphase solver employing the Volume-of-Fluid (VOF) interface-capturing methodology for simulating free surface flows, as the solver. This solver uses a second-order spatial finite-volume discretization scheme. Derivations and discretization can be found in Rusche et al.(2003). The Re-Normalised Group (RNG) theory of Yakhot and Orszag (1986) defines the k-ϵ turbulence model equations. The effectiveness of OpenFOAM simulation has been proven by Hargreaves et al. (2007) for multiphase simulations, and by Higuera et al. (2013a,b) for ocean-wave simulations. OpenFOAM simulations have also been successfully implemented by Douglas and Nistor (2015) in their study of tsunami loading on structures.

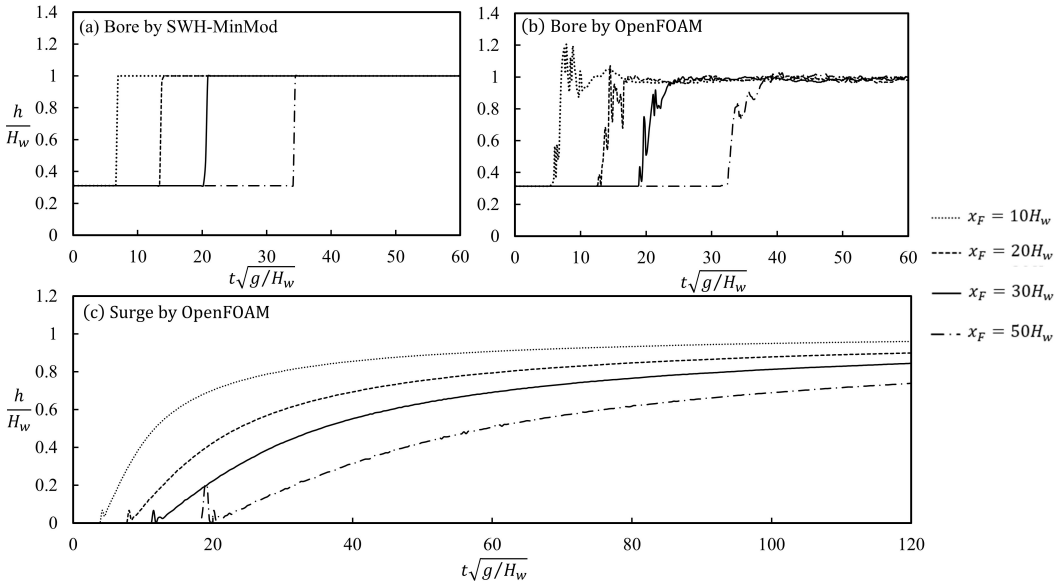

Figure 2–3: Transient-depth profiles by the numerical simulations for wet-bed bores and dry-land surges obtained before their impact on the structures at location $x_F = 10H_w, 20H_w, 30H_w$ and $50H_w$. (a) Bore profiles obtained by the SWH-MinMod simulation. (b) Bore profiles by the OpenFOAM simulation. (c) Surge profiles by the OpenFOAM simulation. The inflow depth and velocity at the inlet were $H_w = 3.215$ m and $U_w = 5.616$ m/s, respectively. The bore advanced onto still water of depth $H = 1$ m. The corresponding wave Froude number was $\mathrm{Fr}_w = 1.0$.

The numerical simulations were conducted by specifying an inflow depth H_w and velocity U_w at the inlet of the computational domain. The structures were located at a distance L from the inlet. We show the transient profile of the bores and the surges at various locations x_F along the channel before their impact on the structures in Figure 2–3.

For the bores, the SWH-MinMod simulations captured perfectly the discontinuity across the front. The OpenFOAM, on the other hand, produced amplitude oscillations of the bores in the region near the inlet. The impact forces on the structures would be affected by the oscillations if the structures were located too close to the inlet. The simulations for various structure locations ($L/H_w = 10$, 20, 30 and 50) are presented later, in sections 4 and 5.

For the dry-land surges, the OpenFOAM simulations provided a gradual rise of the water depth from zero to H_w. The rate of rise depends on x_F/H_w. Figure 3 (c) shows the transient depth profiles of dry-land surges before their impact on structures. The simulations for the impact force produced by the dry-land surges are presented later, in Section 7.

2.4 Impact Force of Wet-bed Bores on a Vertical Wall

The first series of our numerical simulations was for the impact forces of the bores on a vertical wall. We conducted SWH-MinMod simulations to reproduce the SWH-WALL solution derived in Section 2.2, and the OpenFOAM simulations for the non-hydrostatic effect.

Figures 2–4 and 2–5 show the impact by the wet-bed bore for the wave Froude numbers $\mathrm{Fr}_w = 0.6$ and 1.6, respectively. The location of the wall in these two simulations was $L/H_w = 30$, which was sufficiently far away from the inlet for the results not to be affected by the initial oscillations of the bores' amplitude near the inlet.

On the whole, the free surface profiles produced by the SWH-MinMod simulations (red dashed curves) are in agreement with the profiles obtained by the OpenFOAM simulations (white solid curves) both before and after the impact of the wave on the wall. Before the impact, as shown in figures 2–4(a) and 2–5(a), the wave advancing on the wet bed was a bore with a relatively steep wave front. The depth of water behind the wave front of the bore stayed close to the depth H_w in the simulations because the initial still-water depth was specified to satisfy the compatibility condition. Figures 2–4(b) and 2–5(b) show the wave at the instant when the water in front of the wall rose to maximum run-up height, $R_{\max}$. At this instant of maximum run-up, the pressure on the wall was below hydrostatic and the force on the wall was much

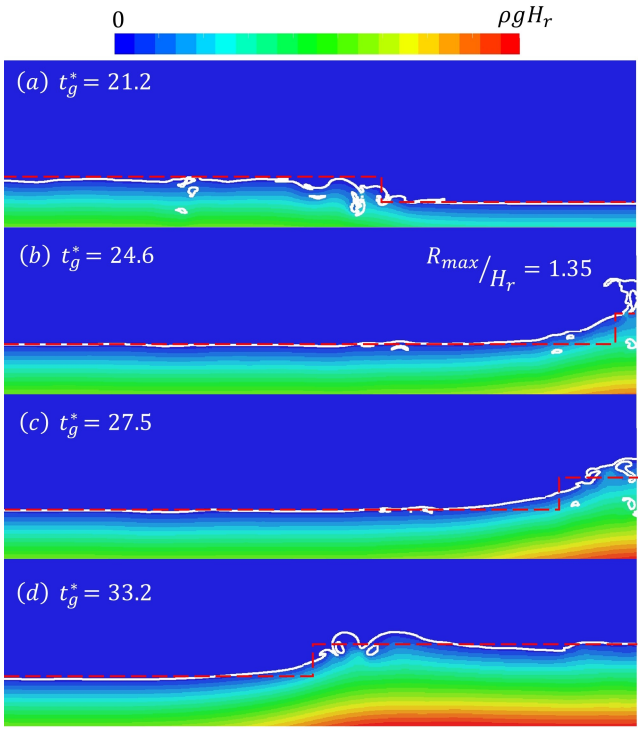

Figure 2–4: Sequence of images showing pressure distribution of a bore on a wet bed ($\mathrm{Fr}_w = 0.6$) impacted on a wall (at location $L/H_w = 30$) at dimensionless times $t_g^* = t\sqrt{g/H_w} = 21.2$, 24.6, 27.5 and 33.2. The color bar on top defines the pressure range from atmospheric pressure (blue) to $\rho g H_r$ (red). The white lines define the air-water interfaces where the phase fraction obtained from the OpenFOAM simulation is 50%. The red-colored dashed lines are the free water surface obtained by the SWH-MinMod simulation.

below the force's maximum. According to the SWH-WALL solution (Equation 2.7), the heights of the upstream propagating bore were $H_r = 0.988$ m and 5.545 m for $\mathrm{Fr}_w = 0.6$ and 1.6, respectively. The maximum run-up height on the front face of the wall – obtained by OpenFOAM simulations – were higher, with $R_{\max} = 1.35 H_r$ and $R_{\max} = 1.28 H_r$ at the times $t_g^* = 21.2$ and 15.3 for the $\mathrm{Fr}_w = 0.6$ and 1.6, respectively.

The pressure on the wall was below hydrostatic at the initial impact as the water accelerated rapidly upward along the wall. The forces did not reach their peak values until later, at times $t_g^* = 27.5$ and 20.8, when the water fell back along the wall – as shown in figures 2–4(c) and 2–5(c), respectively.

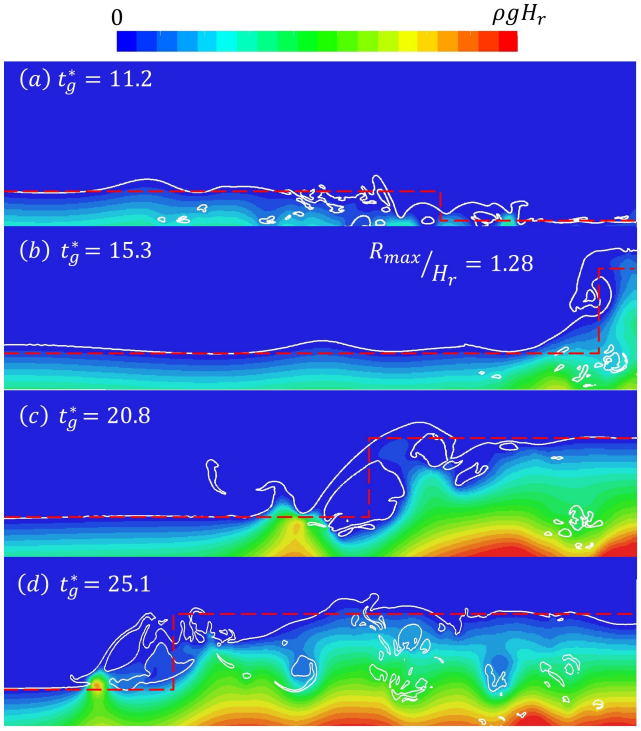

Figure 2–5: Sequence of images showing pressure distribution of a bore on wet bed ($\mathrm{Fr}_w = 1.6$) impacted on a wall (at location $L/H_w = 30$) at dimensionless times $t_g^* = t\sqrt{g/H_w} = 11.2$, 15.3, 20.8 and 25.1. Description for the symbols have been provided in the caption of Figure 2–4.

The upstream propagation of the reflecting bore was closely predicted by the SWH-MinMod simulations. Eventually, the pressure on the wall became hydrostatic as the total force on the wall was in equilibrium with the upstream propagating bore.

2.4.1 Peak Coefficient and Duration of Exceedance

Figures 2–6(a), 2–6(b) and 2–6(c) show the transient variations of the wave-drag coefficients obtained by the OpenFOAM simulations for $\mathrm{Fr}_w = 0.6$, 1.0 and 1.6, respectively. The wave-drag coefficient rose to a peak $\hat{C}_D$ and then settled on to the SWH-WALL value $\overline{C}_D$. Simulations were conducted using different lengths of the channel $L/H_w = 10$, 30 and 50, as shown in the figure. Table 2–2 summarizes the condition of the simulation.

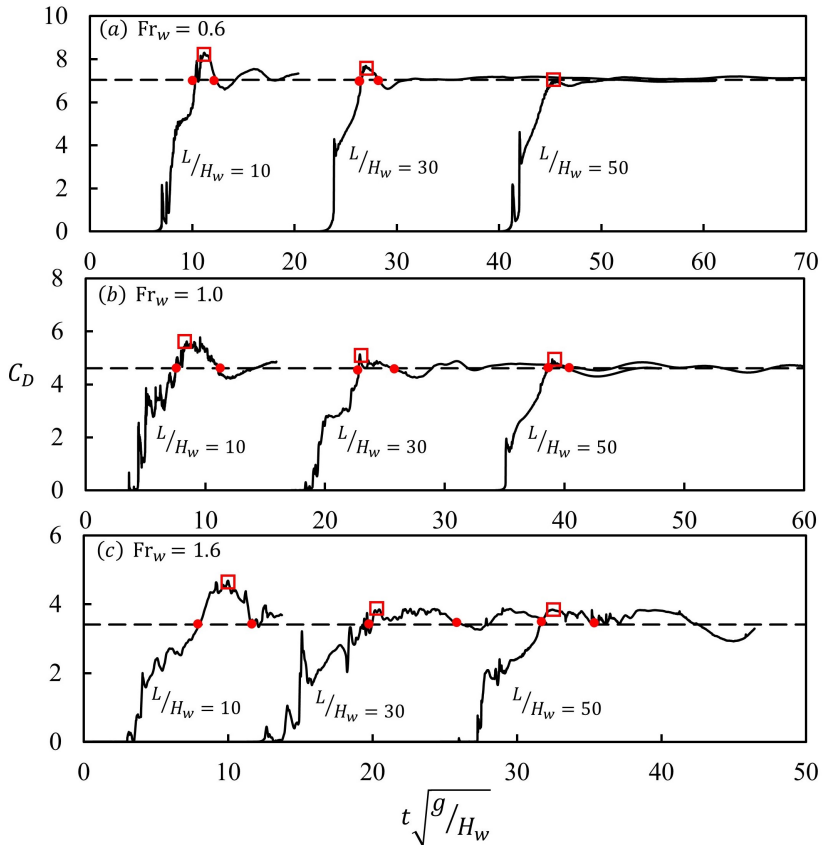

Figure 2–6: Transient variation of the wave-drag coefficient C_D with the time $t\sqrt{g/H_w}$ for three different channel lengths $L/H_w = 10$, 30 and 50; (a) $\mathrm{Fr}_w = 0.6$, (b) $\mathrm{Fr}_w = 1.0$ and (c) $\mathrm{Fr}_w = 1.6$. The dashed lines mark the value of the SWH-WALL solution for $\overline{C}_D$ determined by equations 2.7 and 2.9. The square symbol marks the peak value $\hat{C}_D$. The red dots are the intersections when $C_D = \overline{C}_D$.

Figure 2–7(a) shows the peak value of the wave-drag coefficient $\hat{C}_D$ to the SWH-WALL value $\overline{C}_D$. The open symbols denote the values obtained from the OpenFOAM simulations of $\mathrm{Fr}_w = 0.6$, 1.0 and 1.6, respectively, with the L/H_w varying from 10 to 50. The solid symbols represent the laboratory data by Robertson et al. (2013). The ratio of the wave-drag coefficient can be as high as $\hat{C}_D/\overline{C}_D \simeq 1.35$ when the length of the channel is as small as $L/H_w \simeq 10$. On the other hand, the peak would be quite insignificant and the value of $\hat{C}_D$ practically equal to $\overline{C}_D$ if the bore had traveled a distance beyond $L/H_w \simeq 30$ before its impact on the wall.

Table 2–2: The condition and results of the numerical simulations for the bore impact on a vertical wall.

Symbol	Fr_w	$\hat{C}_D$	$\hat{T}_g$	H (m)	H_w (m)	U_w (m/s)	L (m)	$\Delta x, \Delta y$ (m)	$\hat{C}_D/\overline{C}_D$	L/H_w
□	0.6	8.25	2.04	0.3	0.59	1.44	5.9	0.02	1.17	10
□	0.6	7.68	1.75	0.3	0.59	1.44	11.8	0.02	1.09	30
□	0.6	7.00	0.00	0.3	0.59	1.44	17.7	0.02	1.00	50
◊	1.0	5.77	3.64	0.3	0.96	3.07	14.5	0.02	1.25	10
◊	1.0	5.13	1.77	0.3	0.96	3.07	29.0	0.02	1.10	30
◊	1.0	4.94	2.23	0.3	0.96	3.07	38.5	0.02	1.07	50
△	1.6	4.66	4.05	0.3	1.88	6.86	16	0.02	1.37	10
△	1.6	3.85	3.77	0.3	1.88	6.86	60	0.02	1.13	30
△	1.6	3.81	4.01	0.3	1.88	6.86	120	0.02	1.12	50

The period of time when the force exceeds the SWH-WALL value is the duration of exceedance $\hat{T}_g$. It was determined as the time between intersections when $C_D = \overline{C}_D$, as shown in Figure 2–6 . Figure 2–7(b) shows the dimensionless duration of exceedance $\hat{T}_g\sqrt{g/H_r}$. The average was $\hat{T}_g\sqrt{g/H_r} \simeq 2$ with a detectable tendency for this to decrease slightly with the increase of L/H_w. The intersection when $C_D = \overline{C}_D$ were not determined with complete certainty.

2.4.2 Comparison with Laboratory Experiment

Ramsden (1996) and Robertson et al. (2013) have conducted laboratory experiments to determine the impact of a tsunami wave on a vertical wall. Ramsden (1996) recognized the difference in the profiles between the bores on wet beds and the surges on dry land, and also the difference in the impact of these waves on the wall. However, we were not able to extract enough information from the experiments by Ramsden (1996) to compare his results with our simulations.

The experiments of Robertson et al. (2013) were conducted in a 84-m-long flume. In their experiments, solitary waves of heights up to 1.3 m ran up a 1:12 sloping beach, and broke to form bores on a flat reef. Table 2–3 summarizes the conditions and the results of these laboratory experiments.

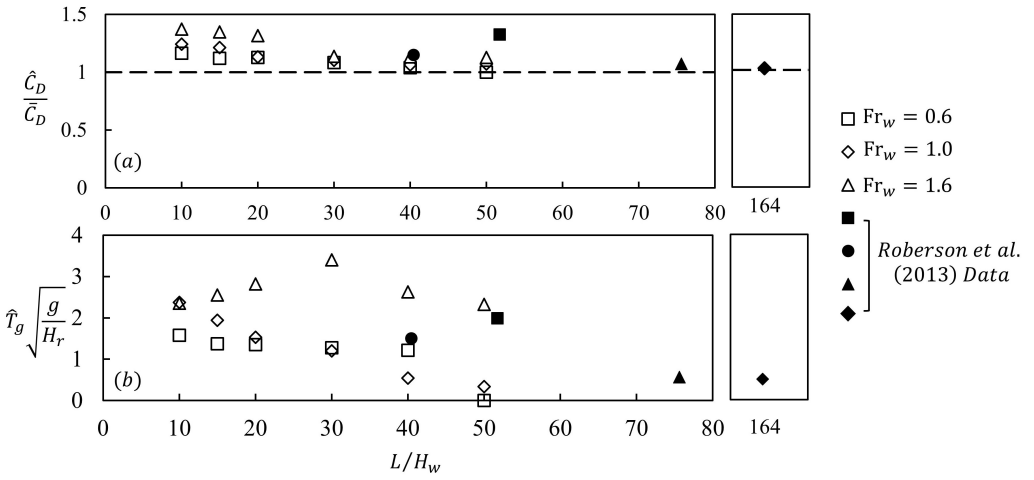

Figure 2–7: (a) The ratio of the peak wave-drag coefficient $\hat{C}_D$ over the coefficient $\overline{C}_D$ obtained from the SWH solution. (b) Duration of exceedance when the wave-drag coefficient $\hat{C}_D$ is above the SWH solution $\overline{C}_D$. One point from the data of Robertson et al. (2013) for L/H_w= 164 is shown in the separate box on the right. Symbols are defined on the right-hand side of the figure and in tables 2–2 and 2–3.

Table 2–3: Experimental data of Robertson et al. (2013).

Symbols	Fr_w	$\hat{C}_D$	$\hat{T}_g$	H (m)	H_w (m)	U_w (m/s)	L (m)	$\hat{C}_D/C_D$	L/H_w
■	0.55	11.42	1.98	0.3	0.56	1.28	28.7	1.49	51
●	0.75	7.09	1.50	0.3	0.71	1.98	28.7	1.22	40
◆	1.05	4.61	1.01	0.05	0.18	1.35	28.7	1.03	159
▲	1.80	3.52	0.99	0.05	0.38	3.48	28.7	1.10	76

The bore in the experiment of Robertson et al. (2013) traveled on the flat reef in water of depths that varied from $H = 0.05$ m to 0.3 m over the reef of length $L = 28.5$ m before its impact on the wall. Robertson et al. (2013) measured the wave height H_w and the celerity c over an 8-m distance in front of the wall. We used the continuity equation and their measurements to calculate the inflow velocity $U_w = c(1 - H/H_w)$. The peak wave-drag coefficient $\hat{C}_D$ and the duration of exceedance $\hat{T}$ for the wave on a wet bed extracted from the data published by Robertson et al. (2013) are included in Figure 2–7.

The dependence of the wave-drag coefficient on the wave Froude number in Robertson et al. (2013) follows remarkably close to the SWH-WALL solution, and to the results obtained by the OpenFOAM simulations as shown in Figure 2–8.

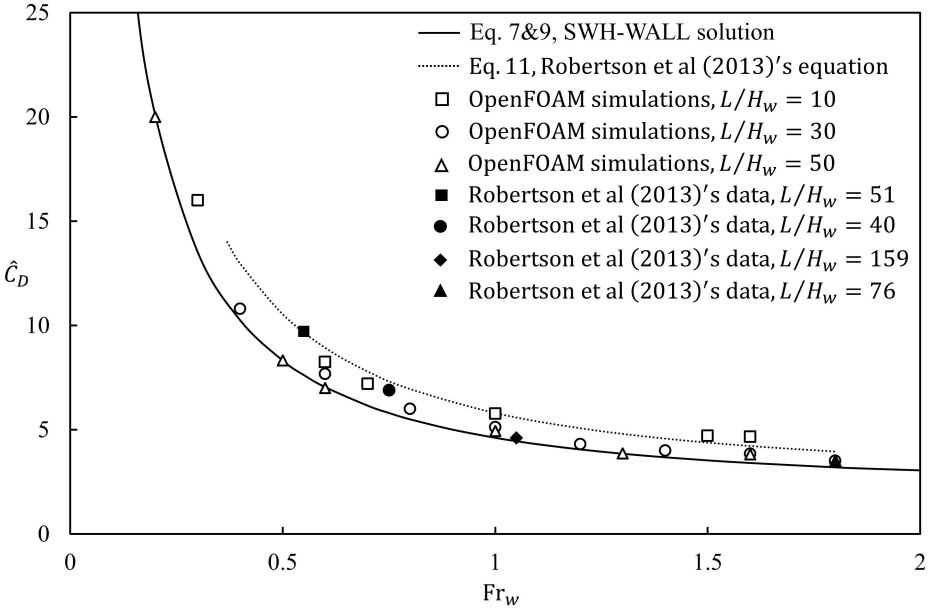

Figure 2–8: The peak values of the wave-drag coefficient $\hat{C}_D$ obtained by OpenFOAM simulations compared with the laboratory data by Robertson et al. (2013). The open symbols denote the OpenFOAM simulation results obtained in channel lengths $L/H_w = 10.$ 30 and 50. Solid symbols are the laboratory data of Robertson et al. (2013). The solid line is the SWH-WALL solution defined by Equations 2.7 and 2.9. The dot-dot line is the Equation 2.11 derived by Robertson et el. (2013) to fit their data.

The formula proposed by Robertson et al. (2013) was for the force on the front face of the wall $\hat{F}_F$. The corresponding peak wave-drag coefficient for the front face of the wall is

$$\hat{C}_{DF} = \frac{\hat{F}_F}{\frac{1}{2}\rho U_w^2 A_w} = \mathrm{Fr_w^{-2}} + \frac{2\mathrm{H_w}}{\mathrm{H_w - H}} + 2\mathrm{Fr_w^{-\frac{2}{3}}} \tag{2.10}$$

Subtracting the initial hydrostatic pressure on the back of the block gives

$$\hat{C}_D = \mathrm{Fr}_w^{-2}(1 - \frac{H^2}{H_w^2}) + \frac{2H_w}{H_w - H} + 2\mathrm{Fr}_w^{-\frac{2}{3}} \tag{2.11}$$

This empirical formula, derived from experimental observation, gave a slightly greater value for $\hat{C}_D$ than the SWH-WALL solution.

2.4.3 Correlation of Wave Drag Coefficient with Froude Number

Figure 2–8 shows the overall comparison of the OpenFOAM simulation results with the experimental data of Robertson et al. (2013), the empirical formula (dotted line, Equation 2.11) of Robertson et al. (2013), and the SWH-WALL solution (solid line, Equations 2.7 & 2.9). Those peak coefficients $\hat{C}_D$, obtained from the OpenFOAM simulations for $L/H_w \geq 50$, were remarkably close to the SWH-WALL coefficient $\overline{C}_D$ determined by Equations 2.7 & 2.9. Those data of Robertson et al. (2013) obtained for $L/H_w = 76$ and 159 were also close to the SWH-WALL wall coefficient $\overline{C}_D$. For $L/H_w = 50$, the ratios $\hat{C}_D/\overline{C}_D$ obtained from the OpenFOAM simulation were 1.00, 1.07 and 1.12 for $\mathrm{Fr}_w = 0.6$, 1.0 and 1.6, respectively. For $L/H_w = 76$ and 159 in the laboratory experiments of Robertson et al. (2013), the ratios $\hat{C}_D/\overline{C}_D$ were 1.03 and 1.10 for $\mathrm{Fr}_w = 1.80$ and 1.05, respectively. Summary of these simulation and experimental results are provided in Tables 2–2 and 2–3.

The comparison in Figure 2–8 has suggests that the SWH-WALL solution would be a good approximation if the bore front were moderately steep. As explained in Section 2.3, the moderately steep front of a quasi-similar state can be loosely defined in the OpenFOAM simulation when the bore has advanced a distance greater than $x_F \simeq 30H_w$. In the experiment by Robertson et al. (2013), the quasi-similar state was apparently attained when the bore on the flat reef had advanced over a distance greater than $L \simeq 50H_w$.

In our OpenFOAM simulation (see Figure 2–3), the amplitude of the bore was greater than H_w in the region close to the inlet. Apparently, the amplitudes of the bore were also greater at the inlet of the reef in the experiment of Robertson et al. (2013). The greater bore amplitude may explain why the coefficient $\hat{C}_D$ was generally higher in value for those simulation data obtained near the inlet in our simulations, and in the experimental data obtained near the entrance to the reef by Robertson et al. (2013).

2.5 Impact Forces of Wet-bed Bores on a Structure of Finite Width

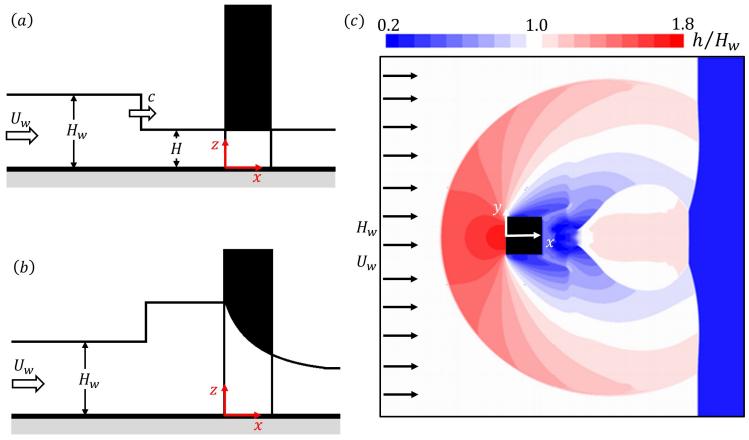

Figure 2–9: (a) Elevation view of the surge wave before its impact on a block. (b) The reflected wave immediately after the impact on the front face of the block. (c) Plane view of the waves on the horizontal x- and y-planes some time after its impact on the block. The wave was produced by an inflow of depth H_s and velocity U_s, parameters that were specified at the entrance to the computational domain.

In this section, we study the scattering of the waves by coastal structures of finite width that are standing in water. The simulation problem is defined in the sketch shown in Figure 2–9. The structure is a square block of width W. In the simulations, the inflow depth H_w and velocity U_w were selected to be compatible with the initial water depth H so that the wave in the form of a bore could advance toward the structure relatively unchanged before its

impact on the structure. The width of the channel W_{ch} was selected to be 10 times wider than the width of the block W, so that the side-wall effect would be negligible. Simulations were conducted first by a 2D SWH-MinMod method using the depth-averaged equations, and then by a 3D OpenFOAM method using the full set of equations covering a full range of conditions of wave Froude number, varying from $\text{Fr}_w = 0.2$ to 2.0, and width-to-depth ratio from $W/H_w = 1$ to 25.

2.5.1 Scattering of Waves by a Large Structure

We begin first with the limiting case of a very large structure. For this limiting case, the width of the structure was selected to be 25 times greater than the height of the incoming wave. With $W/H_w = 25$, the waves around the structure were in shallow water, as the depth of the water was small compared with the horizontal length of the waves. Under this shallow-wave condition, the 3D and 2D simulations were expected to produce similar wave motions. The initial impact of a wave on a very large structure is similar to the impact on a wall, as the wall is a structure of infinite width. The peak wave-drag coefficient $\hat{C}_D$ produced by the initial impact therefore was expected to be comparable in value to the wall coefficient $\overline{C}_D$.

Figure 2–10 shows the scattering waves around the square block obtained from the 2D SWH-MinMod simulations for wave Froude numbers $\text{Fr}_w = 0.4$, 1.0 and 1.6, respectively. Figure 2–11 shows the same waves with the same wave Froude numbers obtained by 3D OpenFOAM® simulations. Table 2–4 summarizes the conditions and results of the simulations. The mesh sizes were $\Delta x = \Delta y = 1.0$ m in the 2D SWH-MinMod simulations, and $\Delta x = \Delta y = 0.5$ m and $\Delta z = 0.1$ m in the 3D OpenFOAM simulations.

Table 2–4: Peak coefficients $\hat{C}_D$ and maximum run-up heights $R_{\max}$ obtained by 3D OpenFOAM simulations and 2D SWH-MinMod simulations for large structures standing in water; $W = 25H_w$, $W_{\text{ch}} = 10W$ and $H = 1$ m. These numerical simulation results are compared with the corresponding values of $\overline{C}_D$ and H_r determined by the SWH-WALL solution (Eqs. 2.7 & 2.9) for the bore impact on a wall.

			OpenFOAM		SWH-MinMod		SWH-WALL solution	
Fr_w	H_w (m)	U_w (m/s)	$\hat{C}_D$	$R_{\max}$ (m)	$\hat{C}_D$	$R_{\max}$ (m)	$\overline{C}_D$ (Eqs. 2.7 & 2.9)	H_r (Eq. 2.7)
0.4	1.55	1.56	10.2	2.40	10.26	2.24	10.246	2.22
1.0	3.20	5.62	4.65	8.80	4.61	6.98	4.612	6.98
1.6	6.25	12.53	3.39	22.41	3.41	18.53	3.403	18.50

The 2D SWH-MinMod simulations captured well the sharp discontinuities across the wave fronts of the scattering waves shown in Figure 2–10. The color bars in Figures 2–10 (a), 2–10(b) and 2–10(c) define the ranges of depth variation, which were (a) from $h/H_w = 0.85$ to 1.15, (b) from $h/H_w = 0.2$ to 1.8 and (c) from $h/H_w = 0.0$ to 2.0.

The 3D OpenFOAM simulations produced similar scattering patterns, which in Figure 2–11 were defined by the normalized bottom pressure, $p/(\rho g H_w)$. The pressure over the depth is not exactly hydrostatic, but the normalized pressure $p/(\rho g)$ is an approximation of the water depth. The ranges of variation of $p/(\rho g H_w)$ obtained from the 3D OpenFOAM, as defined by the color bars in Figure 2–11 were the same as those for the water depth h in Figure 2–10.

2.5.2 Run-up Height and Wave Drag Coefficient

The run-up height R is the water level on the front face of the block at $x = y = 0$. The run-up height, R, divided by the bore height, H_w, obtained by the simulations are plotted on Figure 2–10(d) and Figure 2–11 (d) for the $\text{Fr}_w = 0.4$, 1.0 and 1.6, respectively. The run-up height rose rapidly to a peak $R_{\max}$

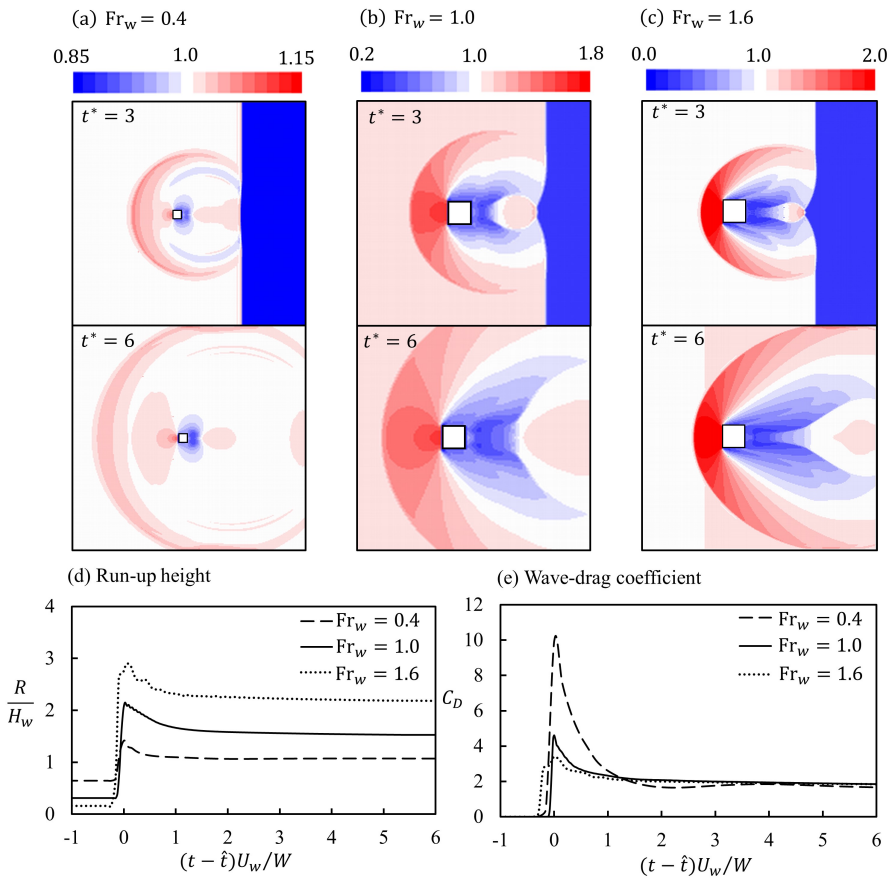

Figure 2–10: 2D SWH-MinMod simulation of the impact of wet-bed bores on a square block. (a)(b)(c) Depth h/H_w contours on the x-y plane at time $t^* = (t-\hat{t})U_s/W = 3$ and at a later time $t^* = 6$, (d) variations of wave run-up height R/H_w with time t^* and (e) variations of wave-drag coefficient C_D with time t^* for wave Froude numbers $\mathrm{Fr}_w = 0.4$, 1.0 and 1.6 and width-to-depth ratio $W/H_w = 25$. The color bars above the depth contours define the range of h/H_w. The wave-drag coefficient rose to its peak $\hat{C}_D$ at time $t = \hat{t}$; that is, at $t^* = 0$.

on impact by the bore, and then settled to a relatively constant level as the scattering wave reached an equilibrium wave state. For the large structure with $W = 25H_w$, the maximum run-up height $R_{\max}$ obtained from the simulations are remarkably close to the reflected wave height H_r determined by the SWH-WALL solution, Equation 2.7. Table 2–4 shows the values of the maximum run-up heights $R_{\max}$ obtained by the simulations and the value of H_r given by the SWH-WALL solution.

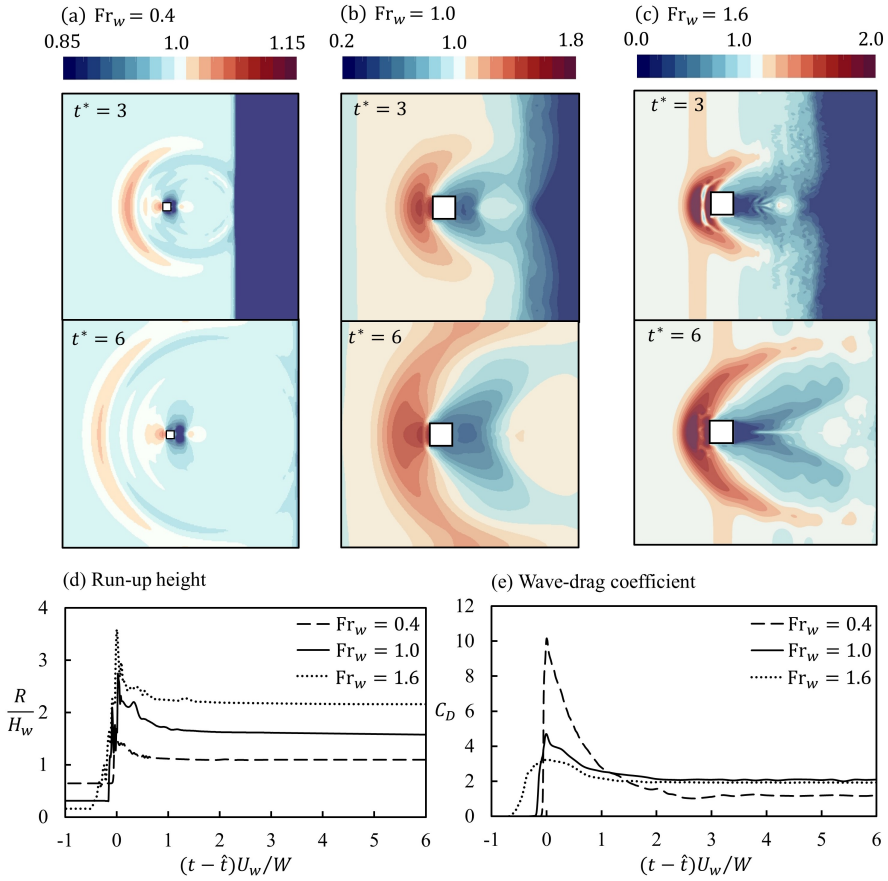

Figure 2–11: 3D OpenFOAM simulations of the impact of wet-bed bores on a square block. (a)(b)(c) Bottom pressure $p/(\rho g H_w)$ contours on the x-y plane at time $t^* = (t-\hat{t})U_s/W = 3$ and at a later time $t^* = 6$, (d) variations of wave run-up height $R/H_w$with time t^* and (e) variations of wave-drag coefficient C_D with time t^* for wave Froude numbers $\mathrm{Fr}_w = 0.4$, 1.0 and 1.6 and width-to-depth ratio $W/H_w = 25$. The color bars above the bottom pressure contours define the range of $p/(\rho g H_w)$. The wave-drag coefficient rose to its peak $\hat{C}_D$ at time $t = \hat{t}$; that is, at $t^* = 0$.

The wave-drag coefficient also rose to a peak $\hat{C}_D$ and then settled to a relatively constant value of $\tilde{C}_D$. Over the period from time $t^* = (t-\hat{t})U_w/W = 3$ to 6, waves were continuously radiating away from the structure. The water level set up by the wave radiation around the structure remained relatively constant. The wave-drag on the structure was also relatively constant. The wave-structure interaction over this period of time may be considered to have reached an equilibrium state.

For the large structure with $W = 25H_w$, the peak coefficient $\hat{C}_D$ obtained from the 3D OpenFOAM simulations and 2D SWH-MinMod simulations were nearly the same. Both were approximately equal to the wall value given by the SWH-WALL solution, Equations 2.7 and 2.9. Table 2–4 also provides the comparison between the value of the peak coefficient $\hat{C}_D$ obtained from our simulation and the wall value $\overline{C}_D$ given by the SWH-WALL solution, Equations 2.7 and 2.9.

The mesh sizes on the x and y planes used in the 3D OpenFOAM and the 2D SWH-MinMod simulations were comparable, but the computational requirement for the 3D simulation was an order of magnitude greater. The 2D simulation is less demanding of computational resources, and would be preferable in practice for large structures in shallow water when the width-to-depth ratio $R = W/H_s$ is sufficiently large. The 2D SWH-MinMod simulations capture the discontinuities across the shock-wave fronts by the second-order MinMod flux-limiting scheme. This method is efficient, reliable and widely accepted for engineering applications. Implementation of the method has been described by Karimpour and Chu (2014, 2015, 2016) and Brunner (2016).

2.5.3 Duration of Exceedance

The period of time when the force coefficient exceeds the wave-structure interaction equilibrium $\tilde{C}_D$ is the duration of exceedance, $\hat{T}$, which is twice the period of time that the C_D exceeds $[\tilde{C}_D + \frac{1}{2}(\hat{C}_D - \tilde{C}_D)]$. The dimensionless duration $\hat{T}U_w/W$, estimated from the transients in Figure 2–10(d) from the 2D SWH-MinMod simulation were $\hat{T}U_w/W = 0.80$, 0.76 and 1.22 for $\mathrm{Fr}_w = 0.4$, 1.0 and 1.6, respectively. The dimensionless duration $\hat{T}U_w/W$, estimated from the transients in Figure 2–11(d) from the 3D OpenFOAM simulations were $\hat{T}U_w/W = 1.41$, 1.02 and 1.17 for $\mathrm{Fr}_w = 0.4$, 1.0 and 1.6, respectively. The

average value is $\hat{T}U_w/W \simeq 1.2$ which is slightly greater than the value obtained by the 2D SWH-MinMod simulations.. In terms of the Froude number, this duration of exceedance is

$$\hat{T} \simeq 1.2\frac{W}{\mathrm{Fr}_w\sqrt{gH_w}}. \tag{2.12}$$

For the example of a surge-wave height $H_w = 5$ m and a Froude number $\mathrm{Fr}_w = 1.0$, the duration of exceedance would be about $\hat{T} \simeq 17$ s if the width of the structure were $W = 100$ m; the duration of exceedance would be only $\hat{T} \simeq 0.17$ s if the width of the structure were 1 m. The force in the initial impact may be huge, but the impulse would be significant only if the width of the structure were sufficiently large.

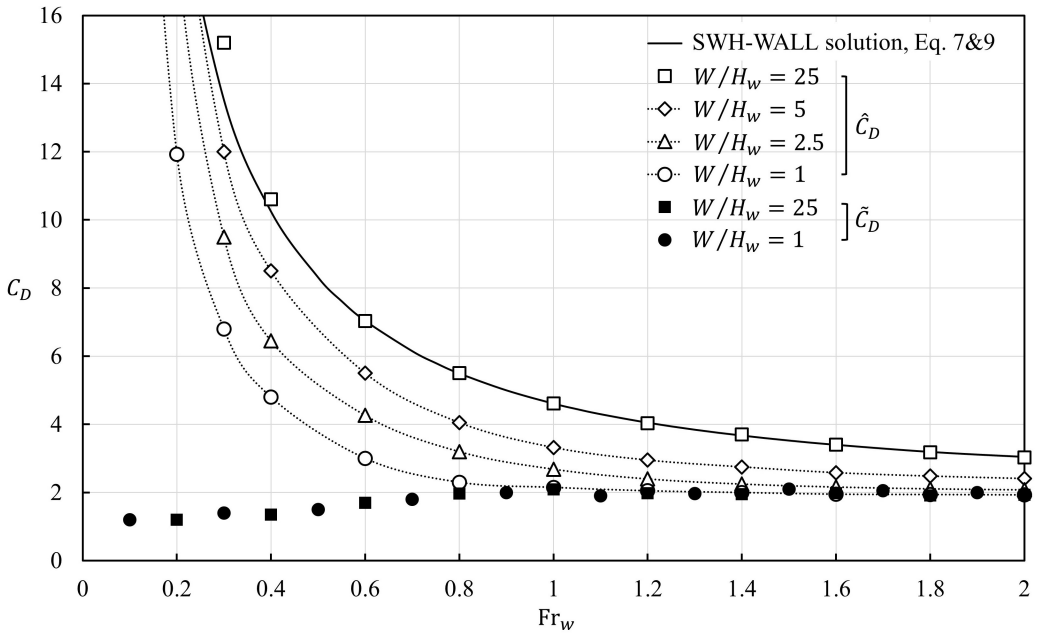

Figure 2–12: Wave drag coefficient for the block standing in water. Open symbols denote the peak value of $\hat{C}_D$ while the solid symbols denote the wave-structure-interaction equilibrium value of $\tilde{C}_D$; the square, the diamond, the triangle and the circle are the symbols for the width-to-depth ratios $W/H_s =$ 25, 10, 5 and 1, respectively. The solid line is the SWH-WALL solution, equations 2.2 and 2.7, for a structure of infinite width.

2.5.4 Dependence on Froude Number and Width-to-depth Ratio

To examine the general dependence of the waves on the Froude number of the waves and width-to-depth ratio of the structure, 3D OpenFOAM simulations were conducted to cover the entire range of wave Froude numbers, varying from $\mathrm{Fr}_w = 0.2$ to 2.0 and the width-to-depth ratio of the structure from $W/H_w = 1$ to 25. 3D OpenFOAM simulations were necessary because the flow around the structure was three-dimensional for small structures with small W/H_w. Figure 2–12 summarizes the results of a large number of simulations. The open symbols in the figure denote the value of the peak coefficient $\hat{C}_D$, while the solid symbols define the equilibrium value of $\tilde{C}_D$ for the wave-structure interaction equilibrium. Remarkably, the equilibrium coefficient $\tilde{C}_D$ is relatively independent of the size of the structure. For large structures, where W/H_w is equal to or greater than 25, the peak coefficient $\hat{C}_D$ is approximately equal to wall coefficient $\overline{C}_D$ that are defined by the solid line in the figure and Equations 2.7 and 2.9 of the SWH-WALL solution. The peak progressively becomes less significant. As the W/H_w approaches the value of unity, the value of the peak coefficient $\hat{C}_D$ is practically the same as the equilibrium coefficient $\tilde{C}_D$.

2.5.5 Comparison with Laboratory Experiment

The 3D OpenFOAM simulations was validated by comparison of the simulation results with the measurements of the wave force on structures in the laboratory by Arnason et al. (2009). Waves, in the form of bores impacted on a square block, were produced in the experiment of Arnason et al. (2009) by sudden removal of a gate in a 16-m-long channel. The gate was 5.9 m from the upstream end-wall. The width of the channel was $W_{ch} = 0.6$ m, which was five times the width of the square block $W = 0.12$ m. Figure 2–13(a) shows the

wave forces obtained by the 3D OpenFOAM simulations. These are included to allow comparison with the laboratory profiles shown on the right-hand side of the figure in (b).

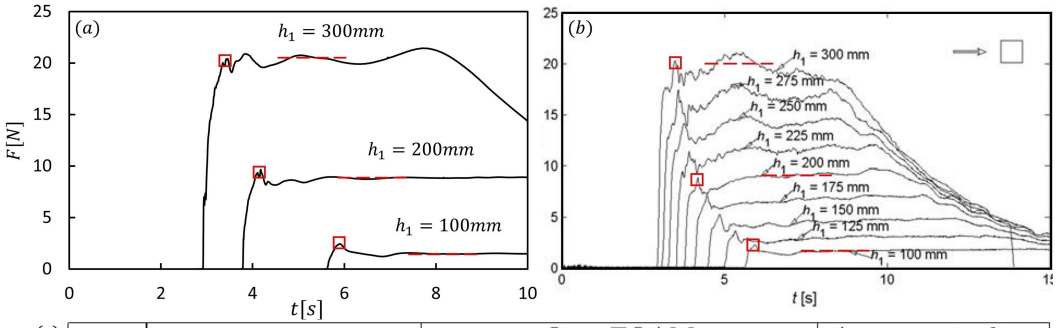

(c)

				OpenFOAM				Arnason et al.	
Fr_w	H_w (m)	W (m)	W/H_w	$\Delta x, \Delta y$ (m)	Δz (m)	$\hat{F}$ (N)	$\tilde{F}$ (N)	$\hat{F}$ (N)	$\tilde{F}$ (N)
0.81	0.050	0.12	2.40	0.005	0.005	2.44	1.49	2.4	1.5
1.20	0.079	0.12	1.52	0.005	0.005	9.66	8.85	8.9	8.9
1.41	0.103	0.12	1.17	0.005	0.005	20.41	20.51	20.1	20.1

Figure 2–13: The transient variation of the wave force obtained by (a) the 3D OpenFOAM simulations and (b) the laboratory experiments by Arnason et al. (2009). (c) A table summarizing the conditions of the simulations and the wave forces $\hat{F}$ and $\tilde{F}$ obtained by the simulations and the laboratory experiments.

The table in Figure 2–13 (c) summarizes the conditions of the experiments and simulations. Arnason et al. (2009) used the dam-break-wave solution of Ritter (1892) to find the height H_w and the velocity U_w of the bores. The water levels in the reservoir were $h_1 = 0.1$, 0.2 and 0.3 m for three laboratory experiments selected for comparison. The corresponding wave Froude numbers were $\mathrm{Fr}_w = U_w/\sqrt{gH_w} = 0.81$, 1.20 and 1.41, and the width-to-depth ratios were $W/H_w = 2.50$, 1.52 and 1.17, respectively. The mesh sizes used in the numerical simulations were $\Delta x = \Delta y = \Delta z = 0.005$ m. Wall friction was included in the simulations.

The 3D OpenFOAM simulations closely reproduced the wave forces determined in the laboratory. In the figure, the open-square symbol marks the

peak wave force $\hat{F}$, and the dashed line marks the wave force $\tilde{F}$ at the wave-structure interaction equilibrium. The table lists the comparable peak and equilibrium forces, $\hat{F}$ and $\tilde{F}$, obtained by the OpenFOAM simulations and the measurements in the laboratory. The agreement between the numerical simulations and laboratory measurements is remarkable. It speaks to the accuracy of both the simulations and the measurements.

2.6 Impact Forces of Dry-land Surges on a Wall and on a Structure of Finite Width

The water depth of a surge on dry land varies gradually. It starts with a depth H_w and a velocity U_w at the entrance to the computational domain and gradually varies to a zero depth at the leading edge. The velocity at the leading edge is significantly greater than the velocity U_w at the entrance. We present the results of the OpenFOAM simulations first for the impact of the surges on a vertical wall, and then the impact on a structure of width W.

2.6.1 Dry-land Surges on a Vertical Wall

The sequence of images in Figure 2–14 shows OpenFOAM simulations of the surges impacted on a vertical wall for wave Froude number $\mathrm{Fr}_w = 0.4$, 0.6, 1.0 and 1.6 at various dimensionless time $t_g^* = t\sqrt{g/H_w}$. (i) The inflow entered the channel at time t_{g1}^*. (ii) The water in front of the wall rose to its maximum run-up height $R_{\max}$ at time t_{g2}^*. (iii) The water fell back onto the incoming wave at time t_{g3}^*. (iv) The reflected wave began to propagate upstream at time t_{g4}^*. (v) A well-defined bore was observed to form, advancing in the upstream direction, as the wave-drag coefficient rose to its equilibrium value $\tilde{C}_D$ at time t_{g5}^*. The maximum run-up heights on the vertical wall at

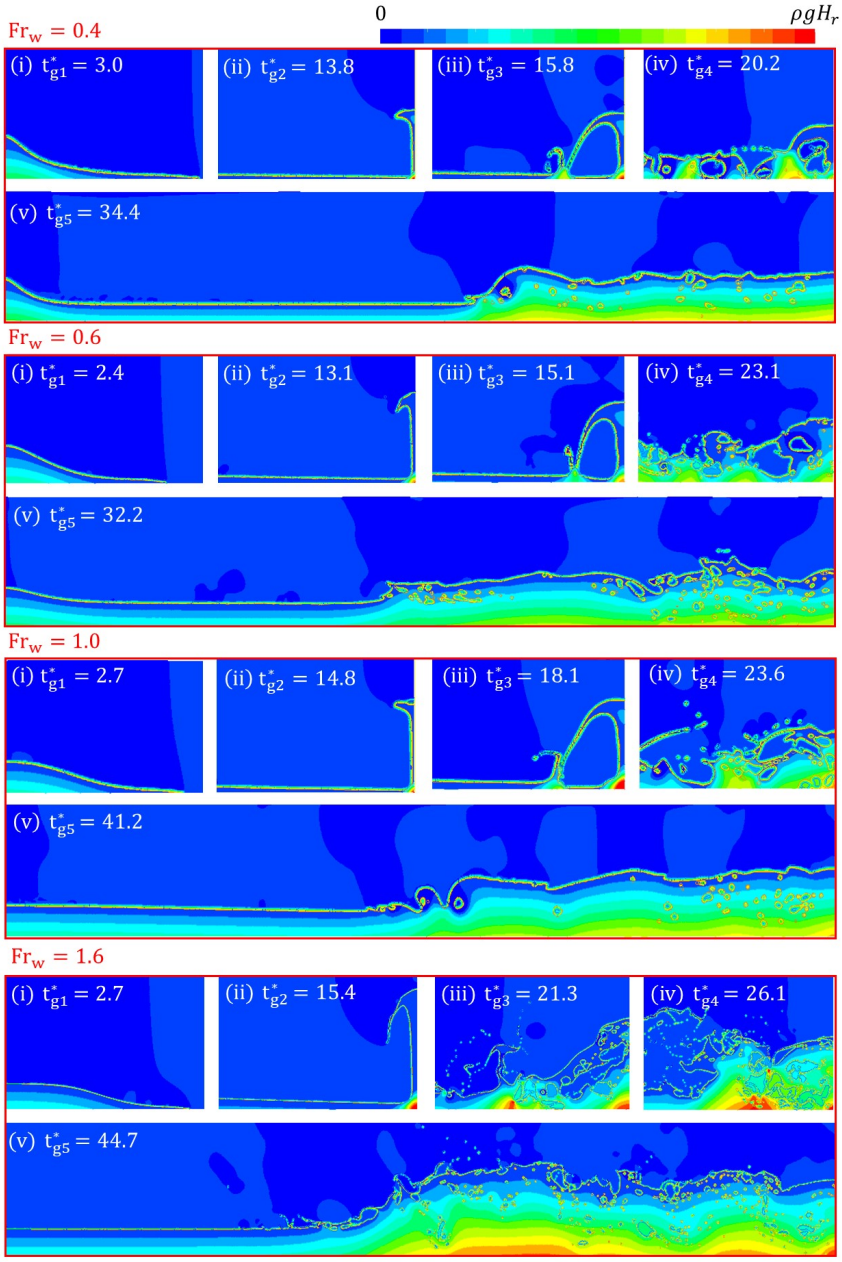

Figure 2–14: Sequence of images showing the surges on dry land at various dimensionless times. For each Froude number, Fr_w = 0.4, 0.6, 1.0 and 1.6, the figure shows the wave profile (i) at time t^*_{g1} when the inflow entered the channel, (ii) at time t^*_{g2} when water in front of the wall rose to its highest level $h_{\max}$, (iii) at time t^*_{g3} when the risen water fell back onto the incoming wave, (iv) at time t^*_{g4} when the reflected wave began to propagate upstream, and (v) at time t^*_{g5} when the wave force on the wall was in equilibrium with the upstream propagating bore.

time $t_g^* = t_{g2}^*$ were $R_{\max} = 1.25H_w, 1.89H_w, 3.01H_w$ and $3.93H_w$ for $\mathrm{Fr}_w = 0.4$, 0.6, 1.0 and 1.6, respectively.

Water run-up achieved great heights on impact with the vertical wall. The pressure on the wall was much below the hydrostatic pressure in the initial impact at time $t_g^* = t_{g2}^*$ when the run-up height reached its maximum $R_{\max}$. Significant upward acceleration of the water along the wall occurred during the initial impact. Large air pockets subsequently formed as the water fell back onto the incoming wave, at time $t_g^* = t_{g3}^*$. The formation of the air pockets and the collapse of the pockets produced pressure oscillations on the wall. The forces on the wall determined by the OpenFOAM simulations increased gradually toward an equilibrium. The equilibrium was not reached until the water and the air pockets organized themselves to form an upstream propagating bore. By the time the forces reached the equilibrium (at time $t_g^* = t_{g5}^*$), most of the trapped air had escaped from the upstream propagating bore.

Figure 2–15 shows the transient variation as the wave-drag coefficient rose toward the equilibrium value. The approach to equilibrium delineated by the red-colored lines was gradual for the dry-land surges. The wave-drag coefficient of the dry-land surge did not have a distinct peak. It fluctuated initially and increased gradually toward the equilibrium value $\tilde{C}_D$. This is compared with the initial sharp increase to the peak and then settling to the equilibrium defined by the black-colored lines for the bores on the wet bed. The equilibrium $\tilde{C}_D$ for the dry-land surges is marked in the figure by the red-colored square symbol. The time scale was $\sqrt{H_w/g}$. The time for the force of the bore to rise to its peak was about 3 to 5 $\sqrt{H_w/g}$. The force produced by the dry-land surge rose gradually. The time for the force of the dry-land surge to attain equilibrium was about 30 $\sqrt{H_w/g}$.

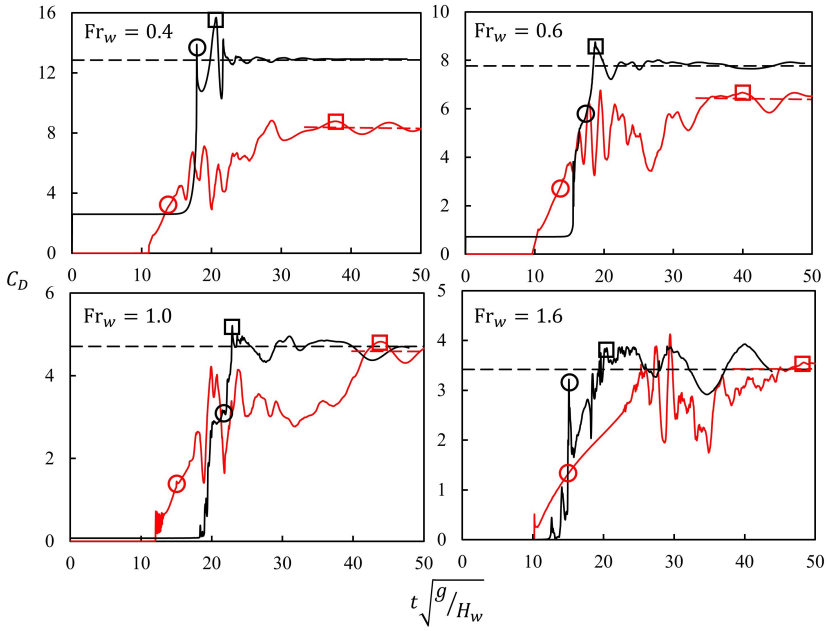

Figure 2–15: Transient development of the wave drag coefficient for dry-land surges (red) compared with the coefficient for the wet-bed bores (black). For the wet-bed bore, the square symbol marks the peak coefficient $\hat{C}_D$. For the dry-land surges the square symbol marks the equilibrium coefficient $\tilde{C}_D$. The circle symbol marks the instant when the water level on the wall rose to its maximum run-up height $R_{\max}$. The length of the channel from the inlet to the wall is $L = 30H_w$.

The transient variation of the force on the wall was not directly related to the water level in front of the wall. The wave-drag coefficient at the instant when the water level reached its maximum run-up height $R_{\max}$, as marked by the open-circle symbol in Figure 2–15, was generally much smaller than the peak $\hat{C}_D$ and the value of $\tilde{C}_D$ at equilibrium.

Figure 2–16 shows the dependence of the equilibrium coefficient $\tilde{C}_D$ on the wave Froude number Fr_w for $L/H_w = 10$, 30 and 50. The best fit of the wave-drag coefficient $\tilde{C}_D$ for the sufficiently long channel with $L/H_w = 30$ and 50, denoted by the open-circle and open-triangle symbols in the figure, is

$$\tilde{C}_D = 1.7 + \frac{2.55}{\mathrm{Fr_w}} \tag{2.13}$$

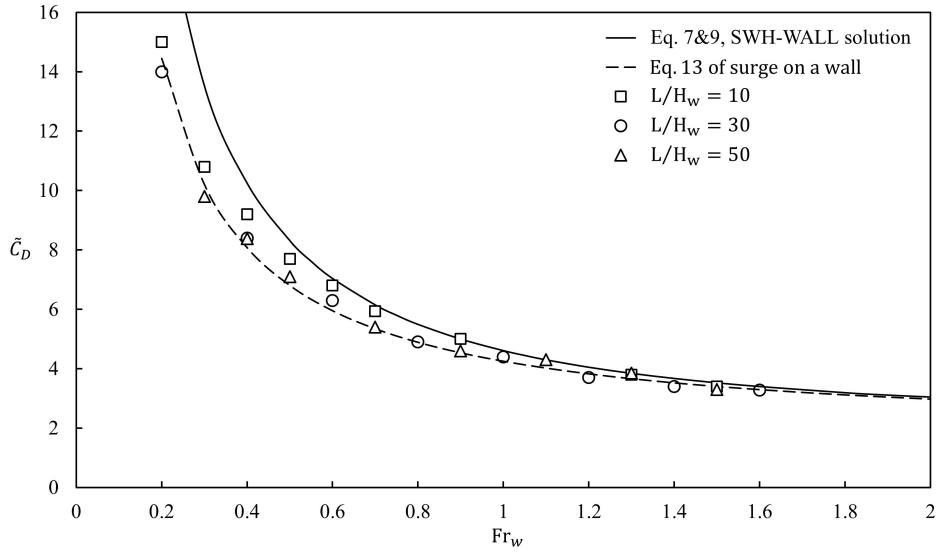

Figure 2–16: The wave-drag coefficients at equilibrium $\tilde{C}_D$ produced by the surges on dry land in channels, with $L/H_w = 10$, 30, and 50 denoted by the open square, open circle and open triangle, respectively. The dashed line is the Equation 2.13 that best fits the OpenFOAM simulation results. The solid line is equations 2.7 & 2.9 of the SWH-WALL solution for the wall coefficient $\overline{C}_D$.

The slightly higher values of $\tilde{C}_D$ obtained from simulation in the shorter channel length of $L/H_w = 10$ were not included in the correlation for Equation 2.13.

2.6.2 Dry-land Surges on a Structure of Finite Width

The interaction between the surges with the structure on dry land produced scattering waves around the structure that were distinctly different from the waves produced by the wet bores. In the former instance, the run-up of water rose rapidly on the front face of the structure. The wave-drag coefficient increased gradually. It did not reach its maximum until later, when the interaction between the wave radiation and the force on the structure had reached an equilibrium. Figure 2–17 shows the scattering waves obtained from the 3D OpenFOAM simulations for $\mathrm{Fr}_w = 0.6$, 1.0 and 1.6 and the width-to-depth

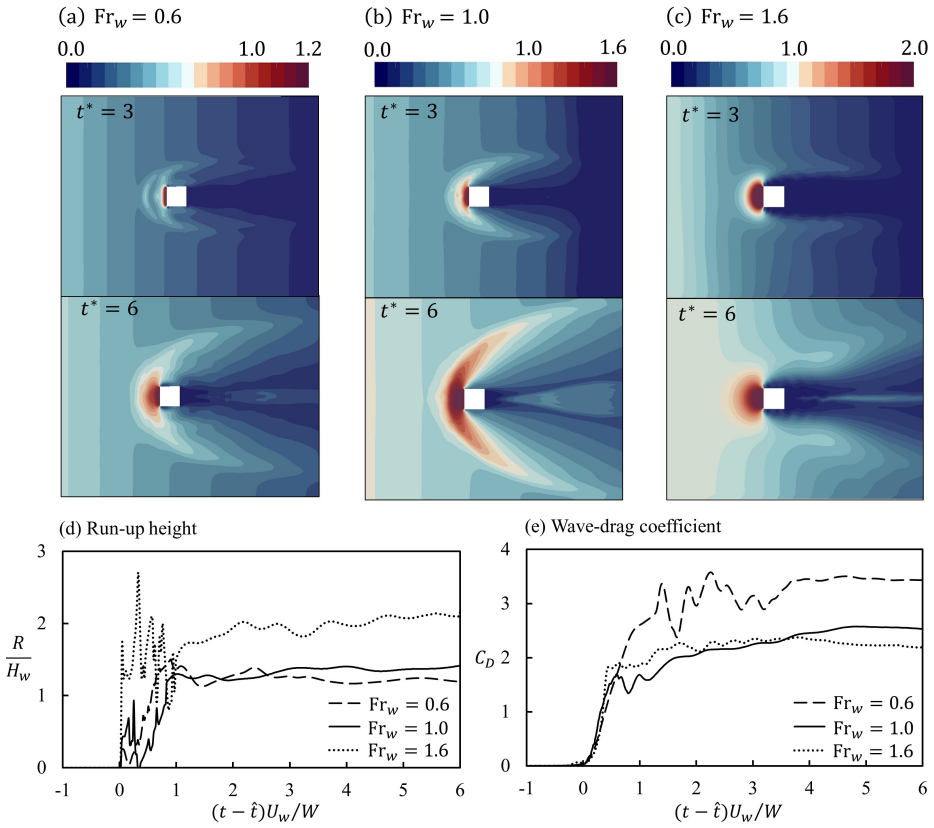

Figure 2–17: 3D OpenFOAM simulations of the impact of dry-bed surges on a square block. (a)(b)(c) Bottom-pressure $p/(\rho g H_w)$ contours on the x-y plane at time $t^* = (t - \hat{t})U_w/W = 3$ and at a later time $t^* = 6$, (d) wave run-up height R/H_w and (e) wave-drag coefficient C_D for wave Froude numbers $\mathrm{Fr}_w = 0.6$, 1.0 and 1.6 and width-to-depth ratio $W/H_w = 5$. The advancing front of the surges arrived at time $t = \hat{t}$; that is, at $t^* = 0$. The color bars above the bottom-pressure contours define the range of $p/(\rho g H_w)$.

$W/H_w = 5$ of the structure. The structure in the simulation is a square block of width W.

Water piled up on the front face of the block. The land in back of the block stayed dry throughout, from time $t* = (t - \hat{t})U_w/W = 0$ to 6, as the force on the structure increased toward the equilibrium. The time needed for the force of the dry-land surges on the block to attain its equilibrium was about 6 W/U_w. This may be compared with the time of 30 $\sqrt{H_w/g}$ taken for the force produced by the dry-land surge on a wall to reach its equilibrium.

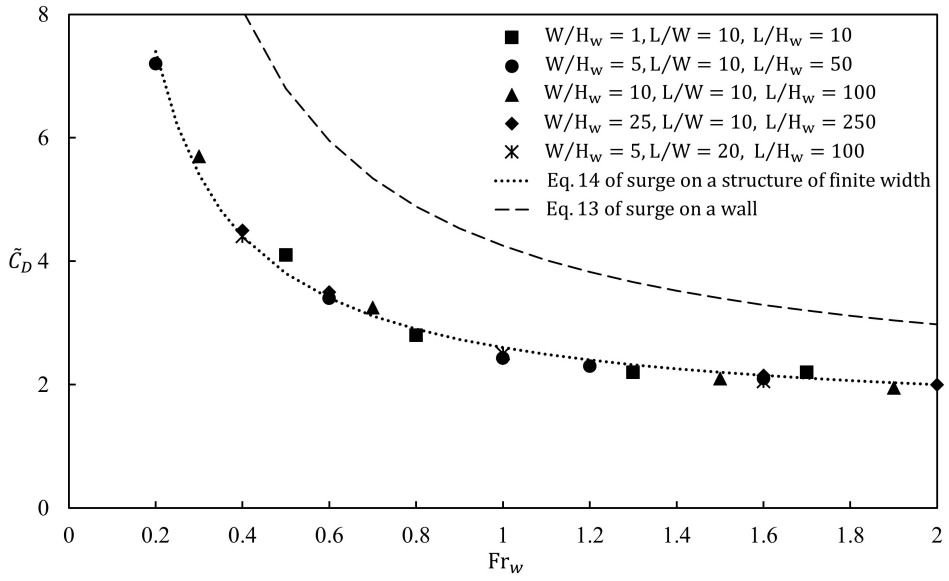

Figure 2–18: Wave drag coefficients on wave Froude number for the impact of surges on structures with finite width. Five types of structure width and distance L were considered, as denoted in the legend. The dotted line is Equation 2.14 that best fits the OpenFOAM simulation results for the surge impact on the structures. The dashed line is Equation 2.13 for the surge impact on a wall.

The pattern of the scattering waves depends on the Froude number. The wave-drag coefficient is also a function of the wave Froude number. The time scale of the increase is W/U_w which is directly proportional to the width of the structure. The 3D OpenFOAM simulations were conducted for small to large structures over a wide range of conditions, with the width-to-depth ratio varying from $W/H_w = 1$ to 25. Figure 2–18 shows the dependence of the equilibrium wave-drag coefficient $\tilde{C}_D$ on the wave Froude number Fr_w. All simulation data falls on the same curve. Remarkably, the coefficient $\tilde{C}_D$ was independent of W/H_w. The data obtained from all simulations are well described by the empirical formula:

$$\tilde{C_D} = 1.4 + \frac{1.2}{\mathrm{Fr_w}} \tag{2.14}$$

The block coefficient determined by this equation for the dry-land surge on a block is consistently lower than the wall coefficient by Equation 2.13 for the impact on a wall.

2.7 Summary and Conclusion

The wave impact force on a wall and a square structure were determined by numerical simulations using shallow-water-hydraulics (SWH) equations, and then by simulations using full Navier-Stokes equations conducted by open-source codes under the OpenFOAM platform.

The wave impact on a wall was considered first. A SWH-WALL solution was derived for the wall impact by the bores. This solution is shown in Figure 2–8 to be consistent with OpenFOAM simulations and available experimental data. OpenFOAM simulations were also conducted to find the impact of the dry-land surges. The wave-drag coefficient for the dry-land surge on a wall rose gradually toward an equilibrium. This equilibrium coefficient for the impact was related to the wave Froude number shown in Figure 2–8.

For the wave impacts on a structure of finite width, the 2D SWH-MinMod simulations and the 3D OpenFOAM simulations have determined the transient development of the wave impact in the range of surge-wave Froude numbers varying from $\mathrm{Fr}_w = 0.2$ to 2.0, and width-to-depth ratios varying from $W/H_w = 1$ to 25. For structures standing in water, the wave-drag coefficient rose to a peak $\hat{C}_D$ at the initial impact and then settled down to a relatively constant value $\tilde{C}_D$ at the wave-structure interaction equilibrium. Figure 2–12 provides the peak coefficients $\hat{C}_D$ and the equilibrium coefficient $\tilde{C}_D$ for the impact of bores on the structure. For a structure on dry land, the initial impact produced a rapid rise of water on the front face of the structure. The wave force on the structure was relatively insignificant in the initial impact

and the increase of the force toward the equilibrium was gradual. Figure 2–18 delineates the dependence of the equilibrium coefficient $\tilde{C}_D$ on wave Froude number Fr_w for a structure on dry land.

The equilibrium coefficients $\tilde{C}_D$ for the impacts of a structure standing in water and one on dry land were not dependent on the width of the structure. The time needed to attain the equilibrium were, however, proportional to the width of the structure. The size of the structure therefore is relevant, as the overall impact on the structure is the integration of the force over time.

For the design of coastal structures, FEMA guidelines (2008, 2012) recommend the use of a wave-force coefficient in the range of $\tilde{C}_D = 2 \sim 3$, and ASCE (2017) guideline recommends $\tilde{C}_D = 1.2 \sim 2.0$. This would be the range of the coefficient if the peak coefficient associated with the initial impact were ignored. But we cannot ignore the peak coefficient because it decides the initial breakaways of walls and windows, and the subsequent development of buoyancy forces and pore pressures in the foundations of buildings considered by Yeh et al. (2013, 2014) as at risk for sliding and overturning.

The simulations in this investigation were conducted to examine the impact of waves on a wall and a square structure. The full simulations to include the shoaling on variable topography and the impact on multiple structures of various arrangements would require significantly greater computer resources. These investigations could be carried out 3D OpenFOAM simulation but would be more efficient using the 2D SWH-MinMod simulation. The 2D simulation would be acceptable if the sizes of the structures were large compared with the depth of the coastal waters.

Chapter 3
Tsunami Wave Force on Elevated Coastal Structures

Xie, Peiwei, and Vincent H. Chu. Tsunami Wave Force on Elevated Coastal Structures. *Coastal Engineering* (2020) draft for submission.

Preface

The accelerating rise of sea level has increased the exposure of coastal communities in low-lying area to extreme inundation. Coastal structures need to be designed and redesigned for stability to withstand the wave impact by tsunami. Here we study the drag, lift and overturning stability on elevated coastal structures by numerical simulations using a well-calibrated solver. We calculated the transient variations of wave forces and the resulting overturning moments for their dependence on the elevation of the structures and the wave Froude number. Remarkably, with proper normalization, the wave-force coefficients are relatively independent of the structure's elevation.

3.1 Introduction

Global warming and sea-level rise have increased the exposure of coastal communities to extreme inundation (Parry et al. 2007; FitzGerald et al. 2008; Werner et al 2009; Nicholls & Cazenava 2010). A moderate sea-level rise may significantly increase the tsunami hazard in low-lying coastal area (Dall'Osso et al. 2014; Li et al. 2018). Indeed, Rignot et al. (2011), Nerem et al. (2018), VIMS (2019) have shown that the rising of sea-level is accelerating. Vertical

evacuation structure is an option to mitigating the tsunami risk (FEMA P-646; ASCE/SEI 7-16). The proper design of such structure for stability to withstand the wave forces produced by the tsunami is needed.

Post-event field surveys by Liu et al. (2005) for the 2004 Indian Ocean Tsunami and by Suppasri et al. (2012), Suppasri et al. (2013), Yeh et al. (2013), De Risi et al. (2017) for the 2011 Tohoku Tsunami have shown that structures previously designed to sustain tsunami impact were heavily damaged or even destroyed. Many of designated vertical evacuation buildings were found not tall enough for the wave height encountered during the tsunami, and hence resulted in fatality of the refugees (FEMA P-646). Research work has been carried out to seek a better understanding of the wave-structure interaction mechanism in order to achieve a better design. Previous work were conducted by considering either a vertical wall (Ramsden 1996; Linton et al. 2012; Robertson 2013;) or a standing cylinder with finite width (Asakura et al. 2003; Arnason et al. 2009; Fujima et al. 2010; Nouri et al. 2010; Wuthrich et al. 2018 a). Based on the research results, FEMA P-646 suggested the use of drag coefficient $C_D = 2.0$ for predicting the tsunami impact force on an coastal structure, and a larger value of $C_D = 3.0$ for structural wall elements of significant width. However, as denoted by Yeh (2014), the drag coefficient should have a dependence on the Froude number of the wave. Xie & Chu (2019) used an OpenFOAM solver to study the tsunami wave impact on both the vertical wall and the finite-width structure. Their simulations offer decent comparisons with the experimental data by Arnason et al. (2009) and Robertson et al. (2013) and also predict the correct dependence of the drag coefficient on the wave Froude number.

In the 2004 Indian Ocean Tsunami event and the 2011 Tohoku Tsunami event, buildings with open nature of the first floor or breakaway ground-level

components (wall, windows, doors) were found with more sustainability than others (Dalrymple & Kriebel 2005; Yeh et al. 2013). Indeed, fields surveys also shown that structures with elevation above ground were much more invulnerable in coastal flooding events (Kennedy et al. 2011; Tomiczek et al. 2014). Elevated coastal structure could be an option of vertical evacuation structure Thus far, only few research attention has been paid on tsunami wave hitting an elevated structure (Park et al. 2017; Park et al. 2019). Comprehensive understanding of the mechanism is not yet achieved.

To address this knowledge gap, we focus in this paper on studying the impact of tsunami wave on elevated coastal structures. We chose the interFoam solver, the same solver that was well-calibrated by Xie & Chu (2019), to conduct three-dimensional simulations for the study. Mesh refinement study was carried out to guarantee the accuracy of numerical solution. As the most significant parameter, the relative base elevation is varied, from 0 to 0.8 times of the wave height, to investigate its effect on the drag, lift and overturning moment on the structure. Beside that, the dependence of the wave forces and moments on the structure width and the wave Froude number are explored in an systematic approach. For the purpose of design and maintenance, in the end we offer the wave-force coefficients for predicting the drag and lift force, as well as the drag and lift moment, on an elevated structure under different wave Froude numbers.

This paper has 5 sections including this introduction. Section 2 presents the numerical methods used for the study. Section 3 discusses on the wave characteristics and the pressure contours on the elevated structures. Generalized force coefficients, transient force calculations and mesh refinement study are introduced in Section 4 and 5. The tsunami wave impact on an elevated structure and the influence of the structure's elevation and width are discussed

in Section 6. Section 7 extends the discussion onto the influence of the wave Froude number. Summary and conclusion are offered in Section 8.

3.2 Numerical Simulation using interFoam

The numerical simulation for the tsunami impact on the elevated structure was carried out using one of the open-source solvers known as interFoam in a C++ library managed by OpenFOAM Fundation (Weller et al. 1998; Greenfields & Christopher 2017). The interFoam solver is a two-phase immiscible fluids solver with volume-of-fluid interface capture technique (Deshpande et al. 2012). Higuera et al. (2014a,b) and Seiffert et al. (2014) used the interFoam solver to study the gravity wave interacting with coastal structures. Xie and Chu (2019) modified and calibrated the solver in a series of simulations of the tsunami wave impact on structures that are standing on solid ground. The interFoam solver used by Xie and Chu (2019) has produced correct results in close agreement with an analytical solution and the experimental observations.

The schematic in Figure 4–1 shows the advance of the tsunami toward the elevated structure. The elevation of the bottom slab of the structure is E above the ground. The width of the structure is W. The tsunami waves entered the computation domain with a wave height H_w and a wave velocity U_w. The structure is located at a distance $L = 30H_w$ from the entrance of the wave. As demonstrated by Xie and Chu (2019), the wave height H_w and the wave velocity U_w must be selected to satisfy the following compatability condition so that the tsunami wave would advance on the water of depth H maintaining its steep front before its impact on the structure:

$$\mathrm{Fr}_w^2 = \frac{U_w^2}{gH_w} = \frac{1}{2}(\frac{H_w}{H} + 1)(\frac{H_w}{H} - 1)^2(\frac{H_w}{H})^{-2} \tag{3.1}$$

The wave Froude number $\mathrm{Fr}_w = U_w/\sqrt{gH_w}$ is a unique function of the relative wave height H_w/H according to this condition.

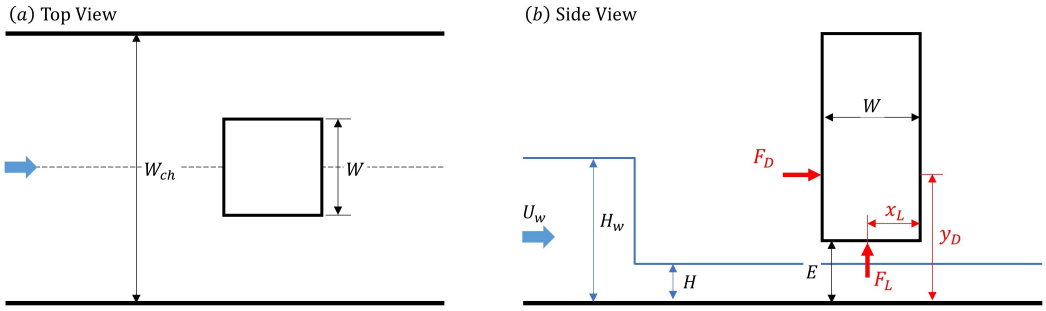

Figure 3–1: The elevated structure of width W and elevation E, and the incoming tsunami of wave height H_w and wave velocity of U_w; (a) top view and (b) side view.

The simulation determined the pressure on the front face and the bottom slab of the structure. The wave drag force F_D and its moment arms y_D are the results of pressure integration on the front face of the structure. The lift force F_L and moment arm x_L are the results of the pressure on the bottom slab. Elevating the structure above the ground may reduce the impact on the front face of the structure but the lift force on the bottom slab can increase the structure's instability to rotate, that may lead to overturning of the elevated structure.

Yeh el al. (2014) in their review and analysis of the structures struck by the 2011 Japan's Tohoku Tsunami has shown how the tsunami can cause reinforce concrete buildings to overturn. They identified the uplifting buoyant force to be the major cause of the structure failure. The laboratory study by Arnason et al. (2009) has shown further the dependence of these impact forces on the wave Froude number. Xie and Chu (2019) has provided formula from their analytical study and numerical simulation study for the impact on the structures that are standing on solid ground. The present study is to evaluate

the impact forces, and the moments of these forces, for their dependence not only on the wave Froude number but also on the elevation of the structure.

3.3 Pressure Contours and Air-Water Interface

Figure 3–2 presents the numerical simulation results using the interFoam solver. The solver finds the solution of the Navier-Stokes equations and turbulence model equations. The Re-Normalized Group (RNG) theory of Yakhot and Orszag (1986) defines the the k-ϵ turbulence model. The solver uses second-order spatial finite-volume discretization schemes. The PIMPLE iterative algorithm, as a combination of the pressure-implicit split operator (PISO) and the semi-implicit method for pressure-linked equations (SIMPLE) algorithms, are used for coupling equations of pressure and velocity. The number of corrector is chose as two as suggested in OpenFOAM (Greenfields & Christopher 2017). A classic implicit Euler method is used for time integration, together with the dynamic adjustable time stepping technique to guarantee a local Courant number of less than 0.8. No-slip boundary condition is patched to the wall to allow a zero velocity on the surface.

Figures 3–2 (a) to (d) are the wave pressure contours and the air-water interface for elevation of the bottom slab $E/H_w = 0$, 0.2, 0.5 and 0.8, respectively, obtained at the instance when the drag force on the front face F_D is maximum. Figures 3–2 (e) to (f) on the other hand are obtained at the instance when the lift force F_L is maximum. The incoming tsunami wave is specified with a wave Froude number of $\mathrm{Fr}_w = 1.0$ and a wave height of $H_w = 3$ m. The structure has a fixed width of 15 m ($W/H_w = 5$). The white line in each frame is the air-water interface defined by the volume fraction of $\alpha = 0.5$. The surface tension in the momentum equation is modeled as continuum surface force and calculated based on the volume fraction (Brackbill et al. 1992).

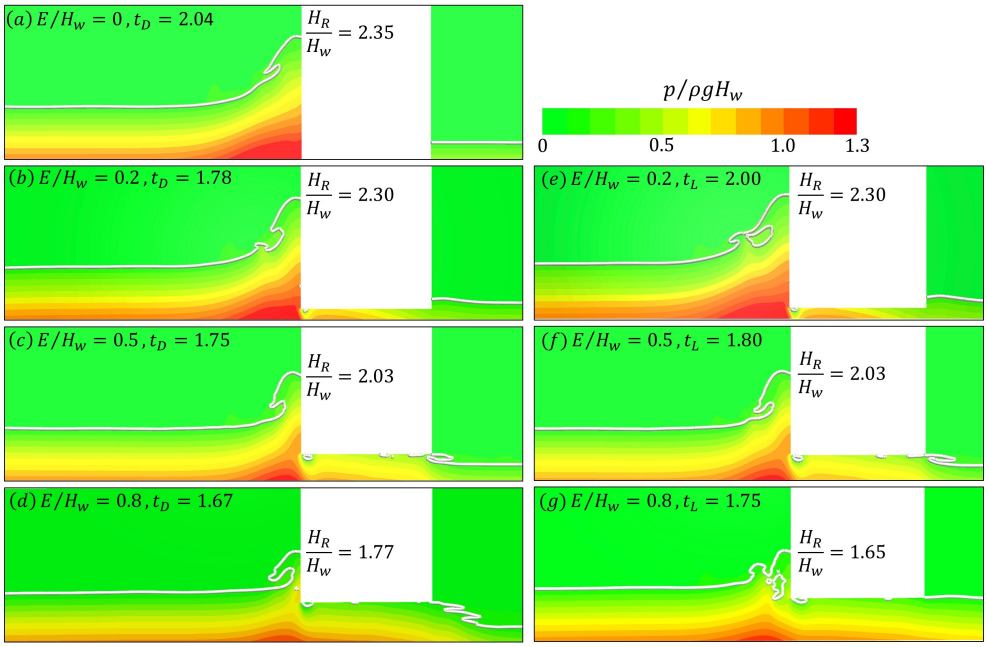

Figure	Elevation of the Bottom Slab	(1) Wave Run-up Height	(2) Hydraulic Pressure at the toe of front face by Run-up Height	(3) Hydraulic Pressure at the toe of front face by Wave Height	(4) Pressure at the toe of front face by interFoam solver	(5) Maiximum Pressure at the bottom slab by interFoam solver
	E/H_w	H_R/H_w	$\rho g(H_R - E)/\rho g H_w$	$\rho g(H_w - E)/\rho g H_w$	$p/\rho g H_w$	$p/\rho g H_w$
(a) t_D=2.35	0	2.35	2.35	1.0	1.30	
(b) t_D=2.30	0.2	2.30	2.10	0.8	1.15	
(c) t_D=2.03	0.5	2.03	1.53	0.5	0.80	
(d) t_D=1.77	0.8	1.77	0.97	0.2	0.75	
(e) t_L=2.00	0.2	2.30	2.10	0.8		0.70
(f) t_L=2.03	0.5	2.03	1.53	0.5		0.40
(g) t_L=1.65	0.8	1.65	0.85	0.2		0.15

Figure 3–2: Wave pressure contours $p/\rho g H_w$ on the center plane for the elevated structures of $E/H_w = 0$, 0.2, 0.5 and 0.8 at the instants of maximum drag force (a - d) and the instants of maximum lift force(e - f). Table 1 lists the hydrostatic and dynamic pressure pressure at the toe (a-d) and on the slab (e-f) of the structure.

The pressures on the front face and on the bottom slab are not hydrostatic. The *Guidelines for Design of Structures and Vertical Evacuation from Tsunami* (FEMA 2012, 2019), however, suggested to use the wave-height H_w to estimate the uplift force on the elevated structure. Table 1 (e), (f) and (g) show the comparison between the maximum dynamic pressure on the slab in column (4) and the hydrostatic pressure in (2) and (3). The dynamic pressure on the bottom slab is not uniform. The maximum value is slightly lower than the hydrostatic pressure by wave height. The resultant lift force is expected to be lower than the buoyant force of wave-height H_w. Table 1 (a) to (d) show the comparison between the dynamic pressure at the toe of the structure and the hydrostatic pressure. The dynamic pressure at the toe of the structure is smaller to the hydrostatic pressure of run-up height but higher than the hydrostatic pressure of wave height. Assuming hydrostatic, the use of wave height or run-up up would lead to misestimation of the drag force on the front face.

3.4 Generalized Coefficients and the Transient Variations

We define the dimensionless coefficient based on the"relative" wave height, which is the height of the incoming wave relative to the elevation of the structure, that is

$$H_{wr} = H_w - E \tag{3.2}$$

With this length scale, the generalize wave-drag coefficient and generalized wave-lift coefficient become

$$C_D = \frac{F_D}{\frac{1}{2}\rho U_w^2 A_{frontal}} \tag{3.3}$$

$$C_L = \frac{F_L}{\rho g H_{wr} A_{slab}} \tag{3.4}$$

The frontal projected area is $A_{frontal} = H_{wr}W$ and the area of the bottom slab is $A_{slab} = W^2$ for the rectangular structure of width W and length W. The normalization for the wave-drag coefficient is the dynamic pressure $\frac{1}{2}\rho U_w^2$. The normalization for the wave-lift coefficient, however, is the buoyant pressure $\rho g H_{wr}$ that is proportional to the relative wave height H_{wr}. The generalized wave-drag coefficient reduces to the one used by Xie and Chu (2019) for structure standing on solid ground, that is when $E = 0$. The generalized wave-lift coefficient is similar in form to the coefficient proposed by Yeh et al. (2014) and the one recommended in the Guidelines for Design of Structures and Vertical Evacuation from Tsunami (FEMA 2012, 2019).

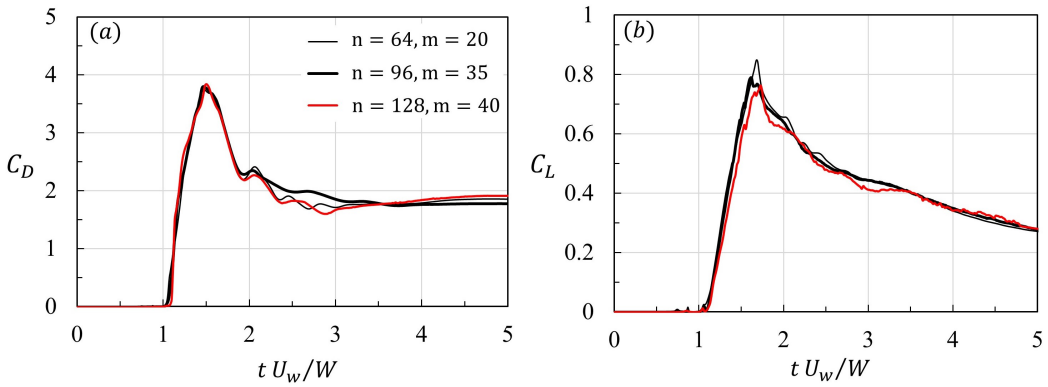

(c)

n	m	$\hat{C}_D$	FE%	Order	$\hat{C}_L$	FE%	Order
64	20	3.73750	3.30		0.84845	12.34	
96	30	3.79793	1.73	3.326	0.78919	4.49	5.385
128	40	3.83921	0.66		0.76245	0.96	
∞	∞	**3.86496**	0		**0.75523**	0	

Figure 3–3: Mesh refinement study for a case with three sets of mesh size. The wave has $\mathrm{Fr}_w = 1.0$, $H_w = 3.2$ m and $U_w = 5.6$ m/s. The structure has $E = 1.5$ m and $W = 32$ m. The horizontal mesh size is defined as $n = W/\Delta x = W/\Delta y$. The vertical mesh size is $m = E/\Delta z$.

Transient variations of the drag coefficient and lift coefficients for one case are plotted in Figure (a) and (b), respectively. The incoming wave has $\mathrm{Fr}_w = 1.0$, $H_w = 3.2$ m and $U_w = 5.6$ m/s. The elevated structure has a elevation of $E = 1.5$ m and a size of $W = 32$ m ($W/H_w = 10$). The drag coefficient run up

to a peak value before its falling onto a quasi-steady state. The lift coefficient climbs up to a peak and then declines slowly. The simulations are run with three different sets of mesh size. The peak values of the drag and lift coefficient obtained from the three simulations are used for the mesh refinement study, as discussed in the next section.

3.5 Mesh Refinement and Convergence Study

To determine the solution accuracy, mesh refinement and convergence study is performed for a case with three sets of mesh sizes, as shown in Figure 3.4. The maximum values of C_D and C_L are used for the determination of convergence and accuracy. The table in Figure 3.4 summarizes the simulation results obtained from the progressively smaller mesh sizes. The order of convergence as the mesh is refined is determined from extrapolation formulae given in Stern et al. (2001). For each group of solutions $(\hat{\alpha}_1, \hat{\alpha}_2, \hat{\alpha}_3)$ obtained from three mesh sizes from finest to coarsest, the formula for the order of convergence is

$$P = \frac{1}{\ln r_{21}} \ln [\frac{\hat{\alpha}_3 - \hat{\alpha}_2}{\hat{\alpha}_2 - \hat{\alpha}_1}] + \frac{1}{\ln r_{21}} [\ln(r_{32}^P - 1) - \ln(r_{21}^P - 1)] \tag{3.5}$$

where the mesh size ratios $r_{21} = \Delta_2/\Delta_1 = 1.33$ and $r_{32} = \Delta_3/\Delta_2 = 1.50$. The extrapolated value is

$$\hat{\alpha}_{\Delta \to 0} = \frac{r_{21}^P \hat{\alpha}_1 - \hat{\alpha}_2}{r_{21}^P - 1}. \tag{3.6}$$

The boldface numbers in the table are the values obtained from the extrapolation to $\Delta \to 0$. The computational Fractional Error in percentage is

$$\text{FE}(\%) = \frac{|\hat{\alpha} - \hat{\alpha}_{\Delta x \to 0}|}{\hat{\alpha}_{\Delta x \to 0}} \times 100 \tag{3.7}$$

The convergence study shows that with the mesh numbers of $n = 128$ and $m = 20$, the computational errors of drag coefficient and lift coefficient are 0.66% and 0.96%, respectively, which is adaptable for engineering purpose.

This set of mesh size is used for the following simulations. The averaged CPU-hour for one simulation is 180 hours for a station with 7^{th} generation Intel(R) Core-i5.

3.6 Wave Impact on Elevated Structures of Various Widths and Elevations

3.6.1 Wave on the elevated structures of $E/H_w = 0$ to 0.8

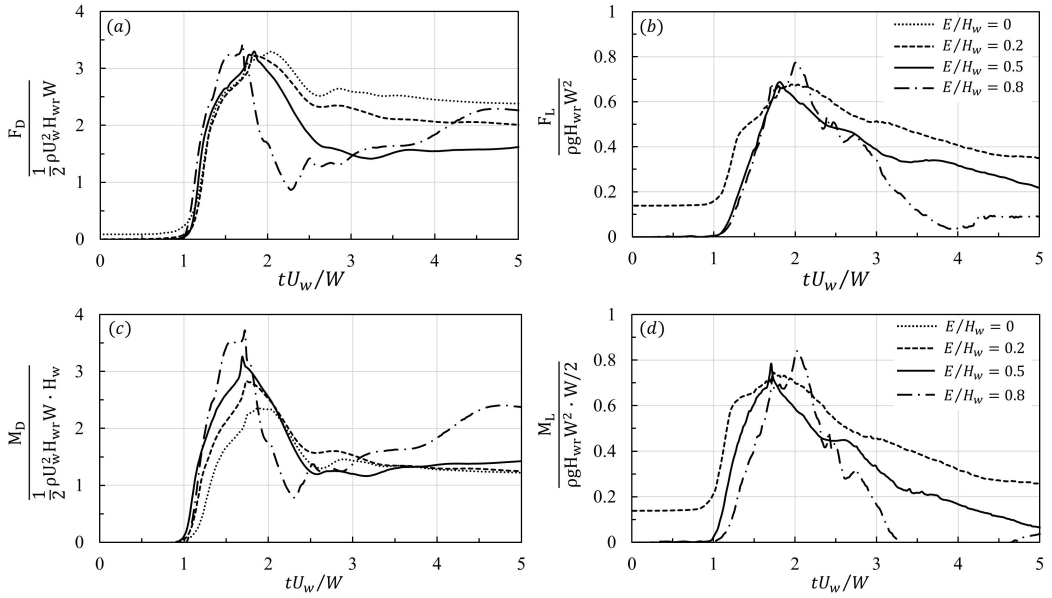

Figure 3–4: Transient variations of the (a) drag coefficients, (b) lift coefficients, (c) dimensionless drag moment and (d) dimensionless lift moment for structures with elevations of $E/H_w = 0, 0.2, 0.5$ and 0.8. The tsunami wave had $H_w = 3$ m and $\mathrm{Fr}_w = 1.0$. The structure size was fixed at $W/H_w = 5$.

The wave forces and the overturning moments that contribute to the potential failure of the structures are determined from the simulations. In Figure 3–4, the transient variations of the dimensionless (a) drag force, (b) lift force, (c) drag moment and (d) lift moment are plotted for the relative elevations of $E/H_w = 0$, 0.2, 0.5 and 0.8. The wave forces and overturning moments go through an impulsive stage at the initial impact and then fall down. For each case, the occurrence of maximum drag force is accompanied with the occurrence of maximum drag moment; the lift force and lift moment

do so. Using the relative wave height for normalization, the peaks of the drag coefficients for different elevations are almost identical. This occurs also for the lift coefficients. Accordingly, the maximum drag force and lift force are reducing as the elevation of the structure is risen up.

The values of the peak drag coefficients and peak lift coefficients for the relative elevations from $E/H_w = 0$ to 0.8 are plotted in Figures 3–5 (a) and (b), respectively. The maximum drag and lift coefficients are relatively independent of the elevation of the bottom slab. Another set of simulations with a much more significant wave height of $H_w = 18$ m were conducted. The consistency of the results indicate that independence of the coefficients on the elevation is valid under different wave conditions. As the lift force is normalized by the hydrostatic buoyant force $\rho g(H_w - E)A_{slab}$, the averaged coefficient of 0.7 indicates that the uplift force on the structure is smaller than the hydrostatic buoyant force, which is due to the dynamic characteristic. This result can also be inferred from the dynamic pressure distribution on the slab, as shown in Figure 3–2.

The drag-moment arm y_D is determined by dividing the maximum drag moment with the maximum drag force, as they occurred at the same time. The drag-moment arms of different elevations are normalized by the wave height H_w and plotted into Figure 3–5 (c). y_D/H_w increases slightly as E/H_w is increasing and get stable around the value of 1.0, indicating that the force center on the structure is closed to the height of the wave. Knowing the drag force, one can conservatively use the wave height as moment arm to estimate the moment of the drag force on the structure. The lift-moment arm x_L, on the other hand, is determined by dividing the maximum lift moment with the maximum lift force. Normalized by half of the structure size $W/2$, the lift-moment arms are plotted in Figure 3–5 (d). $x_L/(W/2)$ is relatively

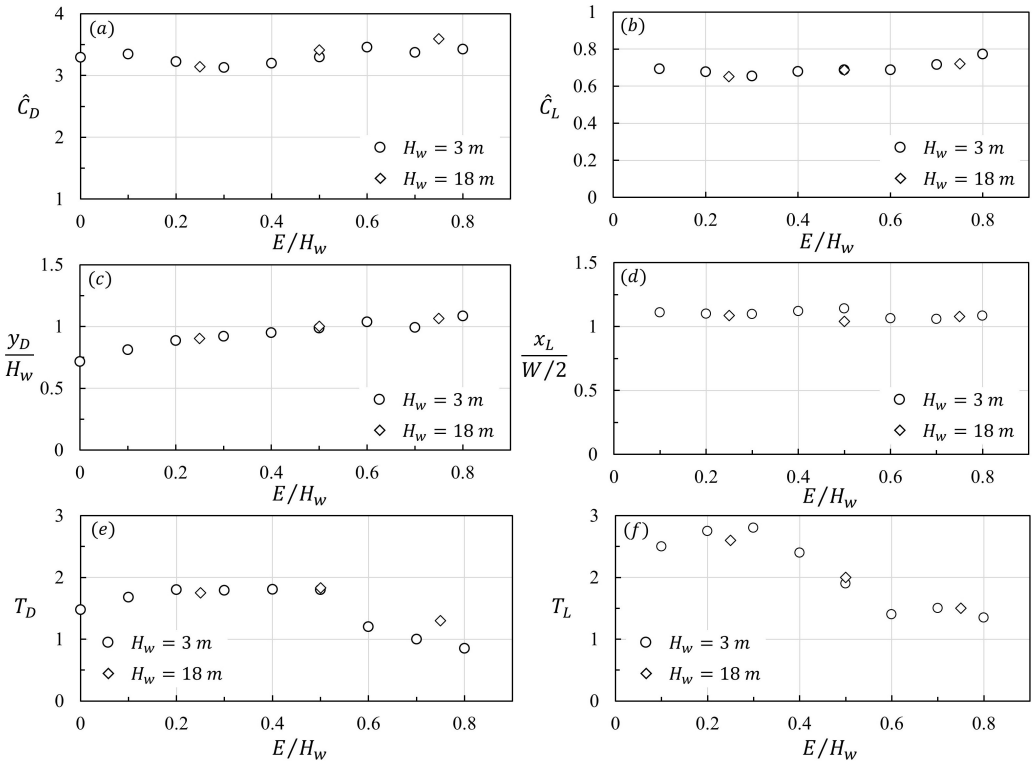

Figure 3–5: The (a) maximum drag coefficient, (b) maximum lift coefficient, (c) drag-moment arm, (d) lift-moment arm, (e) impulse period of drag force and (f) impulse period of lift force for a tsunami wave of $\mathrm{Fr}_w = 1.0$ impacts on elevated structures of $E/H_w = 0$ to 0.8.

independent of the relative elevation and has an averaged value of 1.1. The lift force center is located at the center of the slab with a slight shift to upstream.

Besides the peak force, the force impulse, which is the force times its impact period, is another significant concern of potential damage. The impulse period of the drag force T_D is defined as the period of the impulsive stage before the force falls down onto a quasi-steady state. The impulse period of the lift force T_L is defined as the period that the force exceeds half of the peak force, since the lift force did not have a observable quasi-steady state, as shown in Figure 3–4 (b). The impulse period of the drag and lift are plotted in 3–5 (e) and (f), respectively. As the elevation is increasing, the impulse period shows an downward trend, and the reduction is up to 50%. This result denotes that

rising the elevation of the structure can not only reduce the drag and lift force but also reduce their impulse periods, and hence reduce the force impulses.

3.6.2 Wave on the elevated structures of $W/H_w = 5$ to 30

The wave hitting a finite-width structure relieves itself by flowing around the sides. For structure with a significant width, a transient amount of water may accumulate against the forward side of the structure and results in an significant peak force (FEMA 2012, 2019). Xie & Chu (2019) has offered an investigation to determine the wave force as a function of the structure size for coastal structures standing on solid ground. In this section, the effect of the structure size on the wave force for an elevated structure is investigated by simulations with varies structure widths of $W/H_w = 2$ to 30. In the simulations, the tsunami wave had a wave Froude number of 1.0 and a wave height of $H_w = 3.0$ m. The relative elevation was fixed at $E/H_w = 0.5$.

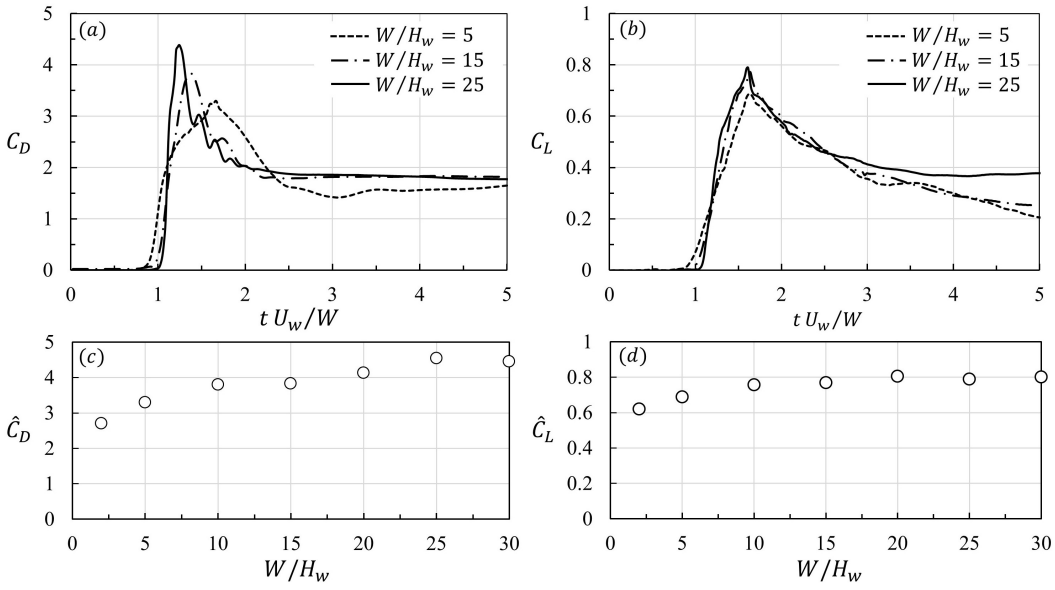

Figure 3–6: Transient variations of the (a) drag coefficients and (b) lift coefficients for structures of $W/H_w = 5, 15$ and 25. The incoming wave have and $\mathrm{Fr}_w = 1.0$. The maximum drag and lift coefficient for structure widths from $W/H_w = 2$ to 30 are plotted in (c) and (d), respectively.

The transient variations of the drag and lift coefficients for the width of $W/H_w = 5$, 15 and 25 are plotted in Figure 3–6 (a) and (b). The variation of structure size does not alter the transient variation pattern but the peak force. The maximum drag coefficient and lift coefficient for the width from $W/H_w = 2$ to 30 are plotted in (c) and (d), respectively. The maximum drag coefficient has a significant increase as the width varies from $W/H_w = 2$ to 10. This increase becomes mild when the structure size varies from 10 to 30. The maximum drag coefficient is increased by 60% when the structure size is extended from $W/H_w = 2$ to 30. The variation of the maximum lift coefficient with the structure size is gentle, as it varies from a value of 0.6 to 0.8 when the structure widths increase by 15 times ($W/H_w = 2$ to 30). The effect of the structure size would be further discussed in the next section for the waves of different Froude numbers.

3.7 Dependence of the Wave Impact on Wave Froude Number

As denoted by Yeh (2014), the drag coefficient of tsunami impact force on a coastal structure must be correlated to the gravity, i.e. the wave Froude number. The wave Froude number should be a significant parameter when considering the tsunami wave impact on a elevated structure. The last section has analyzed the wave impact on structures of various elevations and widths with a fixed wave Froude number of $\mathrm{Fr}_w = 1.0$. In this section, the effect of the wave Froude numbers on the wave impact would be investigated, starting with the wave Froude numbers of $\mathrm{Fr}_w = 0.5$ and 1.5.

3.7.1 The effects of elevations and widths under $\mathrm{Fr}_w = 0.5$ and 1.5

The pressure contours of the wave at the instants of maximum drag for the wave Froude number of $\mathrm{Fr}_w = 0.5$, 1.0 and 1.5 are plotted in Figures 3–7 (a), (b) and (c), respectively. The tsunami wave has a wave height of 3 m. The structure has a fixed elevation of 1.5 m and a fixed width of 15 m.

As the wave Froude number increases, the wave pressure and the wave run-up on the front face of the structure is significantly increased. At the Froude number of $\mathrm{Fr}_w = 0.5$, the pressure under the structure has a smooth transition with the upstream flow and is almost hydrostatic. At the Froude number of $\mathrm{Fr}_w = 1.5$, the pressure has a dramatic transition from the front face to the gap. The pressure under the structure is irregular and much lower than the hydrostatic pressure, which should be due to the high velocity and hence the severe dynamic impact.

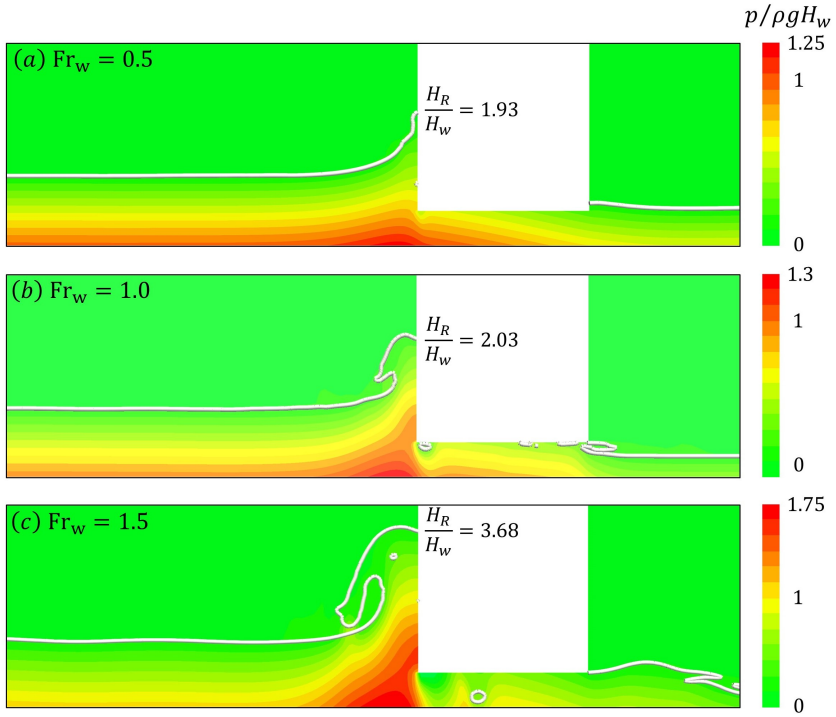

Figure 3–7: Pressure contours $p/\rho g H_w$ on the center plane of the elevated structure at the instants of maximum drag for the wave Froude number of (a) $\mathrm{Fr}_w = 0.5$, (b) $\mathrm{Fr}_w = 1.0$ and (c) $\mathrm{Fr}_w = 1.5$.

The transient variations of drag and lift coefficients of these three cases are plotted in Figures 3–9 (a) and (b), respectively. The maximum drag coefficient apparently has a strong dependence on the wave Froude number, as the peak value decreases from 6.02 to 2.73 for $\mathrm{Fr}_w = 0.5$ to 1.5. The lift coefficient of $\mathrm{Fr}_w = 0.5$ does not have an obvious impulsive stage, since the wave velocity

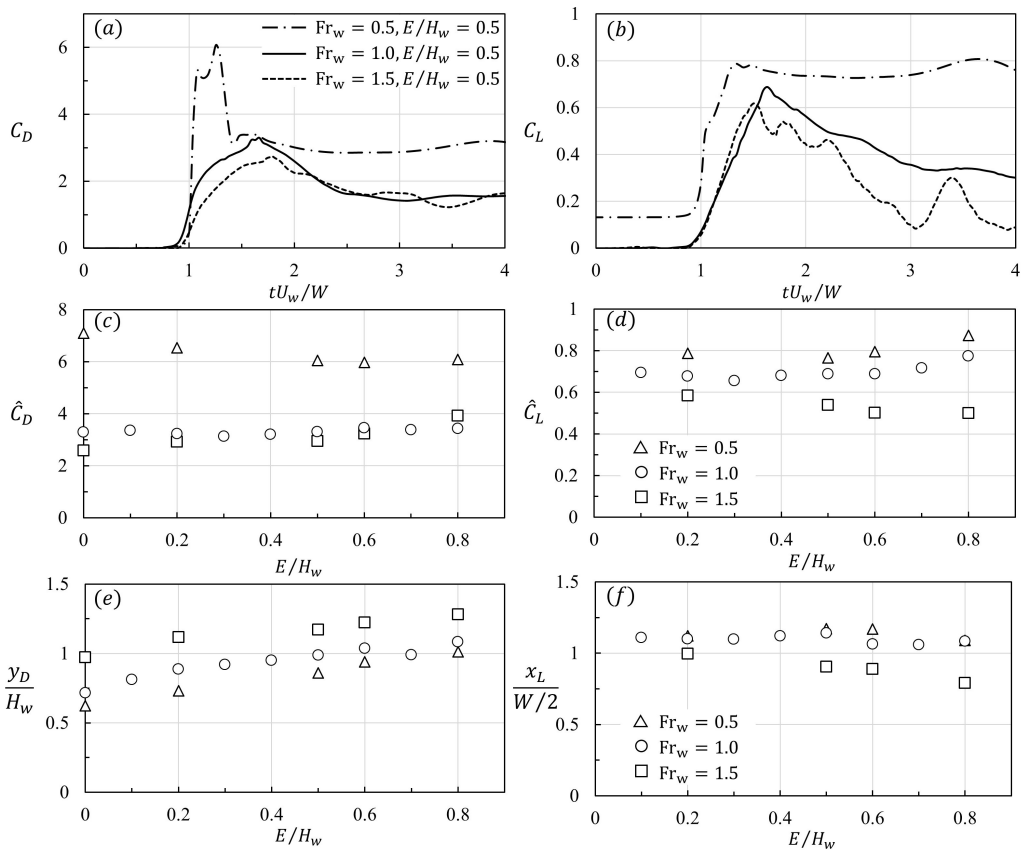

Figure 3–8: The peak (a) drag coefficients and (b) lift coefficients for structures of elevations $E/H_w = 0$ to 0.8. The triangular symbols denote the incoming wave of $\mathrm{Fr}_w = 0.5$; the square symbols denote the incoming wave of $\mathrm{Fr}_w = 1.5$. The structure size is $E/H_w = 5$.

is relatively mild and the pressure under the structure is almost hydrostatic. The maximum lift coefficient decreases from 0.80 to 0.61 when Fr_w increases from 0.5 to 1.5, due to growing dynamic impact.

Simulations with $E/H_w = 0$ to 0.8 were also conducted for the wave Froude numbers of $\mathrm{Fr}_w = 0.5$ and 1.5. The maximum drag coefficients and maximum lift coefficients are plotted in Figures (c) and (d), respectively, along with the cases of $\mathrm{Fr}_w = 1.0$. Same as the finding in the last section that, the elevation of the bottom slab has a weak influence on the maximum drag and lift coefficients. It can be inferred that for one wave Froude number, a specific drag coefficient and lift coefficient can be used for the prediction of wave force.

The moment arms for the drag force and lift force are plotted in (e) and (f), respectively. The dependence of the moment arms on the relative elevation is mild. The drag-moment arm has a slight uprise trend as the wave Froude number increases, denoting that the increasing run-up height on the front face shifts the drag-force center upward. The lift-moment arm of $\mathrm{Fr}_w = 1.5$ is slightly lower than the one of $\mathrm{Fr}_w = 0.5$ and 1.5, which means the lift-force center is moving downstream. That is mainly due to the existence of the low-pressure zone near the entrance of the gap, as shown in Figure 3–7 (c).

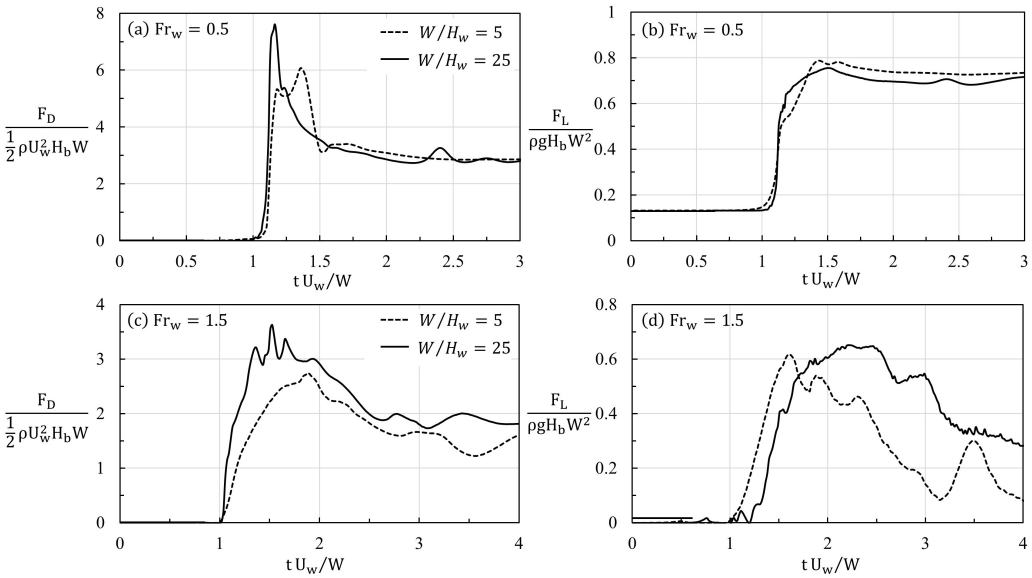

Figure 3–9: Transient variations of drag coefficient, lift coefficient on the elevated structure for the wave Froude numbers of $\mathrm{Fr}_w = 0.5$ and 1.5. The structure widths are $W/H_w = 5$ and 25. The relative base elevations are $E/H_w = 0.5$.

It is acceptable to use a moment arm equal to the wave height $y_D = H_w$ for estimating the drag moment on an elevated structure. A factor of 1.5 can be applied for waves with relatively high Froude numbers ($\mathrm{Fr}_w > 1$) for conservative consideration. A lift-moment arm of 1.2 times of half structure size $x_L = 1.2W/2$ can be applied for the estimation of lift moment under different wave conditions.

The effect of the structure size is examined for the wave Froude number of $\mathrm{Fr}_w = 0.5$ and 1.5. The structure sizes of $W/H_w = 5$ and 25 are considered. The transient variations of drag and lift are plotted in Figures 3–9 (a) and (b) for $\mathrm{Fr}_w = 0.5$, and in (c) and (d) for $\mathrm{Fr}_w = 1.5$. Similar to the previous result, the structure size has a notable influence on the drag coefficient, while its influence on the lift coefficient is negligible.

3.7.2 The drag and lift coefficients as a function of Fr_w

To fulfill the investigation of the wave Froude number effect, simulations of the wave Froude numbers from $\mathrm{Fr}_w = 0.4$ to 1.8 and the relative structure sizes of $W/H_w = 5$ and 25 are conducted. The maximum drag and lift coefficients are plotted in Figures 3–10 (a) and (b), respectively.

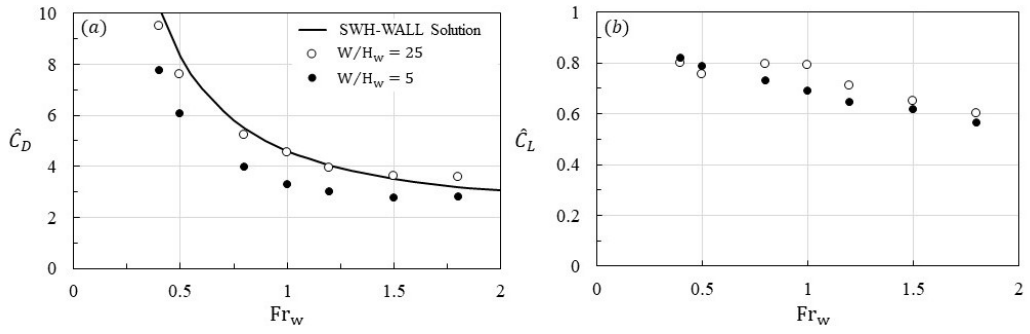

Figure 3–10: The variations of peak (a) drag coefficients and (b) lift coefficients with wave Froude number for structures of $W/H_w = 5$ (solid circle) and $W/H_w \geq 25$ (open circle). The dash line is the SWH-Wall solution of wave force on a vertical wall by Xie & Chu (2019).

As discussed above, the maximum drag coefficient $\hat{C}_D$ has a strong dependence on the wave Froude number. $\hat{C}_D$ falls down sharply at sub-critical Froude number $\mathrm{Fr}_w < 1$ and the goes flat when the Froude number keeps increasing. With $W/H_w = 25$, the values of $\hat{C}_D$ fall on the SWH-Wall solution. The SWH-Wall solution, plotted as the dot line in (a), is an analytical solution for tsunami wave impacts on an vertical wall (Xie & Chu 2019). A structure of size $W/H_w = 25$ is analogous to a wall. With the normalization of the

relative wave height $H_{wr} = H_w - E$, the dependence of the coefficients on the elevation is exempted. The SWH-Wall solution can be adapted for prediction of the drag force on an elevated structure in the limit that the structure has a significant width.

For the structure of $W/H_w = 5$, an averaged reduction of 20% occurs to the drag coefficient. The drag coefficient would go lower if the structure size is smaller. ASCE/SEI 7-16 requires that impulsive tsunami loading should be considered for structural elements of width greater than 3 times of flow depth. The concern of $W/H_w = 5$ could of practical significance.

The maximum lift coefficient $\hat{C}_L$ slightly decreases when the wave Froude number is increasing, mainly due to the growing hydrodynamic effect. The dependence of the lift coefficient on the structure size is negligible. The values of $\hat{C}_L$ are smaller than 1.0, meaning that the uplift force on the elevated structure is smaller than the hydrostatic buoyant force $\rho g H_{wr} A_{slab}$. The suggested value of 1.0 by FEMA (2012) for predicting the uplift force is of conservative consideration.

3.8 Summary and Conclusion

We conduced three-dimensional simulations to study the drag, lift and force moment produced by tsunami waves impact on elevated coastal structures. A well-calibrated solver under the OpenFOAM library is chosen. Mesh refinement study was carried out to ensure the solution accuracy.

Using the normalization of relative wave height $H_{wr} = H_w - E$, the maximum drag and lift coefficients are independent of the elevation of the structure. The simulations predict the correct dependence of the maximum drag coefficient on the wave Froude number and the structure size. The maximum uplift force on an elevated structure has a minimum reduction of 20% to the buoyant force, due to the hydrodynamic effect. The maximum lift coefficient slightly

decreases with the growing of the wave Froude number. The structure size has little impact on the maximum lift coefficient. The drag-moment arm and lift-moment arm on the elevated structure is relatively independent on the elevation. For conservative consideration, a drag-moment arm of 1.5 times of the wave height can be used to estimate the drag moment; the lift-moment arm can be taken as 1.2 times of half of the structure size.

This study provides the drag and lift coefficients as well as the moment arms for the predictions of drag, lift and overturning moment on an elevated structure. With proper normalization, the influence of elevation is exempted from the coefficients. Note that in specific situations, structures might have different shapes or with beans, columns and openings. Simulations using the interFoam solver for specific engineering purpose is recommended.

Chapter 4
Impact Forces by a Gravity Current on a Circular Cylinder above the Seabed

Xie, Peiwei, and Vincent H. Chu. Impact Forces by a Gravity Current on a Circular Cylinder above the Seabed. *Coastal Engineering* (2020) under review.

Preface

We conducted large-eddy simulation to determine the wave forces by a gravity current on a circular cylinder above the seabed, at a significantly higher Reynolds number than any previous study of the same problem. The simulations provided the wave deformation of the current and the transient development of the force for different elevations of the cylinder above the seabed. The force coefficients due to the waves were large (two-to-three times greater in magnitude) compared with the known coefficients for steady flow of uniform density. The lift coefficients in the directions toward and away from the seabed were comparable in magnitude to, and in some instances exceeded, the drag coefficient in the direction of the current. The mesh-refinement and model-performance studies conducted with the simulations have shown the twoLiquidMixingFoam solver to be highly reliable and accurate, as the solver has provided results in close agreement with laboratory observation.

4.1 Introduction

The sudden destabilization of submarine sediments during landslides caused by earthquakes can produce turbidity currents with great destructive forces. As much as 20 m/s of current velocity on the continental slope has been measured as a consequence of submarine landslides (Hsu et al. 2008; Hsu et al. 2009). Indeed, the force of turbidity currents was discovered by Heezen and Ewing (1952) in an investigation into the destruction of 12 submarine telegraph cables on the Grand Banks of Newfoundland that had been triggered by a magnitude-7.2 earthquake on the night of Nov. 18, 1929. Infrastructures dedicated to offshore exploration must meet very stringent safety targets because remediation relating to accidents in deep waters is so challenging. The impact of the turbidity current is one factor to be considered in the design of sub-sea structures on the continental slope. Since onsite measurement of impact forces on structures in deep water would be difficult, numerical simulations offer an excellent means of estimating the drag and lift forces under various scenarios.

The dynamics of turbidity currents have been the subject of numerous studies (Hacker et al. 1996; Hartel et al. 2000; Shin et al. 2004; Cantero et al. 2007; Ooi et al. 2007; Ooi et al. 2009; Longo et al.; 2018). However, relatively little attention has been paid to the impact force of the current, despite the fact that the impact force is needed in the design of sub-sea structures.

In this paper, we examine the impact force on a circular cylinder above the seabed. On impact of the gravity current on the cylinder, waves are produced in the current. Due to the waves, the magnitude of the wave force is greater than the impact force would be from a steady flow of uniform density. Ermanyuk & Gavrilov (2005a,b) measured the wave force of the gravity current in the laboratory, and have correlated the force with the reduced gravity of

the current. The success of their correlation, as the gravity is reduced by a factor of 4 from $\Delta\rho/\rho = 0.04$ to 0.01, supports the notion that the force is due to the waves.

The laboratory measurement of the wave force by Ermanyuk & Gavrilov (2005a,b) and the subsequent numerical simulations of the force by Gonzalez-Juez et al. (2009a,b) and Gonzalez-Juez et al. (2010) are significant contributions to this issue. Nevertheless, further study of the wave force beyond the laboratory scale was needed, particularly in the case of the impact of the force on a circular cylinder. The separation of the flow from the boundary layer on the surface of the circular cylinder is known to be dependent on the Reynolds number and the mesh size used in the numerical simulation (Bouharie & Chu, 2007; Norberg, 2001).

We conducted numerical simulations to determine the impact force for two Reynolds numbers – $Re_D = 840$ and $Re_D = 23500$ – using progressively refined meshes to achieve convergence of the numerical solution. The goal of the simulations involving $Re_D = 840$ was to reproduce the laboratory experiment for the selection of the best sub-grid-scale (SGS) turbulence model among five models tested for their performance. The mesh size was further refined to achieve convergence of the numerical solution at the higher Reynolds number of $Re_D = 23500$. The mesh refinement study for the two flows of very different Reynolds numbers not only assured the accuracy of the simulations but also provided the guide needed for the design of sub-sea structures at still higher Reynolds numbers.

This paper has five sections, including this Introduction. In Section 2, we discuss how we validated the selected SGS turbulence model as the benchmark, using the laboratory data obtained by Ermanyuk & Gavrilov (2005b)

at the Reynolds number of $Re_D = 840$. In Section 3, we explain the computation and mesh refinement study for the transient development of the force on the cylinder and the wave deformation on the gravity current for three elevations of the cylinder above the seabed at the higher Reynolds number of $Re_D = 23500$. Section 4 includes (i) a parametric study of the elevation effect of the cylinder above the seabed, (ii) a comparison of the results with the previous works at the lower Reynolds numbers, and (iii) a contrast between the impact by the gravity current and those of the force of a steady uniform flow. The last and final section is the summary and conclusion.

4.2 Selection and Validation of the SGS Turbulence Model

Our simulations of the gravity current and the impact force on the circular cylinder relied on an open-source computational fluid dynamic solver known as twoLiquidMixingFoam. The solver and a number of pre-/post- processing utilities are part of a C++ toolbox maintained in a library that is customized and distributed by the OpenFOAM Foundation (Weller et al. 1998; OpenFOAM 2017). Successful implementations of the OpenFOAM solvers for studying coastal and river engineering processes include the works by Higuera et al. (2013, 2014a, 2014b), Nguyen (2015) and Xie & Chu (2019). The twoLiquidMixingFoam solver in particular has been used by Gruber et al. (2011), Zhang et al. (2016) and Krpan et al. (2018) for related fluid dynamic simulations. For large-eddy simulations of turbulence flow, the twoLiquidMixingFoam solver offers a number of options for sub-grid-scale (SGS) modeling.

The laboratory experiment by Ermanyuk & Gavrilov (2005b) provided the only available experimental data for calibration. The first series of simulations was intended to reproduce as closely as possible the conditions of the laboratory experiment. Figure 4–1 is a schematic diagram that shows the

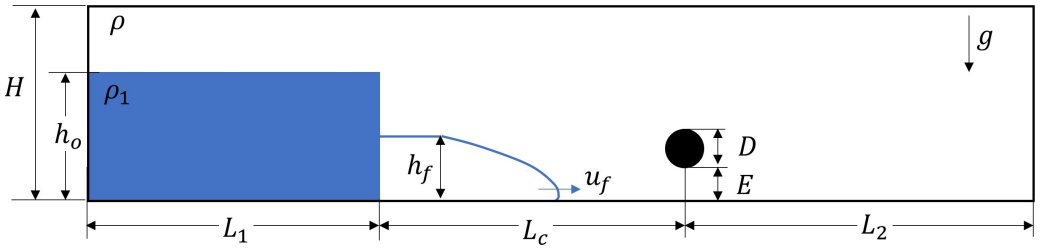

Figure 4–1: Schematic diagram of the laboratory experiment by Ermanyuk & Gavrilov (2005b).

gravity current in the laboratory produced by the sudden release of a block of aqueous sugar solution of density $\rho_1 = \rho + \Delta\rho$. The initial height and length of the block were $h_o = 8$ cm and $L_1 = 160$ cm. The tank height, length and width were $H = 10$ cm, $L = L_1 + L_2 + L_c = 320$ cm, and $W = 20$ cm. The circular cylinder had a diameter of $D = 1.5$ cm located at a distance of $L_c = 5h_o$ downstream from the block, with an elevation of $E = 0.45$ cm above the tank bottom.

We selected the dynamic k-equation SGS turbulence model (Yoshizama 1982, Yoshizama & Horiuti 1985) for the simulation of the gravity current. In Section 4.2.3, we will show this model to be the best performer among the five evaluated models.

4.2.1 Mesh and Its Refinement

The polyMesh utility in the OpenFOAM library generates the mesh around the circular cylinder. Figure 4–2 shows the mesh with $n = 120$ and $m = 90$; $n = 2\pi/\Delta\theta$ is the number of cells on the circumference of the cylinder and m is the number of cells across the width of the channel. The cells on the surface of the cylinder are square in shape. The side of the cells on the circumference is equal in dimension to the side in the radial direction.

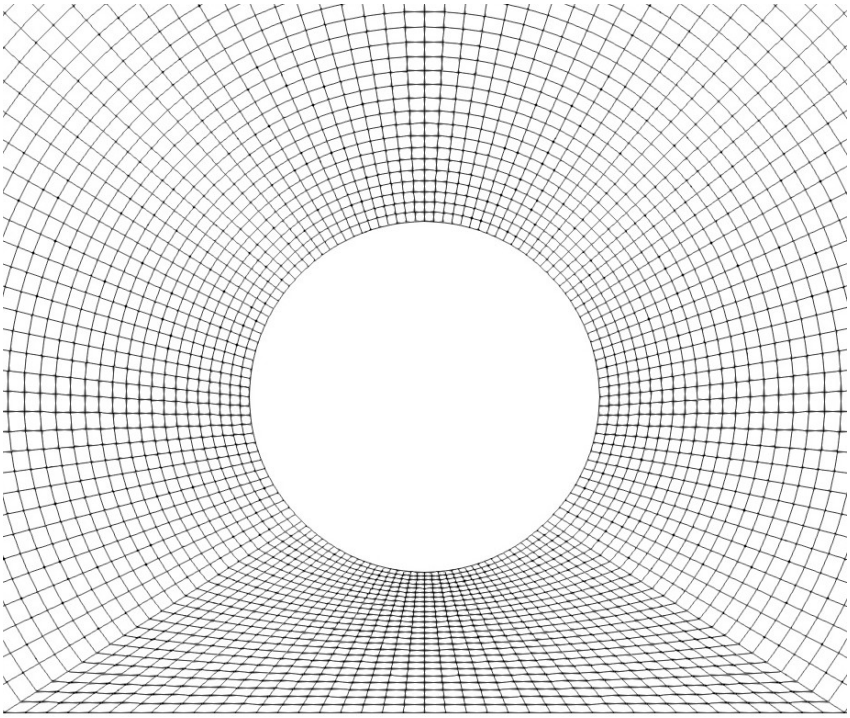

Figure 4–2: Hexahedron mesh around the circular cylinder with $n = 120$ and $m = 90$.

We conducted three simulations with progressively smaller mesh sizes: $(n, m) = (52, 40)$, $(80, 60)$ and $(120, 90)$, respectively. Figures 4–3 (a) and (b) show the transient variations of wave-force coefficients C_x and C_y. The simulations are compared with the measurements in the laboratory by Ermanyuk & Garilov (2005b). These wave-force coefficients are normalized by the reduced gravity g' as follows:

$$C_x = \frac{F_x}{\rho g' \frac{\pi}{4} D^2 W}, \qquad C_y = \frac{F_y}{\rho g' \frac{\pi}{4} D^2 W} \tag{4.1}$$

where F_x and F_y are the components of the force in the direction of the current and in the direction perpendicular to the current, respectively. The lift force F_y is positive in the upward direction and negative in the downward direction. The agreement of the simulations with the experiment is progressively better as the mesh is refined from $(n, m) = (52, 40)$ to $(80, 60)$, and to $(120, 90)$.

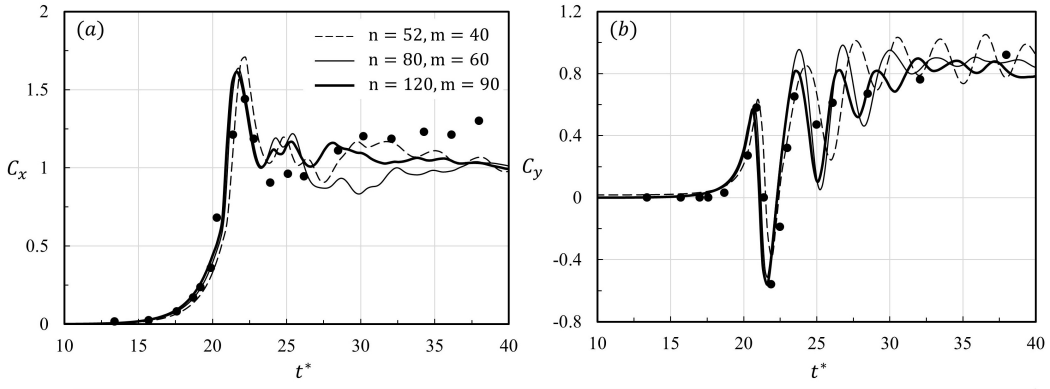

(c)

n	m	$\hat{C}_x$	FE%	Order	$(C_y)^1$	FE%	Order	$(C_y)^2$	FE%	Order
52	40	1.70573	6.25		0.633784	15.03		-0.38331	32.03	
80	60	1.63745	1.99	2.81	0.577149	4.76	2.83	-0.52316	7.23	3.69
120	90	1.61562	0.64		0.559233	1.50		-0.55481	1.60	
∞	∞	**1.60537**	0		**0.550943**			**-0.56394**	0	

Figure 4–3: Transient variations of (a) the drag-force coefficient and (b) the lift-force coefficient obtained from the simulations using three different mesh sizes, and their comparisons with the experimental data by Ermanyuk & Garvilov (2005b). (c) Table for fractional error (FE%) and order of convergence.

The table in Figure 4–3 (c) provides the values of the peak coefficients, the fractional error in percentage and the order of convergence. The order of convergence as the grid is refined is determined by the extrapolation formulas (Stern et al. 2001). From three estimates $(\hat{\alpha}_{k-1}, \hat{\alpha}_k, \hat{\alpha}_{k+1})$ obtained by mesh refinement, the order of convergence is

$$P_k = \frac{1}{\ln r} \ln [\frac{\hat{\alpha}_k - \hat{\alpha}_{k-1}}{\hat{\alpha}_{k+1} - \hat{\alpha}_k}] \tag{4.2}$$

where $r = \Delta_k / \Delta_{k+1}$. The extrapolated value is

$$\hat{\alpha}_{\Delta x \to 0} = \frac{r^{P_k} \hat{\alpha}_{k+1} - \hat{\alpha}_k}{r^{P_k} - 1}. \tag{4.3}$$

In the present order of mesh refinement ($r = 1.5$), the fractional error in percentage is

$$\text{FE}(\%) = \frac{|\hat{\alpha} - \hat{\alpha}_{\Delta x \to 0}|}{\hat{\alpha}_{\Delta x \to 0}} \times 100. \tag{4.4}$$

Using the finest mesh with $(n, m) = (120, 90)$, the fractional errors for values of the force coefficients $\hat{C}_x$, $(C_y)^1$ and $(C_y)^2$ are FE = 0.64%, 1.50% and 1.6%, respectively. The coefficient $\hat{C}_x$ is the peak of the drag coefficient; $(C_y)^1$ is the first peak of the upward-lift coefficient; $(C_y)^2$ is the first peak of the downward-lift coefficient.

4.2.2 Deformation of the Current by Waves

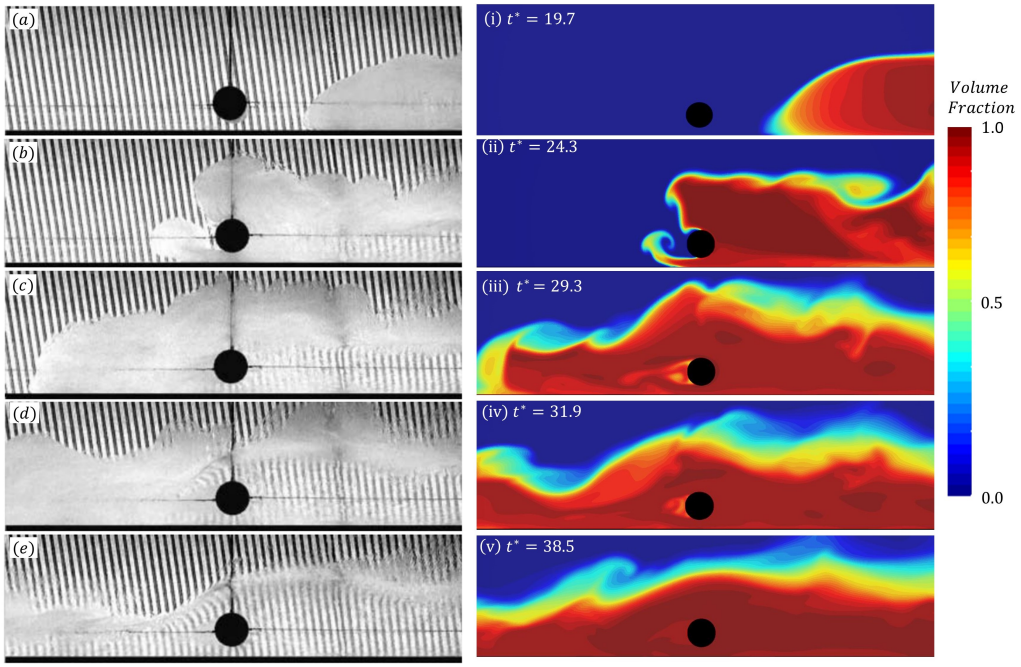

Figure 4–4: Figs. 4(a-e) Sequence of shadowgraphs observed in the laboratory experiment by Ermanyuk & Gavrilov (2005b). Figs. 4(i-v) Volume fraction of the dense fluid on the center plane obtained by the OpenFOAM simulation for $\Delta\rho/\rho = 0.02$.

Large deformations of the gravity current were observed upon impact of the current on the circular cylinder. Figure 4–4 shows the images obtained of the gravity current as it impacted on the circular cylinder using the finest mesh. The images in (i) to (v) of the figure are volume fractions obtained from the simulations at the dimensionless times $t^* = t\sqrt{g'/h_f} = 19.7$, 24.3, 29.3, 31.9 and 38.5. They are compared with the shadow graphs in (a) to (e)

of the figures obtained in the laboratory experiment by Ermanyuk & Gavrilov (2005b). The shadow graphs are averages across the width of the channel. The contours of the volume fraction however are for one slice of the flow on the center plane. The Reynolds number in this laboratory scale experiment was $Re_D = u_f D/\nu = 840$. The velocity that defines the Reynolds number is the frontal velocity u_f at the location of the cylinder obtained in a separate simulation of the gravity current without the cylinder. The wave-force coefficients in Equation 4.1 were introduced by Ermanyuk & Garilov (2005b), recognizing the significance of the internal wave speeds that are proportional to $\sqrt{g'h_f}$.

4.2.3 Selection for the Best Sub-Grid-Scale Model

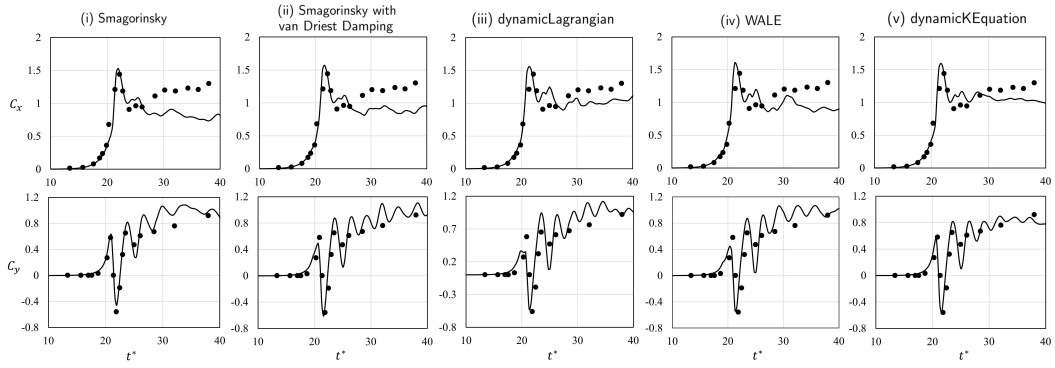

Figure 4–5: Simulation results obtained for C_x and C_y from five SGS models (line) with the finest mesh ($n = 120, m = 90$), compared with the experimental result (solid circle) by Ermanyuk & Gavrilov (2005b).

For large-eddy simulation, the twoLiquidMixingFoam offers the following options for sub-grid-scale turbulence models (OpenFOAM 2017):

(i) Smagorinsky The Smagorinsky SGS model

(ii) Smagorinsky with van Driest Damping The Smagorinsky SGS model with van Driest Damping

(iii) dynamicLagrangian Dynamic SGS model with Lagrangian averaging

(iv) WALE The wall-adapting local eddy-viscosity (WALE) SGS model

(v) dynamicKEquation Dynamic one equation eddy-viscosity model

The Smagorinsky model is the first model created for the purpose of calculating sub-grid eddy viscosity (Smagorinsky 1963). It is the most well known SGS model and has been widely used in the past. An important issue of the Smagorinsky model is that the Smagorinsky coefficient C_s is a constant and can not be reduce to zero, which means the turbulent viscosity does not reduce to zero in the viscous sublayer, i.e. the near-wall region. One of the remedies is applying the van Dreist Damping function to the Smagorinsky model for optimizing the calculation of near-wall behavior (Driest 1956). The dynamic Smagorinsky model allows the calculation of the Smagorinsky coefficient based on local fluid information (Villiers 2006) and hence achieve a better accuracy than the original model. However, negative C_s as well as eddy viscosities generated from the dynamic produce tend to destabilize the simulations. Furthermore, the severe variation of C_s would also reduce the numerical stability. By including the Lagrangian averaging procedure into the dynamic Smagorinsky model, the number of points at which the model predicts negative values of C_s and the spatial variability in the values of C_s is reduced, hence the stability and robustness of the simulation is improved (Meneveau et al. 1996). The WALE model (Nicoud and Ducros, 1999) is gaining its popularity recently, particularly for the use of commercial purpose. The WALE model is a relatively simple eddy-viscosity model that use a constant C_s whilst predict correctly the near-wall behavior without employing wall-damping functions. The dynamic k-equation model adds an additional transport equation of kinetic energy to the model. This approach is proved to be stable with correct asymptotic behavior near wall. Simulation of transitional flow from laminar to turbulent is allowed (Rodi 2013). It also provides

always positive value of SGS kinetic energy (Ghosal et al. 1995). OpenFOAM simulation with the same dynamicKEquation option has been used by Lysenko (2012, 2014) for simulations of flow passing circular cylinder at $Re_D = 3900$ and 20000. Decent comparisons with experiments were obtained. A similar range of Reynolds number is used in our study.

Figures 4–5 (i) to (v) show the simulation results of C_x and C_y obtained by using the five models. The dynamicKEquation model was selected because of superior performance: it correctly reproduced the peak values and the later development of the force coefficients C_x and C_y. Furthermore, it was the only model that captured well the peaks of the first upward lift and the first downward lift. The dynamicKEquation model also produced the fewest oscillations at the tail end of its development. The IAHR Monograph on Large-Eddy Simulation in Hydraulics by Rodi, Constaintinescu and Stoesser (2013) recommends the use of the dynamicKEquation model for sub-grid-scale modeling of turbulence motion.

4.3 Impact on a Cylinder at Reynolds Number $\mathbf{Re}_D = 23500$

We conducted another series of simulations for a Reynolds number of $\mathrm{Re}_D = 23500$ beyond the laboratory scale to determine (a) the effect of the Reynolds number on the impact, and (b) how the mesh should be refined to accommodate the reduction in boundary-layer thickness with the Reynolds number. In this simulation for the higher Reynolds number, the cylinder diameter was $D = 0.1$ m; the density current was released from a block of $h_o = 0.6$ m; the height and the width of the ambient water were $H = 1.5$ m and $W = 0.9$ m, respectively. The initial density difference between the block and its ambient was $\Delta\rho/\rho = 0.02$. The distance between the cylinder and the block was $L_c = 4h_o$, to allow the gravity current to attain the slumping phase as defined by Morino et al. (2005) and Cantero et al. (2007). These conditions

of the simulation produced a frontal velocity of $u_f = 0.235$ m/s at the location of the cylinder, as determined by the simulation without the cylinder. The Reynolds number for these conditions is $\mathrm{Re}_D = 23500$, which is 28 times greater than the Reynolds number in the laboratory experiment by Ermanyuk & Gavrilov (2005b) and is much higher than any previous simulation of the same problem.

According to Bouharie & Chu (2007), the required mesh size to correctly capture the separation of the boundary layer from the surface of a circular cylinder is dependent on the Reynolds number. We therefore conducted another mesh refinement study to determine the adequate mesh size for the higher Reynolds number of $\mathrm{Re}_D = 23500$.

4.3.1 Mesh Refinement for $\mathrm{Re}_D = 23500$

Figures 4–6 (a), (b) and (c) show respectively the transient development of the drag coefficient C_D, lift coefficient C_L and total force coefficient C_F, obtained using three refinements of the mesh with $(n, m) = (108, 40)$, (160, 60) and (240, 90). The table in Figure 4–6 (d) summarizes the results of the mesh refinement study. The elevation of the cylinder $E/D = 0.8$ in this mesh refinement study is somewhat higher than the elevation $E/D = 0.3$ in the laboratory experiment.

To contrast and compare with the known drag and lift coefficients on the cylinder in a flow of uniform density, the impact forces are normalized by the stagnation pressure $0.5\rho u_f^2$ to give the conventional drag coefficient C_D and lift coefficient C_L as follows:

$$C_D = \frac{F_D}{0.5\rho u_f^2 DW} \tag{4.5}$$

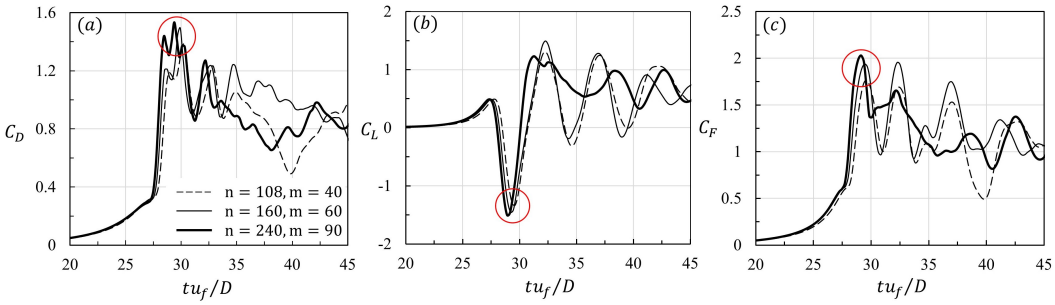

(d)

n	m	$\hat{C}_D$	FE%	Order	$\hat{C}_L$	FE%	Order	$\hat{C}_F$	FE%	Order
108	40	1.38357	13.82		-1.33689	13.54		1.76704	14.93	
160	60	1.49415	6.93	2.52	-1.45436	5.94	2.03	1.93855	9.05	1.57
240	90	1.53387	4.45		-1.50590	2.61		2.02933	4.79	
∞	∞	**1.55612**	0		**-1.54621**	0		**2.13139**	0	

Figure 4–6: Transient development of (a) the drag coefficient, (b) the lift coefficient and (c) the total force coefficient obtained for the Reynolds number of $Re_D = 23500$ and the elevation of $E/D = 0.8$ using three different mesh sizes. (d) Table for fractional error (FE%) and order of convergence. In the table, $\hat{C}_D$ is the peak of the drag coefficient; $\hat{C}_L$ is the negative peak of the downward lift coefficient; $\hat{C}_F$ is the peak of the total force coefficient. The red circles in (a), (b) and (c) mark the occurrences of these peak coefficients.

$$C_L = \frac{F_L}{0.5\rho u_f^2 DW} \tag{4.6}$$

where W is the width of the channel.

In these expressions of the coefficients, F_D = the drag force in the direction of the current and F_L = the lift force in the direction perpendicular to the current. The velocity u_f is the frontal velocity at the location of the cylinder determined by the simulation of the current without the cylinder.

The table in Figure 4–6 (d) tabulates the results of the mesh refinement study. For the mesh with $(n, m) = (240, 90)$, the fractional error (FE) for the peak of the drag coefficient $\hat{C}_D$, the peak of the lift coefficient $\hat{C}_L$, and the peak of the total force coefficient $\hat{C}_F$ are FE = 4.45%, 2.61% and 4.79%, respectively. The mesh with $(n, m) = (240, 90)$ is sufficiently refined. We decided to use this mesh for the rest of the simulations conducted for the Reynolds number of 23500.

4.3.2 Interfacial Deformation and Transient Force Variation

We examined the interfacial waves? deformation of the gravity current at various times after the impact. The interfaces are deformed as waves are produced in the current by the impact. The approaching velocity changes as the interface in front of the cylinder moves up and down due to the waves. Figures 4–7, 4–8 and 4–9 summarize the results from the simulations obtained for three different elevations above the seabed, $E/D = 1.0, 0.4$ and 0.05, respectively.

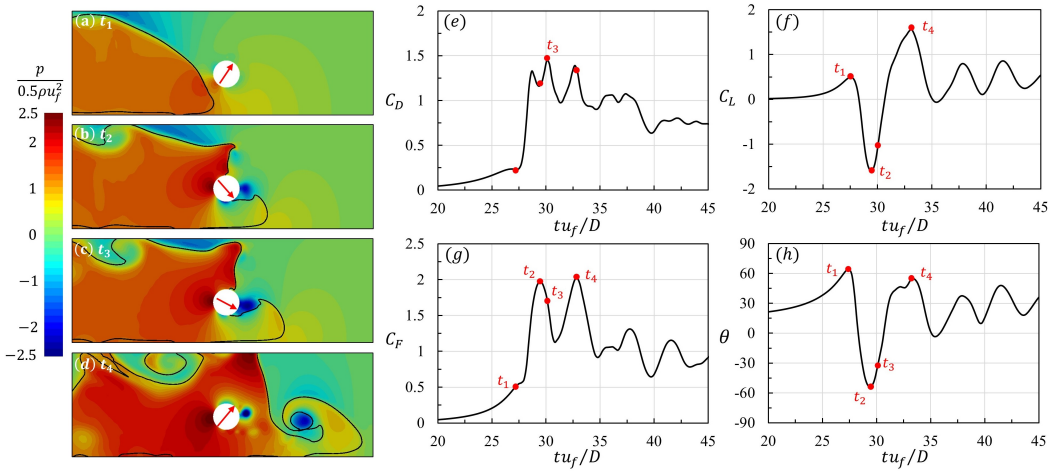

Figure 4–7: Interfacial deformation and transient variation of the force for $Re_D = 23500$ and $E/D = 1.0$. The images in (a), (b), (c) and (d) are the pressure contours of the gravity current around the circular cylinder. The arrows indicate the directions of the total forces. Figures 7 (e), (f), (g) and (h) show the transient variations of the drag coefficient C_D, the lift coefficient C_L, the total force coefficient C_F and the orientation angle of the total force θ, respectively.

The force coefficients are oscillatory, as current in front of the cylinder is affected by the waves. The lift coefficient is comparable in magnitude to the drag coefficient. The force coefficients produced by the unsteady current are two-to-three times greater than the corresponding coefficient in a steady flow of uniform density. We evaluated also the total force $F = \sqrt{F_D^2 + F_L^2}$, the total force coefficient

$$C_F = \frac{F}{0.5\rho u_f^2 DW} \tag{4.7}$$

and the orientation angle of the force

$$\theta = \arctan \frac{F_L}{F_D}. \tag{4.8}$$

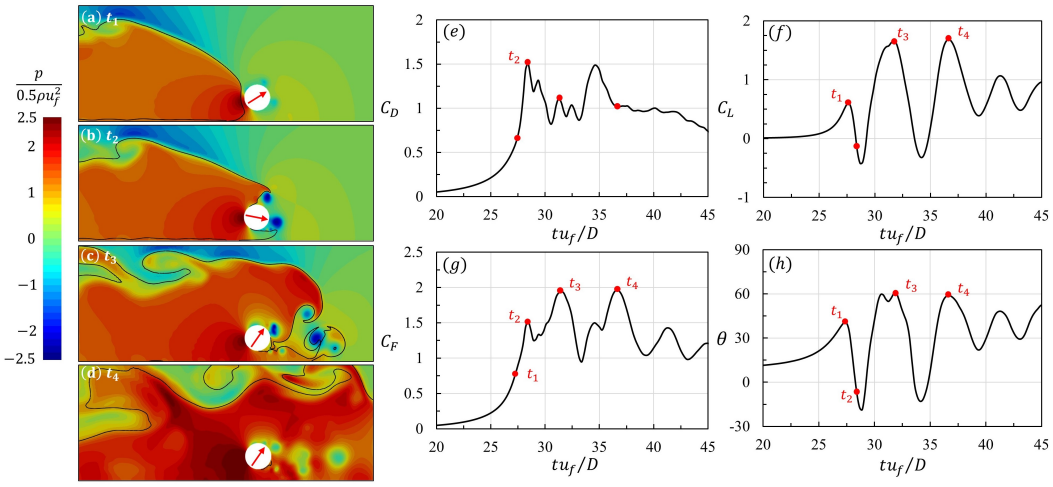

Figure 4–8: Interfacial deformation and transient variation of the force for $Re_D = 23500$ and $E/D = 0.4$. The images in (a), (b), (c) and (d) show the pressure contours of the gravity current around the circular cylinder. The arrows point to the directions of the total forces. Figs. 8 (e), (f), (g) and (h) show the transient variations of the drag coefficient C_D, the lift coefficient C_L, the total force coefficient C_F and the orientation angle of the total force θ, respectively.

The images in Figures 4–7 (a), (b), (c) and (d) show the excess pressure in the gravity current at the center plane of the channel as the current impacts on the cylinder at the dimensionless time $tu_f/D = t_1, t_2, t_3$ and t_4, respectively. The solid line in these images defines the interface where the volume fraction $\alpha = 0.5$. Figures 4–7 (e), (f), (g) and (h) show the transient variations of the coefficients C_D, C_L, C_F and the force orientation angle θ, respectively.

The initial approach of the current to the cylinder at time $tu_f/D = t_1$ is in the form of a wedge (von Kármán 1940). As a consequence, the initial orientation angle of the force is $\theta \simeq 64.3$ at time $tu_f/D = t_1$. Shortly after, at time $tu_f/D = t_2$, the orientation angle of the force flips to a negative value of $\theta =$ -53.9°. The lift coefficient C_L then increases sharply to an upward peak at

time $tu_f/D = t_4$. The orientation angle turns to the positive peak $\theta = 53.4$ at the same time. The peaks of the lift coefficient occur at times t_2 and t_4. The total force coefficient also rises to its peak values at the same times, t_2 and t_4. The time t_3 is the instant when the drag coefficient reaches its maximum.

The simulation results shown in Figure 4–8 are for the cylinder with the smaller elevation $E/D = 0.4$. In this case, the lift coefficient C_L is biased toward the positive value as the lift force is more often in the upward direction. The orientation of the force θ is also biased toward the positive value. The times t_3 and t_4 define the peaks for the upward lift; they also define the peaks of the total force coefficient. For this case, where there is a lower elevation above the seabed, the initial orientation angle at time t_1 has a somewhat smaller value of $\theta_1 = 40.1$. The time t_2 is the occurrence of the maximum drag coefficient. Vorticity is observed to be shedding to the wake of the cylinder at time t_4, as shown in Figure 4–8(d).

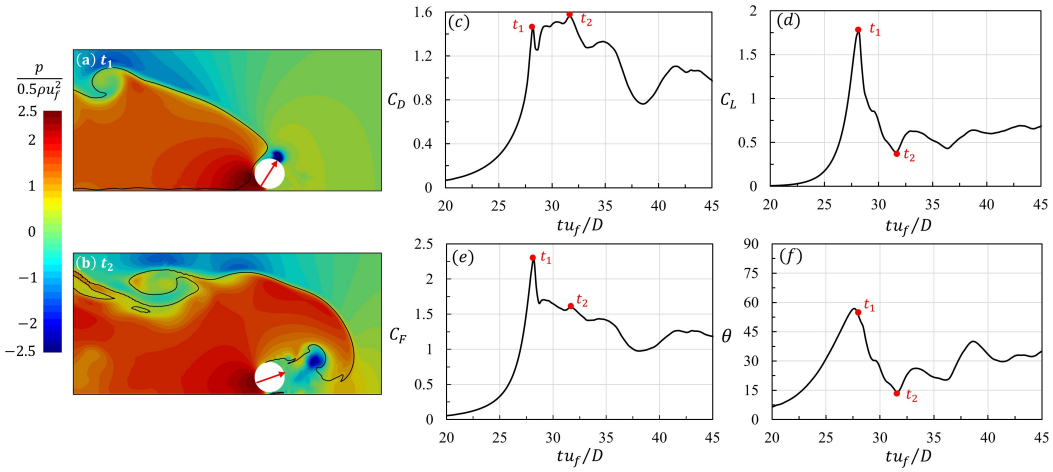

Figure 4–9: Interfacial deformation and transient variation of the force for $Re_D = 23500$ and $E/D = 0.05$. The images in (a) and (b) are the pressure contours of the gravity current around the circular cylinder. The arrows define the directions of the total forces. Figures (c), (d), (e) and (f) show the transient variations of the drag coefficient C_D, the lift coefficient C_L, the total force coefficient C_F and the orientation angle of the total force θ, respectively.

Finally, with a small relative elevation $E/D = 0.05$, the cylinder is practically lying on the seabed, as shown in Figure 4–9. The current below the cylinder is negligible. In this case, the lift coefficient and the orientation angle are positive all the time. The peak of the total force coefficient occurs at time t_1, which is also the time when the lift coefficient reaches its maximum. The peak of the drag coefficient occurs at the time t_2.

4.4 Peak Coefficients and Comparison with Previous Works

The transient development of the force coefficients C_D, C_L, C_F and the orientation angle θ are characterized by their peak values $\hat{C}_D$, $\hat{C}_L$, $\hat{C}_F$ and $\hat{\theta}$. We now examine these peak coefficients (i) to study the effect of the elevation of the cylinder above the seabed, (ii) to compare with the data from the previous works obtained at much lower Reynolds numbers and (iii) to contrast the values of these coefficients with the corresponding values for a steady flow of uniform density.

Figure 4–10 summarizes the peak values obtained from the simulations and the comparison of these values with laboratory experimental data and previous simulation results obtained at the smaller Reynolds numbers. The open-circle $\circ$ symbol denotes the OpenFOAM simulation results for $\mathrm{Re}_D = 23500$. The plus symbol + is the OpenFOAM simulation for $\mathrm{Re}_D = 840$. The cross $\times$ symbol denotes the result of the laboratory experiment by Ermanyuk & Gavrilov (2005b) at the same Reynolds number $\mathrm{Re}_D = 840$. The solid circle and solid triangle denote the values of the previous numerical simulations by Gonzalez-Juez et al. (2009b) at $\mathrm{Re}_D = 558$ and Gonzalez-Juez et al. (2010) at $\mathrm{Re}_D = 459$, respectively.

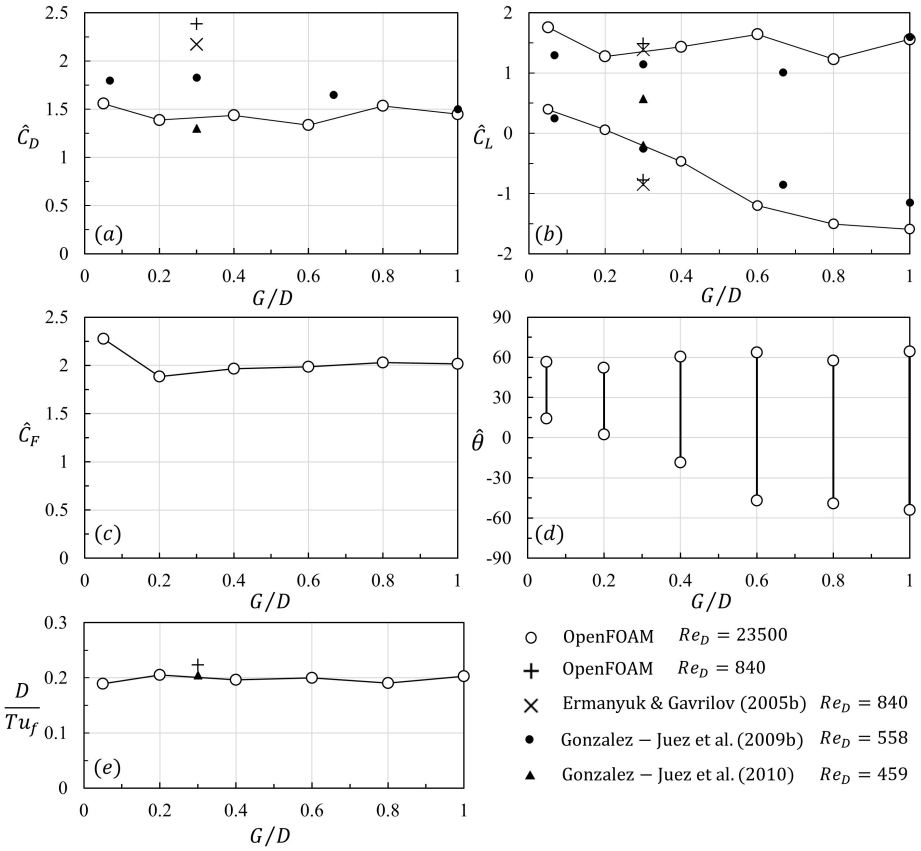

Figure 4–10: Summary for the effect of the Reynolds number Re_D = and the elevation E/D. (a) The maximum drag coefficient $\hat{C}_D$; (b) the maximum upward-lift coefficient $\hat{C}_L$ and downward-lift coefficient $\check{C}_D$; (c) the maximum total force coefficient $\hat{C}_F$; (d) the range of the orientation angle of the total force θ; (e) the Strouhal number.

4.4.1 Effect of Reynolds Number

The values of the peak coefficients are dependent on the Reynolds number. The values for the laboratory-scale Reynolds number $\mathrm{Re}_D = 840$ and $E/D = 0.3$, are $\hat{C}_D \simeq 2.4$ (OpenFOAM) and 2.2 (Ermanyuk & Gavrilov 2005b). This may be compared with $\hat{C}_D \simeq 1.5$ obtained for the Reynolds number $\mathrm{Re}_D = 23500$. The value of the lift coefficient obtained for $\mathrm{Re}_D = 840$ is also different from the values for $\mathrm{Re}_D = 23500$. The lift coefficient for $E/D = 0.3$ has a more severe downward-lift coefficient of $\hat{C}_D \simeq$ -0.8 at the Reynolds number of

$\mathrm{Re}_D = 840$, which is in agreement with the laboratory data by Ermanyuk & Gavrilov (2005b).

The OpenFOAM simulation results are credible as the accuracy was assured by mesh refinement, and they were obtained using the best-performing SGS model. The simulation for the dependence on the cylinder elevation E/D at the Reynolds number $\mathrm{Re}_D = 23500$ has produced essentially the same trend as did the previous study by Gonzalez-Juez et al. (2009b), although the previous study was for a significantly lower Reynolds number ($\mathrm{Re}_D = 558$).

4.4.2 Effect of Elevation

The lift coefficient $\hat{C}_L$ and the angle of orientation θ are most dependent on the elevation of the cylinder E/D. The lift coefficient and the angle of orientation are positive, varying from $\hat{C}_L = 0.4$ to 1.76 and from $\theta \simeq +14^o$ and $+57^o$ at one extreme of a small elevation of $E/D = 0.05$. At the other extreme of $E/D = 1.0$, the oscillation is symmetrical between an upward peak of the lift coefficient $\hat{C}_L = 1.56$ and the downward-peak coefficient of $\hat{C}_L =$ -1.59. The positive peak and negative peak of the orientation angle in this extreme are $\theta \simeq +64^o$ and -56^o, respectively.

The Strouhal numbers are $D/Tu_f \simeq 0.20$, as shown in (e). For comparison, the Strouhal number for a circular cylinder in a steady uniform flow at $Re_D = 23500$ is 0.19 (Norberg 2001). The experiment by Ermanyuk & Gavrilov (2005b) and the simulation by Gonzalez-Juez et al. (2010) at low Reynolds numbers produced similar values for the Strouhal numbers.

4.4.3 Drag and Lift Coefficients for Steady Flow of Uniform Density

The values of the drag and lift coefficients for a circular cylinder in steady flow of uniform density can be found from, for example, the textbook by White

(2015) and the review by Norberg (2001). In a steady flow of uniform density, the peak-to-peak values of the lift coefficient are C_L = -0.68 to 0.68, which is an estimation from the root-mean-square value of 0.48 by Norberg (2001) for the Reynolds number of $Re_D = 23500$. The lift coefficient by the gravity current is typically two-to-three times greater than this value of $C_L = \pm 0.68$.

The peak of the drag coefficient due to waves in the gravity current is $\hat{C}_D \simeq 1.5$, obtained for the Reynolds number of $Re_D = 23500$. By comparison, the value of the drag coefficient is $C_D = 0.82$ for the steady flow of uniform density at the same Reynolds number of $Re_D = 23500$ (White 2015).

4.5 Conclusion

We conducted simulations of gravity current impact on a circular cylinder using the twoLiquidMixingFoam open-source codes at a laboratory scale Reynolds number $\mathrm{Re}_D = 840$ and at a Reynolds number $\mathrm{Re}_D = 23500$. The latter is much greater than the Reynolds number in any previous study. Mesh refinement studies were conducted for both Reynolds numbers to determine the required mesh size for each of the Reynolds numbers. Among the five sub-grid-scale turbulence models evaluated for performance, the dynamicKEquation model produced the most consistent results in comparison with the laboratory data. Besides force coefficients, the simulations also determined the wave deformation on the current caused by the impact. The magnitude of force coefficients due to waves is large (two-to-three times greater) compared with the coefficients for the cylinder in a steady flow of uniform density. The lift coefficient in particular is large, sometimes exceeding the value of the drag coefficient. The rapid reversal in the direction of lift force has led to large amplitude oscillations in the orientation angle of the total force.

The open-source solver twoLiquidMixingFoam is highly adaptable, and is well supported by pre- and post-processing utilities. The mesh refinement and the model performance studies carried out in the present investigation of the gravity current provide a useful guide for engineering simulation of current on structures of various geometries and Reynolds numbers.

Chapter 5
Conclusion and Contribution to Knowledge

This thesis used the interFoam solver and the twoLiquidMixingFoam solver to study (i) the forces of tsunami waves on a vertical wall and on a structure of finite width, (ii) tsunami wave forces on elevated coastal structures, and (iii) impact forces by a earthquake-induced turbidity current on a circular cylinder above the seabed.

For the tsunami wave force on coastal structures, the results of the simulations were calibrated by a number of laboratory works, an analytical solution and the simulations results by the shallow-water hydraulics model. We determine the dependences of wave-force coefficients on the wave Froude number, the size of the structures and the elevation of the structures. These contributions to knowledge are essential for the design and redesign of coastal structures in the adaptation for climate change and sea-level rise.

For the study of turbidity current and its impact on sub-sea structures, the mesh-refinement and model-performance studies conducted with the simulations have shown the twoLiquidMixingFoam solver to be highly reliable and accurate, as the solver has provided results in close agreement with laboratory observation. We further extended the simulations to a Reynolds number which is significantly higher than any previous study of the same problem.

The calibrations and the mesh refinement study have demonstrated the accuracy, reliability and adaptability of the interFoam solver and the twoLiquidMixingFoam solver. The knowledge gained from using these solvers and the pre-/post-processing utilities in the OpenFOAM library has paved the way for

a number of ongoing research work.

Future Work

We have started a number of ongoing projects using the OpenFOAM solvers. These include the studies of tsunami wave impact on submerged breakwater, the overtopping and failure of coastal dike, and impact of turbidity current on various sub-sea structures. A closely related problem to the tsunami is the debris flow impacted onto structures on steep ravine. These are problems that can be resolved using the methods developed in this thesis.

Bibliography

[1] Arikawa, T., Sato, M., Shimosako, K., Hasegawa, I., Yeom, G.-S., and Tomita, T. Failure mechanism of kamaishi breakwaters due to the great east japan earthquake tsunami. *Coastal engineering proceedings 1*, 33 (2012), structures–16.

[2] Arnason, H., Petroff, C., and Yeh, H. Tsunami bore impingement onto a vertical column. *Journal of Disaster Research 4*, 6 (2009), 391–403.

[3] Asakura, R., Iwase, K., Ikeya, T., Takao, M., Kaneto, T., Fujii, N., and Ohmori, M. The tsunami wave force acting on land structures. In *Coastal Engineering 2002: Solving Coastal Conundrums*. World Scientific, 2003, pp. 1191–1202.

[4] ASCE. Minimum design loads and associated criteria for buildings and other structures. Tech. rep., American Society of Civil Engineers, 2017.

[5] Borrero, J. C., Sieh, K., Chlieh, M., and Synolakis, C. E. Tsunami inundation modeling for western sumatra. *Proceedings of the National Academy of Sciences 103*, 52 (2006), 19673–19677.

[6] Brunner, G. W. *HEC-RAS river analysis system: 2D modeling user's manual*. US Army Corps of Engineers, Institute for Water Resources, Hydrologic Engineering Center, 2016.

[7] Camfield, F. E. Tsunami engineering. Tech. rep., COASTAL ENGINEERING RESEARCH CENTER VICKSBURG MS, 1980.

[8] Cantero, M. I., Lee, J., Balachandar, S., and Garcia, M. H. On the front velocity of gravity currents. *Journal of Fluid Mechanics 586* (2007), 1–39.

[9] Chanson, H., Aoki, S.-i., and Maruyama, M. An experimental study of tsunami runup on dry and wet horizontal coastlines. *Science of Tsunami Hazards 20*, 5 (2003), 278–293.

[10] Charvet, I., Ioannou, I., Rossetto, T., Suppasri, A., and Imamura, F. Empirical fragility assessment of buildings affected by the 2011 great east japan tsunami using improved statistical models. *Natural Hazards 73*, 2 (2014), 951–973.

[11] Cross, R. H. Tsunami surge forces. *Journal of the waterways and harbors division 93*, 4 (1967), 201–234.

[12] Cuomo, G., Allsop, W., Bruce, T., and Pearson, J. Breaking wave loads at vertical seawalls and breakwaters. *Coastal Engineering 57*, 4 (2010), 424–439.

[13] Dall'Osso, F., Dominey-Howes, D., Moore, C., Summerhayes, S., and Withycombe, G. The exposure of sydney (australia) to earthquake-generated tsunamis, storms and sea level rise: a probabilistic multi-hazard approach. *Scientific reports 4* (2014), 7401.

[14] Dalrymple, R. A., and Kriebel, D. L. Lessons in engineering from the tsunami in thailand. *BRIDGE-WASHINGTON-NATIONAL ACADEMY OF ENGINEERING- 35*, 2 (2005), 4.

[15] De Risi, R., Goda, K., Mori, N., and Yasuda, T. Bayesian tsunami fragility modeling considering input data uncertainty. *Stochastic Environmental Research and Risk Assessment 31*, 5 (2017), 1253–1269.

[16] De Villiers, E. The potential of large eddy simulation for the modeling of wall bounded flows. *Imperial College of Science, Technology and Medicine, London (UK)* (2006).

[17] Dias, W., Yapa, H., and Peiris, L. Tsunami vulnerability functions from field surveys and monte carlo simulation. *Civil Engineering and Environmental Systems 26*, 2 (2009), 181–194.

[18] Douglas, S., and Nistor, I. On the effect of bed condition on the development of tsunami-induced loading on structures using openfoam. *Natural Hazards 76*, 2 (2015), 1335–1356.

[19] Driest, E. V. On turbulent flow near a wall. *Journal of the aeronautical sciences 23*, 11 (1956), 1007–1011.

[20] Ermanyuk, E., and Gavrilov, N. Interaction of internal gravity current with an obstacle on the channel bottom. *Journal of applied mechanics and technical physics 46*, 4 (2005a), 489–495.

[21] Ermanyuk, E., and Gavrilov, N. Interaction of an internal gravity current with a submerged circular cylinder. *Journal of applied mechanics and technical physics 46*, 2 (2005b), 216–223.

[22] FEMA. Guidelines for design of structures for vertical evacuation from tsunamis. Tech. rep., Federal Emergency Management Agency, 2008.

[23] FEMA. Guidelines for design of structures for vertical evacuation from tsunamis. Tech. rep., Federal Emergency Management Agency, 2012.

[24] FEMA. Guidelines for design of structures for vertical evacuation from tsunamis. Tech. rep., Federal Emergency Management Agency, 2012.

[25] FitzGerald, D. M., Fenster, M. S., Argow, B. A., and Buynevich, I. V. Coastal impacts due to sea-level rise. *Annual Review of Earth and Planetary Sciences 36* (2008).

[26] Fritz, H. M., Phillips, D. A., Okayasu, A., Shimozono, T., Liu, H., Mohammed, F., Skanavis, V., Synolakis, C. E., and Takahashi, T. The 2011 japan tsunami current velocity measurements from survivor videos at kesennuma bay using lidar. *Geophysical Research Letters 39*, 7 (2012).

[27] Fujima, K., Achmad, F., Shigihara, Y., and Mizutani, N. Estimation of tsunami force acting on rectangular structures. *Journal of Disaster Research 4*, 6 (2009), 404–409.

[28] Ghobarah, A., Saatcioglu, M., and Nistor, I. The impact of the 26 december 2004 earthquake and tsunami on structures and infrastructure. *Engineering structures 28*, 2 (2006), 312–326.

[29] Ghosal, S., Lund, T. S., Moin, P., and Akselvoll, K. A dynamic localization model for large-eddy simulation of turbulent flows. *Journal of fluid mechanics 286* (1995), 229–255.

[30] Goff, J., Liu, P. L., Higman, B., Morton, R., Jaffe, B. E., Fernando, H., Lynett, P., Fritz, H., Synolakis, C., and Fernando, S. Sri lanka field survey after the december 2004 indian ocean tsunami. *Earthquake Spectra 22*, 3_suppl (2006), 155–172.

[31] Greenshields, C. J. Openfoam user guide. *OpenFOAM Foundation Ltd, version 5.0* (2017).

[32] Greenshields, C. J. Openfoam user guide, v5. 0. *OpenFOAM foundation Ltd* (2017).

[33] Gruber, M., Johnson, C., Tang, C., Jensen, M. H., Yde, L., and Hélix-Nielsen, C. Computational fluid dynamics simulations of flow and concentration polarization in forward osmosis membrane systems. *Journal of membrane science 379*, 1-2 (2011), 488–495.

[34] Hargreaves, D., Morvan, H., and Wright, N. Validation of the volume of fluid method for free surface calculation: the broad-crested weir. *Engineering Applications of Computational Fluid Mechanics 1*, 2 (2007), 136–146.

[35] Härtel, C., Meiburg, E., and Necker, F. Analysis and direct numerical simulation of the flow at a gravity-current head. part 1. flow

topology and front speed for slip and no-slip boundaries. *Journal of Fluid Mechanics 418* (2000), 189–212.

[36] Heezen, B. C., and Ewing, W. M. Turbidity currents and submarine slumps, and the 1929 grand banks [newfoundland] earthquake. *American journal of Science 250*, 12 (1952), 849–873.

[37] Henderson, F. M. Open channel flow. Tech. rep., 1966.

[38] Higuera, P., Lara, J. L., and Losada, I. J. Realistic wave generation and active wave absorption for navier–stokes models: Application to openfoam®. *Coastal Engineering 71* (2013), 102–118.

[39] Higuera, P., Lara, J. L., and Losada, I. J. Simulating coastal engineering processes with openfoam®. *Coastal Engineering 71* (2013), 119–134.

[40] Higuera, P., Lara, J. L., and Losada, I. J. Three-dimensional interaction of waves and porous coastal structures using openfoam®. part i: formulation and validation. *Coastal Engineering 83* (2014), 243–258.

[41] Higuera, P., Lara, J. L., and Losada, I. J. Three-dimensional interaction of waves and porous coastal structures using openfoam®. part ii: Application. *Coastal Engineering 83* (2014), 259–270.

[42] Hsu, S., Tsai, C., Ku, C., and Sibuet, J. Flow of turbidity currents as evidenced by failure of submarine telecommunication cables. In *Intern Conf on Seafloor Mapping for Geohazard Assessment, Extended Abs, Rendiconti online, Società Geologica Italiana* (2009), vol. 7, pp. 167–171.

[43] Hsu, S.-K., Kuo, J., Chung-Liang, L., Ching-Hui, T., Doo, W.-B., Ku, C.-Y., and Sibuet, J.-C. Turbidity currents, submarine landslides and the 2006 pingtung earthquake off sw taiwan. *TAO: Terrestrial, Atmospheric and Oceanic Sciences 19*, 6 (2008), 7.

[44] Jaffe, B. E., Goto, K., Sugawara, D., Richmond, B. M., Fujino, S., and Nishimura, Y. Flow speed estimated by inverse modeling of sandy tsunami deposits: results from the 11 march 2011 tsunami on the coastal plain near the sendai airport, honshu, japan. *Sedimentary Geology 282* (2012), 90–109.

[45] Jones, W., and Launder, B. E. The prediction of laminarization with a two-equation model of turbulence. *International journal of heat and mass transfer 15*, 2 (1972), 301–314.

[46] Karimpour, S., and Chu, V. Transverse dam-break waves. *Journal of Fluid Mechanics 2* (2014).

[47] Karimpour, S., and Chu, V. H. Instability of unbounded transverse mixing layer in shallow waters. *Canadian Journal of Civil Engineering 43*, 6 (2016), 504–510.

[48] Karimpour Ghannadi, S., and Chu, V. H. High-order interpolation schemes for shear instability simulations. *International Journal of Numerical Methods for Heat & Fluid Flow 25*, 6 (2015), 1340–1360.

[49] Kato, F., Suwa, Y., Watanabe, K., and Hatogai, S. Mechanisms of coastal dike failure induced by the great east japan earthquake tsunami. *Coastal Engineering Proceedings 1*, 33 (2012), 1–9.

[50] Kennedy, A., Rogers, S., Sallenger, A., Gravois, U., Zachry, B., Dosa, M., and Zarama, F. Building destruction from waves and surge on the bolivar peninsula during hurricane ike. *Journal of Waterway, Port, Coastal, and Ocean Engineering 137*, 3 (2011), 132–141.

[51] Kirkgöz, M. Breaking wave impact on vertical and sloping coastal structures. *Ocean Engineering 22*, 1 (1995), 35–48.

[52] Kolmogorov, A. N. The local structure of turbulence in incompressible viscous fluid for very large reynolds numbers. *Cr Acad. Sci. URSS 30* (1941), 301–305.

[53] Koshimura, S., Oie, T., Yanagisawa, H., and Imamura, F. Developing fragility functions for tsunami damage estimation using numerical model and post-tsunami data from banda aceh, indonesia. *Coastal Engineering Journal 51*, 3 (2009), 243–273.

[54] Krpan, R., and Končar, B. Simulation of turbulent wake at mixing of two confined horizontal flows. *Science and Technology of Nuclear Installations 2018* (2018).

[55] Li, L., Switzer, A. D., Wang, Y., Chan, C.-H., Qiu, Q., and Weiss, R. A modest 0.5-m rise in sea level will double the tsunami hazard in macau. *Science advances 4*, 8 (2018), eaat1180.

[56] Linton, D., Gupta, R., Cox, D., van de Lindt, J., Oshnack, M. E., and Clauson, M. Evaluation of tsunami loads on wood-frame walls at full scale. *Journal of Structural Engineering 139*, 8 (2012), 1318–1325.

[57] Liu, P. L.-F., Lynett, P., Fernando, H., Jaffe, B. E., Fritz, H., Higman, B., Morton, R., Goff, J., and Synolakis, C. Observations by the international tsunami survey team in sri lanka. *Science 308*, 5728 (2005), 1595–1595.

[58] Longo, S., Ungarish, M., Di Federico, V., Chiapponi, L., and Petrolo, D. Gravity currents produced by lock-release: theory and experiments concerning the effect of a free top in non-boussinesq systems. *Advances in water resources 121* (2018), 456–471.

[59] Lysenko, D. A., Ertesvåg, I. S., and Rian, K. E. Large-eddy simulation of the flow over a circular cylinder at reynolds number 3900 using the openfoam toolbox. *Flow, turbulence and combustion 89*, 4 (2012), 491–518.

[60] Lysenko, D. A., Ertesvåg, I. S., and Rian, K. E. Large-eddy simulation of the flow over a circular cylinder at reynolds number 20000. *Flow, turbulence and combustion 92*, 3 (2014), 673–698.

[61] Matsutomi, H., Sakakiyama, T., Nugroho, S., and Matsuyama, M. Aspects of inundated flow due to the 2004 indian ocean tsunami. *Coastal Engineering Journal 48*, 02 (2006), 167–195.

[62] Meneveau, C., Lund, T. S., and Cabot, W. H. A lagrangian dynamic subgrid-scale model of turbulence. *Journal of fluid mechanics 319* (1996), 353–385.

[63] Mori, N., Takahashi, T., Yasuda, T., and Yanagisawa, H. Survey of 2011 tohoku earthquake tsunami inundation and run-up. *Geophysical research letters 38*, 7 (2011).

[64] Nguyen, V. T. 3d numerical simulation of free surface flows over hydraulic structures in natural channels and rivers. *Applied Mathematical Modelling 39*, 20 (2015), 6285–6306.

[65] Nicholls, R. J., and Cazenave, A. Sea-level rise and its impact on coastal zones. *science 328*, 5985 (2010), 1517–1520.

[66] Nicoud, F., and Ducros, F. Subgrid-scale stress modelling based on the square of the velocity gradient tensor. *Flow, turbulence and Combustion 62*, 3 (1999), 183–200.

[67] Nistor, I., Palermo, D., Nouri, Y., Murty, T., and Saatcioglu, M. Tsunami forces on structures. *In: Kim YC (ed), Handbook of Coastal and Ocean Engineering.* (2010), 261–286.

[68] Norberg, C. Flow around a circular cylinder: aspects of fluctuating lift. *Journal of Fluids and Structures 15*, 3-4 (2001), 459–469.

[69] Norberg, C. Fluctuating lift on a circular cylinder: review and new measurements. *Journal of Fluids and Structures 17*, 1 (2003), 57–96.

[70] Nouri, Y., Nistor, I., Palermo, D., and Cornett, A. Experimental investigation of tsunami impact on free standing structures. *Coastal Engineering Journal 52*, 01 (2010), 43–70.

[71] OCADI. *Technical standards and commentaries for port and harbour facilities in Japan*. The Overseas Coastal Area Development Institute of Japan, Ports and Harbours Bureau, Tokyo, Japan., 2009.

[72] Ooi, S. K., Constantinescu, G., and Weber, L. Numerical simulations of lock-exchange compositional gravity current. *Journal of Fluid Mechanics 635* (2009), 361–388.

[73] Ooi, S. K., Constantinescu, G., and Weber, L. J. 2d large-eddy simulation of lock-exchange gravity current flows at high grashof numbers. *Journal of Hydraulic Engineering 133*, 9 (2007), 1037–1047.

[74] Park, H., and Cox, D. T. Probabilistic assessment of near-field tsunami hazards: Inundation depth, velocity, momentum flux, arrival time, and duration applied to seaside, oregon. *Coastal Engineering 117* (2016), 79–96.

[75] Park, H., Cox, D. T., Lynett, P. J., Wiebe, D. M., and Shin, S. Tsunami inundation modeling in constructed environments: A physical and numerical comparison of free-surface elevation, velocity, and momentum flux. *Coastal Engineering 79* (2013), 9–21.

[76] Park, H., Cox, D. T., and Shin, S. Physical modeling of horizontal and vertical tsunami forces on the elevated overland structure. *Journal of Coastal Research 91*, sp1 (2019), 51–55.

[77] Park, H., Tomiczek, T., Cox, D. T., van de Lindt, J. W., and Lomonaco, P. Experimental modeling of horizontal and vertical wave forces on an elevated coastal structure. *Coastal Engineering 128* (2017), 58–74.

[78] Parry, M., Parry, M. L., Canziani, O., Palutikof, J., Van der Linden, P., Hanson, C., et al. *Climate change 2007-impacts, adaptation and vulnerability: Working group II contribution to the fourth assessment report of the IPCC*, vol. 4. Cambridge University Press, 2007.

[79] PATANKAR, S. V., and Spalding, D. B. *A calculation procedure for the transient and steady-state behaviour of shell-and-tube heat exchangers*. Imperial College of Science and Technology, Department of Mechanical Engineering, 1972.

[80] Ramsden, J. D. Forces on a vertical wall due to long waves, bores, and dry-bed surges. *Journal of waterway, port, coastal, and ocean engineering 122*, 3 (1996), 134–141.

[81] Ramsden, J. D., and Raichlen, F. Forces on vertical wall caused by incident bores. *Journal of Waterway, Port, Coastal, and Ocean Engineering 116*, 5 (1990), 592–613.

[82] Reese, S., Bradley, B. A., Bind, J., Smart, G., Power, W., and Sturman, J. Empirical building fragilities from observed damage in the 2009 south pacific tsunami. *Earth-Science Reviews 107*, 1-2 (2011), 156–173.

[83] Ritter, A. Die fortpflanzung de wasserwellen. *Zeitschrift Verein Deutscher Ingenieure 36*, 33 (1892), 947–954.

[84] Robertson, I., Paczkowski, K., Riggs, H., and Mohamed, A. Experimental investigation of tsunami bore forces on vertical walls. *Journal of Offshore Mechanics and Arctic Engineering 135*, 2 (2013), 021601.

[85] Rodi, W., Constantinescu, G., and Stoesser, T. *Large-eddy simulation in hydraulics*. Crc Press, 2013.

[86] Roeber, V., and Bricker, J. D. Destructive tsunami-like wave generated by surf beat over a coral reef during typhoon haiyan. *Nature communications 6* (2015), 7854.

[87] Rossetto, T., Peiris, N., Pomonis, A., Wilkinson, S., Del Re, D., Koo, R., and Gallocher, S. The indian ocean tsunami of december 26, 2004: observations in sri lanka and thailand. *Natural Hazards 42*, 1 (2007), 105–124.

[88] Rusche, H. *Computational fluid dynamics of dispersed two-phase flows at high phase fractions*. PhD thesis, Imperial College London (University of London), 2003.

[89] Seiffert, B., Hayatdavoodi, M., and Ertekin, R. C. Experiments and computations of solitary-wave forces on a coastal-bridge deck. part i: Flat plate. *Coastal Engineering 88* (2014), 194–209.

[90] Shin, J., Dalziel, S., and Linden, P. Gravity currents produced by lock exchange. *Journal of Fluid Mechanics 521* (2004), 1–34.

[91] Smagorinsky, J. General circulation experiments with the primitive equations: I. the basic experiment. *Monthly weather review 91*, 3 (1963), 99–164.

[92] St-Germain, P., Nistor, I., and Townsend, R. Numerical modeling of the impact with structures of tsunami bores propagating on dry

and wet beds using the sph method. *International Journal of Protective Structures 3*, 2 (2012), 221–255.

[93] St-Germain, P., Nistor, I., Townsend, R., and Shibayama, T. Smoothed-particle hydrodynamics numerical modeling of structures impacted by tsunami bores. *Journal of Waterway, Port, Coastal, and Ocean Engineering 140*, 1 (2013), 66–81.

[94] Stern, F., Wilson, R. V., Coleman, H. W., and Paterson, E. G. Comprehensive approach to verification and validation of cfd simulations part 1: methodology and procedures. *Journal of fluids engineering 123*, 4 (2001), 793–802.

[95] Suppasri, A., Koshimura, S., Imai, K., Mas, E., Gokon, H., Muhari, A., and Imamura, F. Damage characteristic and field survey of the 2011 great east japan tsunami in miyagi prefecture. *Coastal Engineering Journal 54*, 1 (2012), 1250005–1.

[96] Suppasri, A., Mas, E., Charvet, I., Gunasekera, R., Imai, K., Fukutani, Y., Abe, Y., and Imamura, F. Building damage characteristics based on surveyed data and fragility curves of the 2011 great east japan tsunami. *Natural Hazards 66*, 2 (2013), 319–341.

[97] Takagi, H., and Bricker, J. D. Assessment of the effectiveness of general breakwaters in reducing tsunami inundation in ishinomaki. *Coastal Engineering Journal 56*, 4 (2014), 1450018–1.

[98] Te Chow, V. *Open channel hydraulics*. McGraw-Hill Book Company, Inc; New York, 1959.

[99] Tomiczek, T., Kennedy, A., and Rogers, S. Collapse limit state fragilities of wood-framed residences from storm surge and waves during hurricane ike. *Journal of waterway, port, coastal, and ocean engineering 140*, 1 (2014), 43–55.

[100] VIMS. Sea-level report cards. Tech. rep., Virginia Institute of Marine Science, 2019.

[101] Von Karman, T., et al. The engineer grapples with nonlinear problems. *Bulletin of the American Mathematical Society 46*, 8 (1940), 615–683.

[102] Weller, H. G., Tabor, G., Jasak, H., and Fureby, C. A tensorial approach to computational continuum mechanics using object-oriented techniques. *Computers in physics 12*, 6 (1998), 620–631.

[103] Werner, A. D., and Simmons, C. T. Impact of sea-level rise on sea water intrusion in coastal aquifers. *Groundwater 47*, 2 (2009), 197–204.

[104] White, F. M. *Introduction to Fluid mechanics*. McGraw-Hill Education, 2015.

[105] Wüthrich, D., Pfister, M., Nistor, I., and Schleiss, A. J. Experimental study of tsunami-like waves generated with a vertical release technique on dry and wet beds. *Journal of Waterway, Port, Coastal, and Ocean Engineering 144*, 4 (2018), 04018006.

[106] Wüthrich, D., Pfister, M., Nistor, I., and Schleiss, A. J. Experimental study on the hydrodynamic impact of tsunami-like waves against impervious free-standing buildings. *Coastal Engineering Journal 60*, 2 (2018a), 180–199.

[107] Xie, P., and Chu, V. H. The forces of tsunami waves on a vertical wall and on a structure of finite width. *Coastal Engineering 149* (2019), 65–80.

[108] Yakhot, V., Orszag, S., Thangam, S., Gatski, T., and Speziale, C. Development of turbulence models for shear flows by a double expansion technique. *Physics of Fluids A: Fluid Dynamics 4*, 7 (1992), 1510–1520.

[109] Yakhot, V., and Orszag, S. A. Renormalization group analysis of turbulence. i. basic theory. *Journal of scientific computing 1*, 1 (1986), 3–51.

[110] Yeh, H., Barbosa, A. R., Ko, H., and Cawley, J. G. Tsunami loadings on structures: Review and analysis. *Coastal Engineering Proceedings 1*, 34 (2014), 4.

[111] Yeh, H., Sato, S., and Tajima, Y. The 11 march 2011 east japan earthquake and tsunami: Tsunami effects on coastal infrastructure and buildings. *Pure and Applied Geophysics 170*, 6-8 (2013), 1019–1031.

[112] Yoshizawa, A. A statistically-derived subgrid model for the large-eddy simulation of turbulence. *The Physics of Fluids 25*, 9 (1982), 1532–1538.

[113] Yoshizawa, A., and Horiuti, K. A statistically-derived subgrid-scale kinetic energy model for the large-eddy simulation of turbulent flows. *Journal of the Physical Society of Japan 54*, 8 (1985), 2834–2839.

[114] Zhang, S., Jiang, B., Law, A. W.-K., and Zhao, B. Large eddy simulations of 45 inclined dense jets. *Environmental Fluid Mechanics 16*, 1 (2016), 101–121.

Appendix A: Wave Generation and Propagation

Figure 5–1 (a) shows a simulation of a bore advancing in an open channel. The initial still-water depth is $H = 1$ m. The inflow at the entrance has $H_w = 3.215$ m, $U_w = 5.616$ m/s and $\mathrm{Fr}_w = 1.0$, determined by the compatibility condition. The channel width is set as 10 times of the inflow depth to avoid the influence of the banks on the propagation. The bore is advancing with a relatively uniform depth H_w, except in the section of the bore front where many turbulence structures exist. A previous study using 2-D simulations by Xie & Chu (2019) shown that bore had dramatic depth oscillations near the entrance, while the oscillations were much milder at a distance of $L \geq 30H_w$ from the entrance. Three probes are set up to record the variations of water depth and velocity at different locations. Probe (i) locates at a distance $L = 25H_w$ to the entrance and a distance $B = 2.5H_w$ to the right-hand bank; probe (ii) has $L = 30H_w$ and $B = 5H_w$; probe (iii) has $L = 30H_w$ and $B = 7.5H_w$.

After the wave passes the locations of the probes, the transient wave heights h and velocities u on the probes are identical to H_w and U_w, respectively. On (i) with $L = 25H_w$, the wave velocity has a mild peak of $1.1U_w$ at the beginning, mainly due to the turbulent effect at the wavefront. The variations of wave height and velocity on the spanwise direction are not noticeble. By using such a boundary condition, the wave can be defined with a constant height H_w and a constant velocity U_w when the wave has propagated for a distance $L \geq 30H_w$.

Appendix B: Examination of the Channel Width Effect

In laboratory work of tsunami impact on coastal structures, the channel width was typically set to be a fixed value refers to the structure width. For instance, in the study by Arnason et al. (2009), the channel width to structure

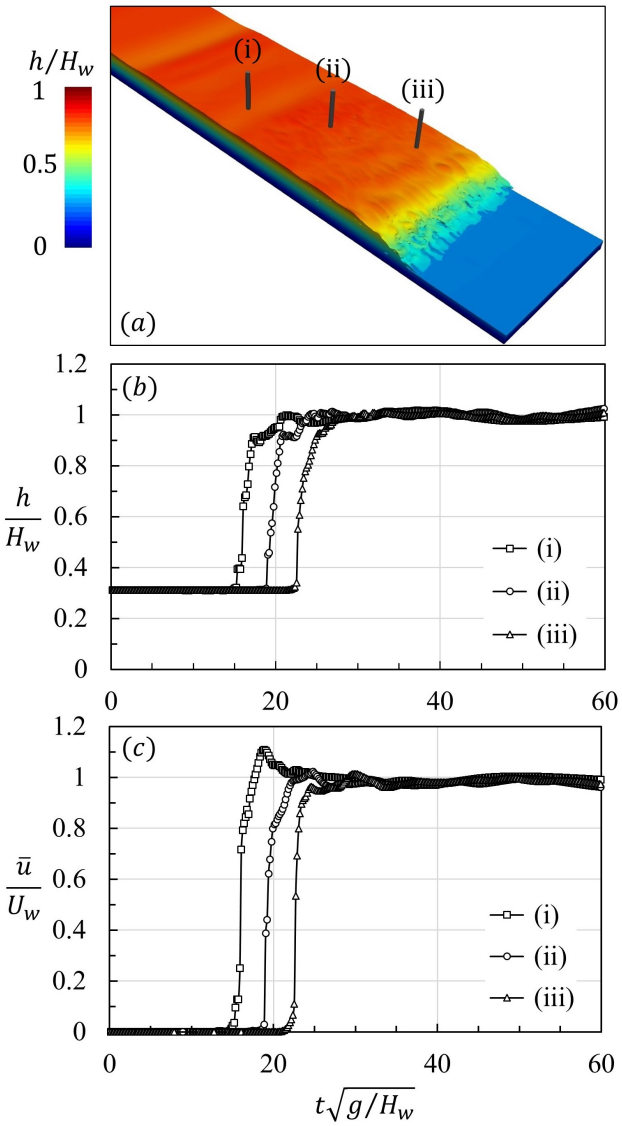

Figure 5–1: (a) Propagation of a bore in an open channel with a width of $W_{ch} = 10H_w$. The bore has a height of $H_w/H = 3.2$ and and $\mathrm{Fr}_w = 1.0$. The color contour denotes the wave elevation referred to the inflow depth H_w. Probe (i) locates at a distance $L = 25H_w$ to the entrance and a distance $B = 2.5H_w$ to the right-hand bank; probe (ii) has $L = 30H_w$ and $B = 5H_w$; probe (iii) has $L = 30H_w$ and $B = 7.5H_w$. The variations of the water depth h and the averaged velocity across the depth $\bar{u}$ on the three probes are plotted in (b) and (c), respectively, versus the dimensionless time $t\sqrt{g/H_w}$.

width ratio was chosen as $W_{ch}/W = 5$; this ratio was set up as 4.33 in the experiments Douglas et al. (2015); Wüthrich et al. (2018) summarized a series of work using different channel widths and chose a width ratio of $W_{ch}/W = 4.67$ for their study of wave impact. Varying the channel width while maintaining other parameters unchanged is impractical in laboratory. Heretofore, whether the channel width has an effect of the tsunami wave impact on a structure is not clear and awaiting investigation.

In this study, we performed numerical simulations to explore the channel width effect of the wave force on an elevated structure. The incoming tsunami wave has a Froude number of $\mathrm{Fr}_r = 1.0$ and a wave height of $H_w/H = 3.215$. The elevated structure has a floor elevation of $E/H = 1.5$ refer to the still water depth $H = 1$ m. The structure width is fixed as $W/H_w = 5$. The channel widths are $W_{ch}/W = 2$, 3, 4, 5 and 6.

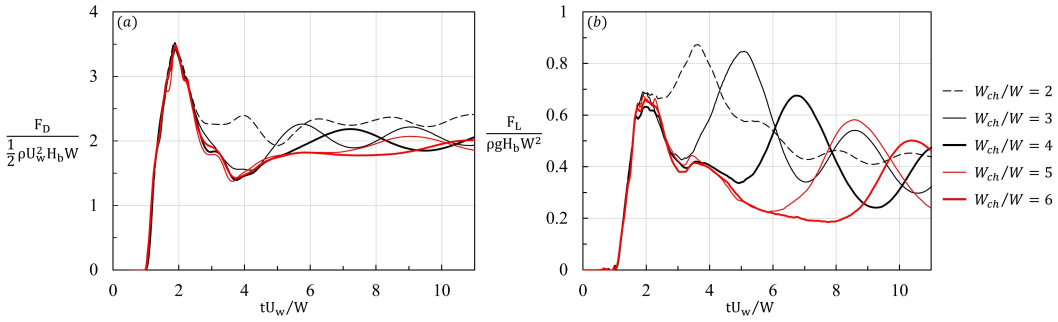

Figure 5–2: The variations of (a) drag coefficient and (b) lift coefficient on a elevated structure in different channel widths. The still water depth is $H = 1$ m. The incoming tsunami wave has $H_w = 3.2$ m, $U_w = 5.61$ m/s and $\mathrm{Fr}_w = 1.0$. The structure has a floor elevation of $E = 1.5$ m and a width of $W = 16$ m.

Figure 5–2 (a) shows the transient variations of the drag coefficients C_D in the five channels of different widths. Despite the differences in the channel width, the peak drag coefficients $\hat{C_D}$ are identical. The coefficients at the quasi-steady state are approximately $\tilde{C_D} = 0.55\hat{C_D}$ except for the case with $W_{ch}/W = 2$, which has a slightly higher quasi-steady drag coefficient than the

others. Accordingly, the channel width has no impact on the peak drag force, and its influence on the quasi-steady drag force is insignificant unless that the channel is as narrow as W_{ch}/W =2. For W_{ch}/W =2, the slight increase of drag force at quasi-steady state is due to the blockage effect in a narrow channel. This blockage effect was previously discussed by Qi et al.(2015).

The variations of lift coefficients are shown in Figure 5–2 (b). During the interaction with the wave, the lift coefficients have a first peak following by a string of fluctuations, which is dissipating with time. The channels of $W_{ch}/W = 2$ and 3 have a second peak that is apparently higher than the first peak.

In Figure **??**, the wave elevations around the elevated structure for the two channels of $W_ch/W = 2$ and 6 at the time of $t^* = tU_w/W = 1.96$, 3.64 and 6.00 are plotted from (a) to (e). The pressure contour inset in each frame varies from negative pressure $-\rho g(H_w - E)$ (blue) to positive pressure $\rho g(H_w - E)$ (red). The black curves denote the water volume fraction of 50%.

At $t^* = 1.96$, which is the time of the first peak in Figure 5–2 (b), the wave profiles around the structure in (a) and (b) are similar to each other. The wave climbs up on the front of the structure, flows around the sides and intrudes into the gap. As the wavefront reaches the rear of the structure, the flow beneath the structure has fulfilled the gap with severe air entrainment. High pressures are observed near the two flanks of the structure, rather than the front or rear. The effect of channel width is barely observed at this moment. At $t^* = 3.64$, the wave in a wide channel of $W_{ch}/W = 6$ is scattering on the front and by the sides of the structure, as shown in (d). However, the wave in the narrow channel of $W_{ch}/W = 2$ in (c) has hit the banks and been reflected back to the structure location. Water has piled up around the structure. The wave elevations on the four faces of the structure are higher comparing to

those in (d). The pressures on the slab in (c) are apparently higher than the one in (d). The highest pressures occur on the two sides. It is at this moment that the lift coefficient on the structure in a channel of $W_{ch}/W = 2$ reaches its maxima. At $t^* = 6.00$ in (e), the wave piling up in front of the structure is propagating upstream. The reflected waves from the banks intersect at the downstream of the structure. The pressures on the slab drop down as the wave elevations around the structure are lower comparing to (c). In (f), the scattering wave has hit the banks and bounced back toward the structure. A lift force fluctuation is expected once the reflected wave interacts with the structure, which occurs at a later time $t^* = 10.3$ shown in Figure 5–2 (b).

In conclusion, the effect of channel width on the drag force, in particular on the force maxima, is insignificant. Due to the interactions of reflected waves with the structure, the lift force has a string of fluctuations after the first peak. The fluctuations dissipate with time. The second peak could be higher than the first one, depending on the width of the channel. An elevated structure could suffer a more significant uplift force if walls or other structures are sitting beside.

,,